Experiments with Toroidal Microresonators in Cavity QED

Thesis by

Elizabeth Wilcut Connolly

In Partial Fulfillment of the Requirements

for the Degree of

Doctor of Philosophy

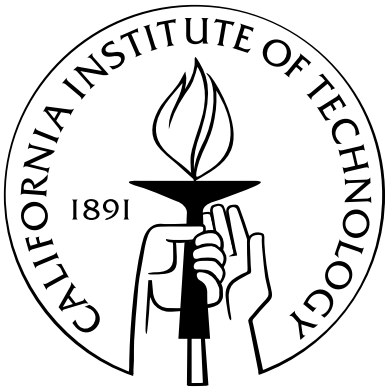

California Institute of Technology

Pasadena, California

2009

(Defended February 9, 2009)

Acknowledgements

I would like to thank the entire Quantum Optics group, particularly my adviser Jeff Kimble, for giving me such a wonderful opportunity to be part of truly amazing and ground-breaking research. In particular, my appreciation to Takao Aoki, Warwick Bowen, Tobias Kippenberg, Barak Dayan, Scott Kelber, Eric Ostby, Kok Win Goh, Matt Eichenfeld, and Daniel Alton for all the wonderful times (and often late nights) in lab. I can't even begin to quantify the amount of knowledge learned from coffee breaks with the ever-patient Takao and Warwick.

Mr Arner, thank you for showing me what an amazing world there is to explore in physics; more important than the fundamental principles, you taught me how to truly enjoy it. For giving me the confidence and resources to succeed at Cal, thank you Bruce Birkette and Mia Ong. For always being there as my mentor and friend, Colin McCormick.

Last, but surely not least, my family has been the support I needed to follow my dreams and explore to the horizons. My parents, who always believe in me and will do anything to help me achieve my goals, I couldn't have done this without you. To my husband Ryan and beautiful daughter Elisa, your love is the rock that I lean on—thank you for giving my life more meaning than I knew possible. To the Connollys, you have taken the "inlaw" off of daughter and sister and given me invaluable support.

For the countless other people who have touched my life along the way, thank you.

Abstract

Advances made pertaining to strong interactions between single photons of light and single atoms have great potential in the field of quantum information. However, scalability is a limiting factor in the applicability of current technologies (such as an atom in the mode of a Fabry-Perot resonator) due to difficulties in alignment and fabrication. Toroial resonators, however, are fabricated lithographically on silicon wafers, and are therefore easily scalable. Light is coupled into a toroid by tapered optical fiber, allowing for the efficient retrieval of photons from the resonator mode that is necessary if multiple resonators are to be eventually coupled to one another. We have demonstrated interactions between single atoms of cesium and a toroidal resonator that lie in the regime of strong coupling since the rate of coupling between an atom and the cavity mode, ${g_0}^m = (50 \pm 12)$ MHz, is much larger than the dissipative rates of the system $(\gamma, \kappa)/2\pi \approx (2.6, 18)$ MHz. To further expand upon the usefulness of toroids in cavity QED, I have striven to improve the way that toroids are characterized and coupled. An apparatus which semi-automates the characterization process reduces the length of time a toroid is outside of vacuum, thus limiting environmental degradation. To help in better understanding the process of pulling tapered fibers, the efficiency and characteristic quantities have been detailed. Similarly, the behavior of a toroid resonance as a function of coupling strength was quantified. Preliminary locking of the coupling by controlling the separation between the taper and toroid has been accomplished. This locking will allow the next generation of atom-toroid coupling to require less human intervention and therefore be more efficient.

Contents

List of Figures

Chapter 1

Introduction

Historically, our group has made pioneering advances in cavity quantum electrodynamics (cQED) using Fabry-Perot resonators to build up strong, localized fields from single photons which can interact with single atoms [1, 2, 3, 4]. However, the scalability of these systems is limited, as is their ability to efficiently be combined into fiber-based networks, since they are inherently free-space devices. A single Fabry-Perot is extremely difficult to build and align, as the spacing between mirrors must be maintained to 10^{-14} m. Therefore the prospect of building a network of multiple resonators of this type — as is desired in quantum information — is not promising. A first attempt at combating this problem was to use a small, solid-state microsphere resonator [5, 6], whose one-piece design is inherently more stable than the traditional two-mirrored resonators previously used. However, the geometry of a sphere causes the mode volume to be relatively large [7, 8], limiting the achievable rate of coupling — which is inversely proportional to the mode volume — between an atom and a photon in the resonator. In the fall of 2003, shortly after my arrival in Jeff Kimble's Quantum Optics Group, a new experiment was proposed that had the potential to address these issues and thereby push the limits of cQED.

Microtoroidal resonators [9, 10] were the latest achievement to come out of Kerry Vahala's group at Caltech and showed great promise for probing the physics of cQED. These resonators, shown in the inset of Figure 2.3, support a whispering gallery mode [11], as do microspheres, in which the light is trapped in the resonator mode via total internal reflection. The nature of this total internal reflection gives rise to modes

which lie near the outer surface of the structure, a portion of which reside outside the physical structure as an evanescent wave. As shown in Figure 2.2b, it is with this evanescent field that atoms will interact. Microtoroids have very small mode volumes due to their toroidal geometry — which is comparable to a small portion of the azimuthal angle in a microsphere — and are inherently scalable since they are fabricated lithographically on silicon chips. Finally, the Vahala group greatly improved the method of coupling light in and out of a whispering gallery mode resonator — previously done in free-space using a carefully positioned prism and free-space beam — by using the evanescent field of tapered optical fibers. These fibers are compact and, by nature, easily and efficiently integrable into a larger fiber-based network.

1.1 My History in the Group

At the time that I joined the group, this experiment of using toroidal cavities for cQED was in its infancy. Working with graduate students Kok Win Goh (Win) from our group and Tobias Kippenberg and Sean Spillane from the Vahala group, I was able to participate in the design of this new experiment from the beginning. Simulations performed by Sean, and the discussions which followed, determined that these toroids would not only be suitable for cavity QED, they could also greatly improve upon the current standards. Specifically, at the time of publication of the manuscript [12], the highest rate of coupling, $g/2\pi$, between an atom and a Fabry-Perot cavity was 110 MHz, while the simulations showed that toroids should be capable of achieving $g/2\pi > 700$ MHz. Further, the toroidal cavities have the potential to be far more sensitive in detecting atoms, with critical photon and atom numbers as low as $6\text{x}10^{-6}$ and $2\text{x}10^{-7}$, respectively. For comparison, the projected theoretical limits of Fabry-Perot cavities of the same values are $5.7\text{x}10^{-6}$ and $1.9\text{x}10^{-4}$, showing substantial improvement in the critical atom number for toroids. The rate of optical information for toroids, for judicious choice of geometry, can theoretically be as high as $1.6\text{x}10^{8}$ Mbits/sec compared to the theoretical projection of $1.7\text{x}10^{5}$ Mbits/sec for Fabry-Perot resonators [13, 12]. Clearly, these resonators demonstrated a great enough potential

in the field of cavity QED for us to build an apparatus to test the theory.

During these beginning months, based on the preliminary goal of simply determining whether a whispering gallery mode resonator could indeed interact strongly with single atoms (which had never been done before), we decided to operate with the tapered fiber in contact with the toroidal resonator rather than attempting to control the separation to < 100 nm. This decision allowed us to use a simple positioning system and focus our energies on obtaining a signal-to-noise ratio high enough to be able to detect the extremely small signals caused by single atoms. A further self-imposed limitation on the scope of this first experiment involved trapping of atoms. Since trapping atoms in the mode of a resonator is extremely difficult, and we were attempting to design the simplest experiment which would allow us to couple atoms and toroids, if even for a very short time, we decided to only watch for atoms as they fell by the resonator in the field of gravity.

Learning from Win (and starting with an empty optical table), we designed and built the first version of the vacuum chamber that would ultimately house the experiment from Chapter 2, in which we observed interactions between single atoms and a toroidal resonator. From Win, I learned the basics of operating an experiment under ultra high vacuum, including cleaning procedures [14] and fundamental chamber design principles. Further, since my background was in solid-state physics, he instructed me in the ways of optical physics, from how to clean optics to building a diode laser.

Designing a chamber in which forming a MOT would be possible, while allowing for coupling between the tapered fiber and toroid, proved to be difficult. A significant portion of my first year was spent designing the configuration of the vacuum chamber, as well as the components which would go inside. Due to the many constraints imposed by beams, imaging systems, positioning equipment, and many other factors that came up in the course of designing, I developed a full-scale, three-dimensional model of the vacuum chamber and all components which would go inside (see Appendix A). Given the number of virtual test runs that failed for various reasons, such as discovering that parts which operated beautifully once in the chamber were too

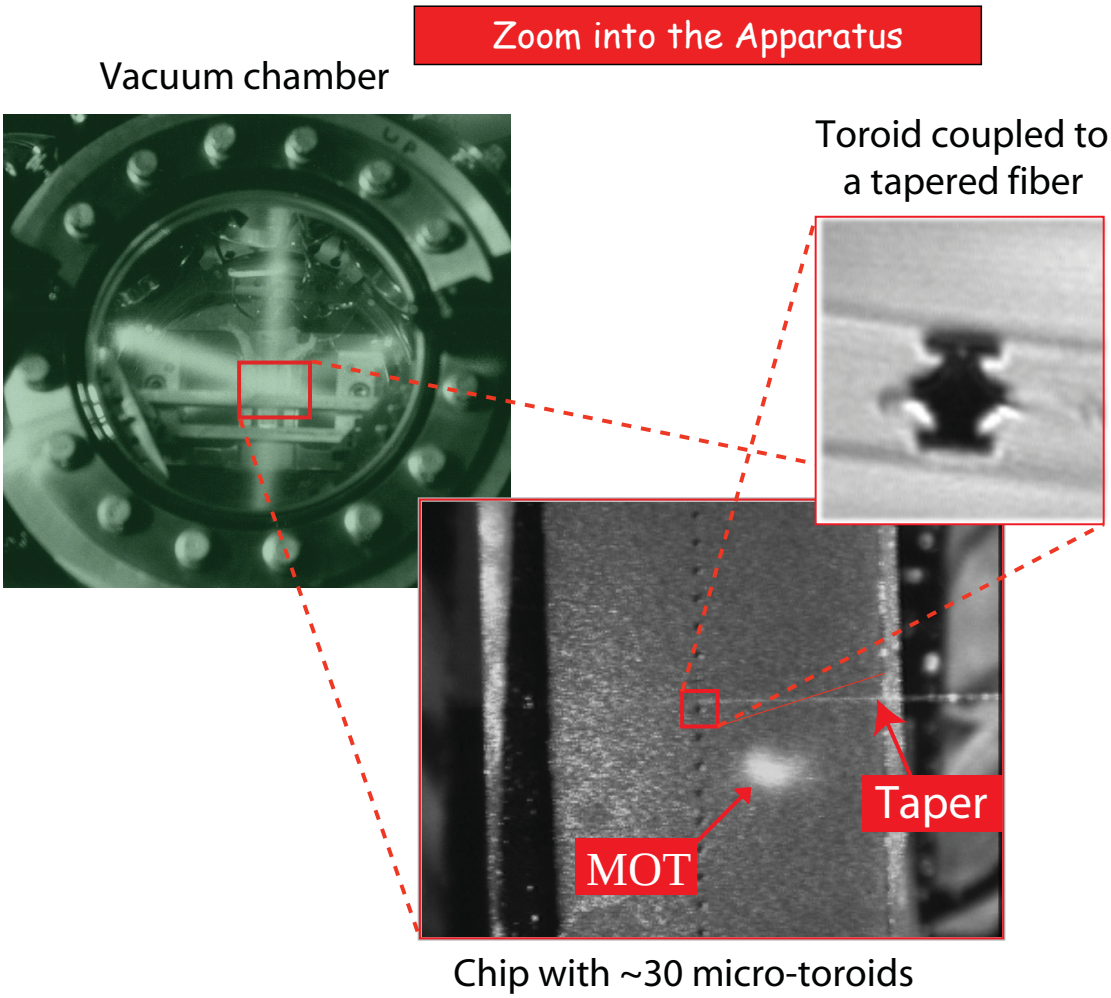

Figure 1.1: Photographs of our vacuum chamber at various levels of zoom. The far-left photo, taken by Nara Cavalcanti, shows the view from above our chamber with the MOT beams made visible by flooding the chamber with cesium. The next level of zoom shows the toroid chip (which has approximately thirty resonators), taper, and MOT. In practice, the MOT is aligned, using a view such as this, to lie above the chosen toroid so that the most dense region of the atom cloud passes through the mode of the coupled resonator. Finally, the most magnified image is of a toroid located in the chamber coupled to a tapered fiber.

large to fit in the chamber openings, this step saved valuable time and resources.

In 2004, Win moved on from our group, and Warwick Bowen, Takao Aoki, and Matt Eichenfeld joined the project. They instilled in me their wisdom of atomic physics and cavity QED. Through much effort, we were able to build our first MOT and successfully put a taper and toroid into the vacuum chamber. Figure 1.1 shows the experiment as viewed from above the vacuum chamber. In the far-left photo, the MOT beams are visible as they cross above the toroid chip, which contains about thirty resonators. While Warwick, Matt, and Takao took the primary roles in building a MOT in our new chamber, I studied under Tobias to learn all that I could about toroidal resonators. From Tobias I learned to manufacture toroids that have high quality factors and also to pull high efficiency tapers. I learned the intricacies of how toroids work, among them tricks to obtain efficient coupling between a taper and a toroid (Chapter 4). Due to this invaluable experience I became the official toroid coupler in our group for the next few years.

Over the next year we tried, without success, to observe single atoms interacting with the toroid mode. Despite the fact that we were unable to see atoms transiting the mode due to a high noise floor and saturated atoms, I was able to learn how to build and optimize a MOT from my colleagues Matt, Warwick, and Takao. By the summer of 2005 our group consisted of Barack Dayan, Takao, and me, as Matt and Warwick left to pursue other avenues. Barack was instrumental in helping us to change our detection scheme from heterodyne detection, which had many drawbacks that are detailed in Section 2.3.4, to single photon counters, which allowed us to detect much lower light levels. He also introduced me to the power of Labview in controlling an experiment and acquiring data.

In 2006, with a more automated experiment, lower number of intracavity photons (Section 2.3.4), and — through practice — better degree of critical coupling (which gives a darker background and therefore an improved signal-to-noise ratio), we finally observed single atom transits (Chapter 2.2). Now that we had a signal to optimize, we were able to perform various experiments in order to quantify the degree of coupling between the atom and cavity. The standard method for determining this coupling

strength is to record the spectra of a resonance when the atom is present, since the resonance of the toroid is predicted to split from a single Lorentzian into two, separated by the rate of coupling between the atom and cavity g_0[1]. However, since our atom transits are very short ($\simeq 2\mu$s) and produce only about 10 photons, this is not feasible. Through valuable collaborations with Scott Parkins, we developed alternate methods of determining the coupling strength. Ultimately, we used a theory developed by Scott (Section 2.2) in which the number of atom transits above a given threshold, are plotted as a function of atom-cavity detuning, and fit to the theoretical curves that correspond to various values of the "maximally accessible g_0," ${g_0}^m$ [2]. In doing so, we determined that the ${g_0}^m$ of our toroid was $\simeq 50 \pm 12$MHz. Since this is larger than any of the dissipative rates in the system, we are considered to be in the regime of "strong coupling." These findings were published in reference [15] and presented at the 2006 International Conference on Atomic Physics.

In the years since these results were obtained, I have worked somewhat independently on smaller projects pertaining to tapers and toroids. Tapering of efficient optical fibers has essentially been an art form in our group due to the large number of variables with few signals providing feedback. For the last two years, in the process of pulling many tapers, I have recorded the behavior of each pull in an attempt to quantify the behavior of tapering fibers as a function of such factors as pull length and oscillations. It has been shown that as the rate of change of the radius of a taper approaches adiabaticity, the efficiency increases [16, 17]. Consistent with this, I found that efficiency increased as the length of the pull region increased (Chapter 3). Further, as oscillations in the transmission as a function of pull length (due to interference with higher-order modes) decreased, the efficiency again increased.

Another project I undertook was to improve the method of characterizing toroids (Chapter 4). Since the quality factors of toroids decrease while exposed to atmo-

[1]The resonance will only split by g_0 for an atom in a location that allows it to be optimally coupled to the toroid mode. In reality, this rate of coupling g is a function of position which decays as the distance from the surface is increased.

[2]We fit to the "maximally accessible g_0" because the actual maximum g_0 is the coupling strength at the surface of the toroid. Since the toroid is made of silica, a dielectric, atoms cannot reside too close to the surface without impact due to the van der Waals force. This is detailed in Section 2.2.

spheric conditions (thought to be due to water absorption [18]), it is crucial that they spend as little time outside of vacuum or dry box as possible. Therefore, there is a need to be able to quickly locate and record all resonances of a particular toroid. This way, it can be analyzed at a later time while safely stored under vacuum. By semi-automating this procedure and using the error signal of the toroid transmission, rather than the transmission itself, toroids can be characterized very quickly. A given toroid can have all resonances, over a full free spectral range (FSR), recorded in less than one minute, whereas previous methods took several minutes to record a small fraction of an FSR. The error signal allows us to find small resonances out of the noise when the toroid is very weakly coupled. This greatly eases the process of finding resonances that are several megahertz wide in data that is taken over more than ten nanometers.

While characterizing toroids, I observed how characteristics of the resonances change as the strength of coupling is varied (Chapter 5). I acquired data by smoothly scanning the separation between the taper and toroid while recording the spectrum of a resonance. The data from the resonance, at each separation of taper and toroid, was then fit to a pair of Lorentzians[3] in order to obtain the width, separation, frequency shift, and depth of the resonance as a function of coupling strength. With the exception of the resonance depth, which increases until critical coupling and then recedes, all values seemed to increase exponentially, albeit at different rates. While the increase in width and change in depth are due to increased coupling from the taper, the increase in modal splitting is theorized to be due to an increase in scattering off the surface of the tapered fiber. Further, the shift in resonance frequency is due to the presence of the taper, an additional volume of silica, in the mode of the toroid.

Finally, in an effort to ultimately couple a taper to the toroid in the vacuum chamber without contacting one to another, the separation between the taper and toroid must be actively controlled by a feedback system. By mechanically isolating the coupling apparatus and implementing a simple locking circuit, I, together with

[3]The data was fit to a pair of Lorentzians rather than a single one due to the modal coupling that occurs in the toroid [19].

Daniel Alton, have succeeded in suppressing the drift that occurs below $\simeq$2 Hz by as much 10 dB (Chapter 6). While improvements need to be made in order to suppress higher frequency noise, this achievement allows us to maintain an arbitrary degree of coupling for over an hour, without human intervention. Previously, the separation would drift and require manual adjustment within a matter of minutes, if not sooner.

Chapter 2

Observation of Strong Coupling Between One Atom and a Monolithic Microresonator

2.1 Goal and Scope of Original Experiment

The purpose of this initial experiment was to demonstrate that strong coupling between single atoms and a whispering gallery mode resonator could indeed be achieved. When an atom enters into the mode of a cavity, in our case a toroidal resonator, a coupling occurs between the components of the system. As per the Jaynes-Cummings model [20], the cavity mode and a single atom exchange excitation by way of a single quantum at a rate g_0, where $2g_0$ is the single photon Rabi frequency [21]. If this exchange of excitation, g_0, occurs more rapidly than any of the dissipative rates in the system, then we are considered to be in a regime known as strong coupling between the atom and cavity [22, 23]. This coupling manifests itself in a splitting in the energy levels of the system. Specifically, when no atom is present, the spectrum of a single resonance of the toroid is given by a single Lorentzian[1]. However, when an atom couples to the cavity, this Lorentzian splits symmetrically into two such line shapes, separated by the single-photon Rabi frequency $2g_0$, in a phenomenon known as Rabi splitting. In this experiment, we looked to design the simplest configuration which would enable us to observe such phenomena.

[1]In actuality, the toroid supports two standing wave modes, manifest in two Lorentzians rather than one. This behavior is described in Section 5.1.3 and reference [19].

Our strategy for observing atoms is to probe the cavity spectrum and look for deviations characteristic of eigenvalues of the atom-cavity system. To do this we will inject a weak laser into the mode of the cavity, tuned to a resonance that is made to coincide with a particular energy level of cesium. When an atom is present, the resonance exhibits the characteristic Rabi splitting, causing it to no longer coincide with the frequency of the probe laser. Once the atom leaves the toroid mode the probe laser is once again at the same frequency as the toroidal resonance. The probe laser manifests this atom "transit" through the mode as a change in optical power detected at the output of the toroid. This is portrayed in Figure 2.1.

Our first technical difficulty was the short interaction time between an atom and the toroid mode. Ideally, an atom will be trapped in the mode of the toroid, giving a long temporal signal with which to probe the coupled spectra. However, this is extremely difficult to accomplish, particularly for a whispering gallery mode resonator. The external accessible mode of a whispering gallery mode resonator is much smaller than previous cavities used for cavity quantum electrodynamics. A Fabry-Perot cavity, for example, has been used to trap atoms [1] with much success; however, the region of trapping is much larger and less restrictive than that of a toroid. Unlike that of a toroid, the standing wave structure of the Fabry-Perot mode has many antinodes that reside between the two mirrors, far from the dielectric surfaces. A toroid mode is an evanescent field which decays exponentially as the distance from the surface. This means that the strongest mode lies at the surface, with the strength dropping off dramatically as one moves hundreds of nanometers away. However, the van der Waals force tens of nanometers away from the surface is strong enough to cause any atoms this close to bombard the toroidal surface, terminating any interaction that would have occurred with the mode of the cavity. While these challenges are being undertaken in future generations of the experiment, for this trial we chose to forgo trapping and limit ourselves to the observing signals caused by atoms falling with gravity through the mode of the toroidal resonator.

Our second hurdle to overcome was maintaining the proper separation between the taper and toroid to within less than one micron deviation. Rather than design a

sophisticated positioning system (as we are doing for the next generation, described in Section 4.2.4), we opted to operate with the the taper contacted to the toroid, i.e., in "contact mode." While this mode is easier to control, as drift and vibrations in taper-toroid separation are not a factor, it does limit the modes to which we are able to couple, as well as limit the lifetime of the toroid due to repetitive impact from the taper. However, for the scope of this experiment, the benefits in separation stability outweigh these disadvantages.

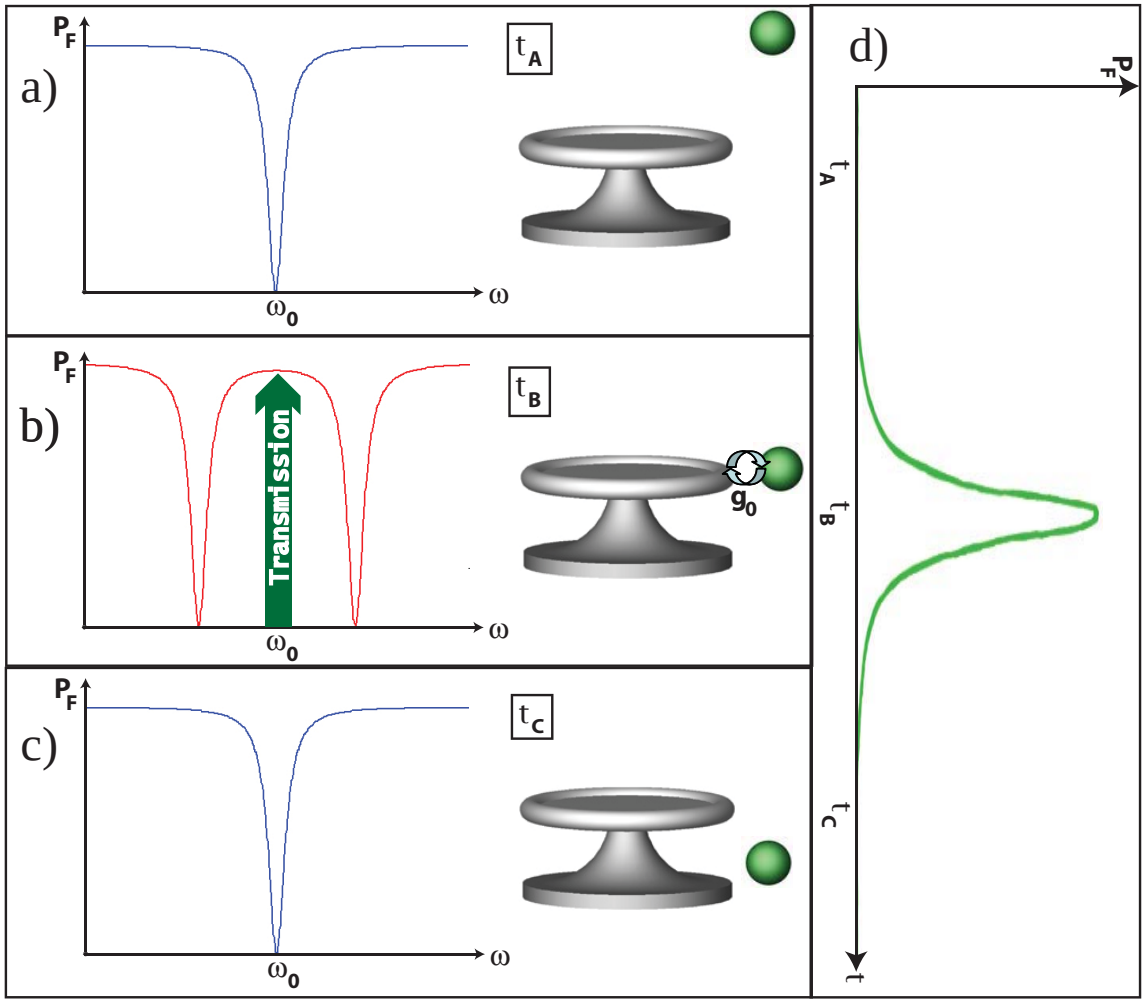

Figure 2.1: Diagram of an atom transiting the mode of a toroid. The left-hand side shows the spectrum of a particular toroid resonance at the output of the taper, denoted by P_F, for different atom locations. Our probe laser is locked to the bottom of the resonance at frequency ω_0. (a) The resonance is unaffected by the atom when it is far above the toroid. Therefore, the probe laser remains on resonance, with zero output transmission. (b) The atom move through the toroid mode and exchanges excitations at the rate g. The resonance splits about ω_0 by g, causing the probe at ω_0 to no longer be resonant and a spike of transmission to occur. (c) The atom passes by the toroid, the original resonance is restored and the probe output once again is zero. (d) The temporal profile of an atom transit. The transmission through the taper, P_F, starts at zero when the atom is far above the toroid at time t_A, increases to a maximum when the atom is closest, and thus most strongly coupled, to the mode at time t_B, and finally drops back to zero once the atom falls away at time t_C.

2.2 Experimental Results [2]

Over the past decade, strong interactions of light and matter at the single-photon level have enabled a wide set of scientific advances in Quantum Optics and Quantum Information Science. This work has been carried out principally within the setting of cavity quantum electrodynamics (QED) [22, 23, 24, 25] with diverse physical systems [7], including single atoms in Fabry-Perot resonators [22, 26], quantum dots coupled to micropillars, photonic bandgap cavities [27, 28], and Cooper-pairs interacting with superconducting resonators [29, 30]. Experiments with single, localized atoms have been at the forefront of these advances [2, 3, 31, 4, 32], utilizing optical resonators in a Fabry-Perot configuration with finesse $F \sim 10^5 - 10^6$ [33]. Due to the extreme technical challenges involved in further improvement of the multilayer dielectric mirror coatings [13] and in scaling to large numbers of such resonators, there has been increased interest in the development of alternative microcavity systems [7]. Here, we demonstrate strong coupling between individual cesium atoms and the fields of a high-Q toroidal microresonator. From observations of transit events for single atoms falling through the resonator's evanescent field, we determine $g_0^m/2\pi \approx (50 \pm 12)$ MHz for interactions near the surface of the resonator, where $2g_0^m$ is the single-photon Rabi frequency. Strong coupling $g_0^m > (\gamma, \kappa)$ is thereby demonstrated for the interaction of single atoms and optical photons in a monolithic resonator, where $(\gamma, \kappa)/2\pi \approx (2.6, 18)$ MHz are the dissipative rates for atom and cavity field. Our work opens a new avenue for investigations of optical processes with single atoms and photons in lithographically fabricated microresonators. Applications include the implementation of quantum networks [34, 35], scalable quantum logic with photons [36], and quantum information processing on atom chips [37].

The realization of large-scale quantum networks [34, 35] requires the capability to interconnect many "quantum nodes," each of which could consist of a microresonator containing a set of trapped atoms. The "quantum channels" to connect these nodes would be optical fiber, with strong interactions in cavity QED providing an efficient

[2] Significant portions of this text are taken from our paper "Observation of strong coupling between one atom and a monolithic microresonator" [15].

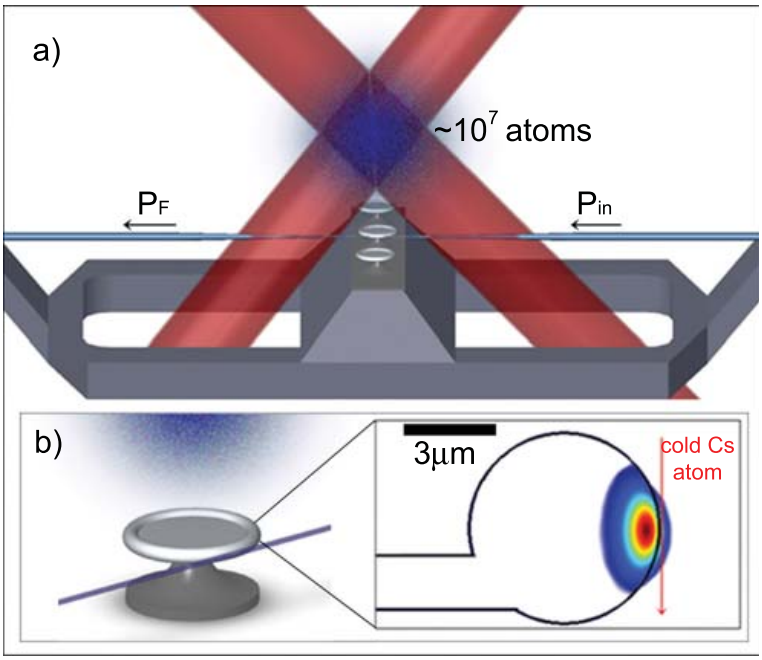

Figure 2.2: (a) Simple schematic of the experiment showing a cloud of cold cesium atoms and associated trapping lasers above an array of microtoroidal resonators. Light from the probe beam P_{in} is coupled into a resonator by way of the fiber taper, with the forward propagating output P_F coupled into the taper. (b) Illustration of an SiO_2 microtoroidal resonator, fiber taper, and atom cloud above. The calculated field distribution for the lowest order resonator mode is shown by the color contour plot on the right. Cold cesium atoms fall through the external evanescent field of this mode and are thereby strongly coupled to the resonator's field.

interface between light and matter. This chapter provides a critical step towards a feasible quantum network by demonstrating strong coupling of single atoms to microresonators which are fabricated on silicon wafers in large numbers by standard lithographic techniques followed by a laser-reflow process [9]. Combined with the capability to couple light efficiently to and from such cavities directly via a tapered optical fiber [38], toroidal microcavities offer promising capabilities for new nonlinear interactions of single atoms and photons across distributed networks.

Our efforts follow the pioneering work of V. Braginsky [11] and later works [5] by employing the whispering-gallery modes (WGMs) of fused silica microtoroidal resonators [12]. As depicted in Figure 2.2, a silicon chip containing a collection of 35 microtoroidal resonators is located inside a vacuum chamber at 10^{-9} Torr and is

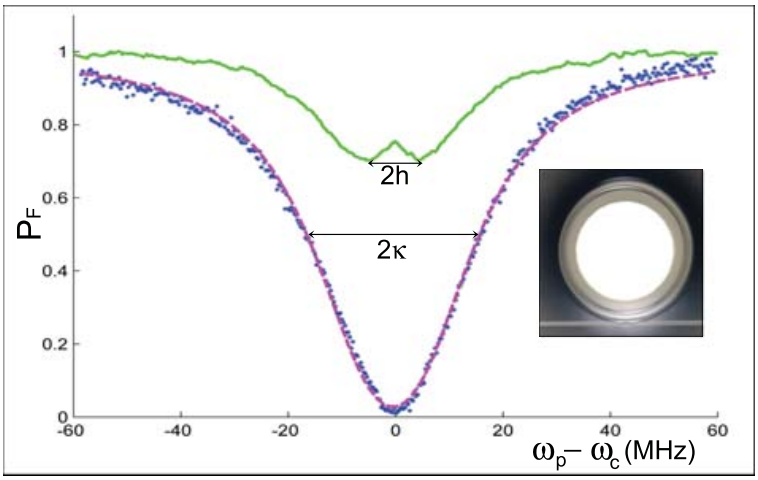

Figure 2.3: Cavity transmission function $T_F = P_F/P_{in}$ as a function of probe frequency ω_p. The lower trace is taken for critical coupling; the upper trace for conditions of under-coupling [38]. From fits to such traces for critical coupling (dashed curve), we find $(\kappa, h)/2\pi = (17.9 \pm 2.8, 4.9 \pm 1.3)$ MHz, with κ, h being the overall cavity field decay rate and the scattering-induced coupling between two counter-propagating modes of the microtoroid, respectively (see reference [19] for more details). Inset: Photograph of a microtoroid and coupling fiber

positioned to couple a particular resonator to a tapered fiber. The toroids have major diameter $D \simeq 44$ μm and minor diameter $d \simeq 6$ μm [12]. By judicious choice of the point of contact between the surface of the resonator and the tapered fiber, we attain critical coupling, in which the forward propagating power P_F in the fiber drops to near zero for the probe frequency ω_p equal to the cavity resonance frequency ω_C [38]. Measurements of the cavity transmission in the absence of atoms are presented in Figure 2.3. Note that the forward flux P_F and associated transmission spectrum T_F are analogous to the reflected flux and reflection spectrum from a Fabry-Perot cavity [38].

By varying the temperature of the silicon chip, the detuning $\Delta_{AC} \equiv \omega_A - \omega_C$ between ω_C and the atomic resonance at ω_A ($6S_{1/2}, F = 4 \longrightarrow 6P_{3/2}, F' = 5'$ transition in cesium) can be controlled with uncertainty $\simeq \pm 2$ MHz (see Section 2.4.1).

Cold atoms are delivered to the vicinity of the toroidal resonator from a small cloud of cesium atoms cooled to $T \simeq 10$ μK and located 10 mm above the silicon chip. Every 5 seconds, the cloud is dropped, resulting in about 2×10^6 atoms in a

3 mm ball at the height of the chip, with then a few dozen atoms passing through the external evanescent field of the toroidal resonator. By way of two single-photon detectors (D_{F1}, D_{F2}) (see Section 2.4.2), we continuously monitor the forward propagating signal P_F from a frequency-stabilized probe beam P_{in} coupled to the toroidal resonator. The interaction of each individual atom with the evanescent field destroys the condition of critical coupling, leading to an increase in P_F. The measurement cycle then repeats itself for 2.5 seconds for a reference measurement, this time with no atomic cloud formed above the microtoroid.

Figure 2.4 displays typical records $C(t)$ for the number of single-photon detection events within time bins of $\delta t = 2\ \mu s$ as functions of time t for the forward signal $P_F(t)$. Measurements are displayed (a) with and (b) without atoms for the case of equal probe and cavity frequencies, $\omega_p = \omega_C$, for $\Delta_{AC} \simeq 0$, and with mean intracavity photon number $\bar{n}_0 \simeq 0.3$ for the forward circulating mode of the toroidal resonator a (see Section 2.4). The traces in both (a) and (b) exhibit background levels that result from the nonzero ratio $P_F/P_{in} \sim 0.005$ at critical coupling in the absence of atoms. However, Figure 3a clearly evidences sharp peaks of duration $\Delta t \approx 2\ \mu$s for the forward propagating light $P_F(t)$, with an individual peak shown more clearly in the inset. Each event arises from the transit of a single atom through the resonant mode of the microtoroid, with approximately 30 events per cycle observed. Figure 2.4c examines the temporal profile of transit events in more detail by way of the cross correlation $\Gamma(\tau)$ of photoelectric counts $C_1(t_1), C_2(t_1 + \tau)$ from the detectors (D_{F1}, D_{F2}) for P_F (see Section 2.4.2). This result agrees reasonably well with the theoretical prediction for atom transits through the calculated field distribution shown in Figure 2.2b.

By applying a threshold requiring $C(t) \geq 6$ counts for $C(t)$ as in Figure 2.4(a, b), we find the average time dependence $\bar{C}_{\geq 6}(t)$ over ~ 100 measurement cycles. Figure 2.4d displays the results both with and without atoms, with the average counts $\Sigma_6(t)$ derived from $\bar{C}_{\geq 6}(t)$ by summing over successive time bins $\delta t = 2\ \mu$s for 1 ms intervals. The peak in transit events is consistent with the expected distribution of arrival times for atoms dropped from our atom cloud. By contrast, negligible excess events (i.e.,

$C(t) \geq 6$) are recorded for the cases without atoms.

Focusing attention to the central region indicated by the dashed lines in Figure 2.4d, we examine in Figure 2.4e the probability $P(C)$ to record C counts within $\delta t = 2$ μs. Evidently, when the atom cloud is present, there is a statistically significant increase (of at least fifteen sigma) in the number of events with $C \geq 4$. These are precisely the events illustrated by the inset in Figure 2.4a and the cross correlation in Figure 2.4c, and are associated with single atom transits near the surface of the toroidal resonator. By varying the value of $\bar{n}_0$, we have confirmed that the large transit events evident in Figure 2.4 are dramatically reduced for $\bar{n}_0 \gtrsim 1$ photon, which indicates the saturation of the atom-cavity system.

A quantitative description of our observations in Figure 2.4 of individual atom transits requires the development of a new theoretical model in cavity QED. In reference [19], a model is presented which shows that the underlying description of the interaction of an atom with the fields of the toroidal resonator is in terms of normal modes (A, B) (see reference [19]), which have mode functions $\psi_{A,B}(\rho, x, z)$ that are standing waves $(\cos kx, \sin kx)$ around the circumference x of the toroid, with ρ the radial distance from the surface and z the vertical coordinate. $\psi_{A,B}(\rho, x, z)$ have peak coherent coupling $g_0/2\pi = 70$ MHz for the lowest order modes of our resonator, such as illustrated in Figure 2.2b. These normal modes result from coupling of two oppositely directed traveling waves by scattering at rate h, with the resulting mode splitting manifest in Figure 2.3. Note that the presence of two normal modes leads to a $\sqrt{2}$ increase in the coupling constant in our case as compared to the one predicted by the Jaynes-Cummings model for an atom interacting with a single traveling wave mode (see reference [19] for further details).

Guided by this theory, we have carried out a series of measurements as in Figure 2.4 to determine the coherent coupling rate g_0 for interactions of single atoms with our toroidal resonator, but now with various values of the atom-cavity detuning Δ_{AC}, keeping the probe resonant with the cavity: $\omega_C \approx \omega_p = \omega_A + \Delta_{AC}$. The qualitative idea is that large single-atom transit events will occur only over a range of detunings $|\Delta_{AC}| \lesssim g_0$. Specifically, the decrease in the forward transmission T_F induced by

atom transits as a function of Δ_{AC} is described by a Lorentzian with width β set by g_0 (see Section 2.4). The eigenvalues of the atom-toroid coupled system are drawn in Figure 2.5A relative to the cavity resonance (blue, dashed). In this representation the atom (red, dashed) has positive energy detuning for negative values of Δ_{AC}, and negative detuning for positive values of Δ_{AC}. The coupling with the atom lifts the degeneracy between the atom and the cavity at Δ_{AC}, leading to the expected splitting of $2g$ between dressed states #1 and #2. However, since the atom is never fully coupled to both normal modes (A,B), a third dressed state (#3, green) remains practically unchanged by the atom. This three mode structure is represented in Figure 2.5(B), which describes the forward flux T_F at fixed $\Delta_{AC} = 0$ as a function of the probe frequency, demonstrating maxima points at 0 and $\pm g$. Similarly, the coupling strength manifests itself in the dependence of T_F on Δ_{AC}, as shown in Fig 2.5(C) for probe frequency fixed to the cavity resonance, as is the case in our experiment. Thus, the decrease in the forward flux T_F at the cavity resonance $\omega_p = \omega_C$ as a function of the cavity-atom detuning Δ_{AC} is a generic feature of the eigenvalue structure of the system.

In our case, $g_0 = g_0(\rho, x, z) \approx g_0(\rho, x, Vt)$, where V is the velocity of the dropped atoms in the z direction. Thus, a numerical integration was performed over ρ, x, and t in order to derive the theoretical expectation for $T_F(\Delta_{AC})$, presented in Figure 2.6a for three values of g_0^m, where g_0^m is the maximal coupling that an atom can experience in its interaction with the cavity modes. Indeed, we see that the width β grows monotonically with g_0^m. However, the average value of T_F is not a parameter that is readily measured in our current experiment, where we expect many short individual transits, some of which are too weak to be distinguished from the background noise (Figure 2.4e). A parameter that describes our actual experimental measurements more closely is the probability to obtain a transit which results in transmission above a certain threshold. Obviously the two measures are closely related, such that this probability decreases with detuning Δ_{AC} in the same fashion as does T_F.

Figure 2.6b–d presents the results of our measurements for the average number of transit events per atom drop, $N_{drop}^{av}(C \geq C_0)$, which have photoelectric counts greater

than or equal to a threshold value C_0 for a set of seven detunings Δ_{AC}. In accord with the expectation set by Figure 2.6a, there is a decrease in the occurrence of large transit events for increasing Δ_{AC} in correspondence to the decrease in the effective atom-cavity coupling coefficient for large atom-cavity detunings.

The full curves shown in Figure 2.6b–d are the results of theoretical calculation for these measurements, with the relevant cavity parameters (κ, h) determined from fits as in Figure 2.3. We first ask whether the data might be explained by an effective value g_0^e for the coherent coupling of atom and cavity field, without taking into account the fact that individual atoms transit at radial distances ρ which vary from atom to atom. Figure 2.6b examines this possibility for various values of g_0^e, assuming a coupling coefficient $g_0^e \psi_{A,B}(x) = g_0^e[\cos kx, \sin kx]$ averaged along one period in x (as in Figure 2.6a). Apparently, an effective value $g_0^e/2\pi \approx 40$ MHz provides reasonable correspondence between theory and experiment for large events $C \geq 6$.

We adapt our theory to the actual situation of atoms arriving randomly at radial and circumferential coordinates by introducing a mesh grid over (ρ, x), and then computing the cavity transmission function $T_F(t)$ from $\psi_{A,B}(\rho, x, z(t))$ for atomic trajectories $z(t)$ over this grid. We also account for the time resolution $\delta t = 2$ μs of our data acquisition by a suitable average of $T_F(t)$ over such time bins (as was also the case in Figure 2.6b).

The results from these calculations are displayed in Figure 2.6c–d as the set of full curves for three values of coherent coupling g_0 for the cavity mode functions $\psi_{A,B}(\rho, x, z)$, where in b–d, the theory is scaled to match $N_{drop}^{av}(C \geq C_0)$ at $\Delta_{AC} = 0$. From such comparisons, we determine maximal accessible $g_0^m/2\pi = (50 \pm 12)$ MHz. Note that this conclusion is insensitive to the choice of cutoff C_0 over the range $4 \leq C_0 \leq 9$ for which we have significant transit events.

According to our calculations, the value of $g_0^m/2\pi = (50 \pm 12)$ MHz corresponds to the coupling rate expected at a distance of roughly 45 nm from the surface of the microtoroid. We estimate that due to the attractive van der Waals forces (see reference [39]), atoms which enter the evanescent field with a distance $\rho \leq 45\, nm$ from the microtoroid are expected to impact its surface in less than 1 μs, thus preventing

such atoms from generating appreciable transit events in the transmission function T_F.

To summarize, we have reported the first observation of strong coupling for single atoms interacting with an optical resonator other than a conventional Fabry-Perot cavity [22, 7, 26]. The monolithic microtoroidal resonators [9] employed here have the capability for input-output coupling with small parasitic losses, with demonstrated ideality in excess of 99.97% [38]. Moreover, quality factors $Q = 4 \times 10^8$ have been realized at $\lambda = 1550$ nm [10] and $Q \simeq 10^8$ at $\lambda = 850$ nm [12], with good prospects for improvements to $Q \simeq 10^{10}$ [6]. For these parameters, the efficiency for coupling single photons into and out of the resonator could approach $\epsilon \sim 0.99 - -0.999$ [38], while still remaining firmly in the regime of strong coupling [12]. Such high efficiency is critical for the realization of scalable quantum networks [34, 35] and photonic quantum computation [36]. Indeed, of diverse possibilities for the distribution and processing of quantum information with optical cavities [7, 27, 28], the system of single atoms coupled to microtoroidal resonators arguably provides one of the most promising avenues. Beyond efficient input-output coupling [38], strong coupling to a material system with long-lived internal states has now been demonstrated, albeit here in a primitive, proof-of-principle setting. Clearly, an outstanding technical challenge is to trap single atoms near the surface of the microtoroid, with one possibility having been investigated in reference. [40].

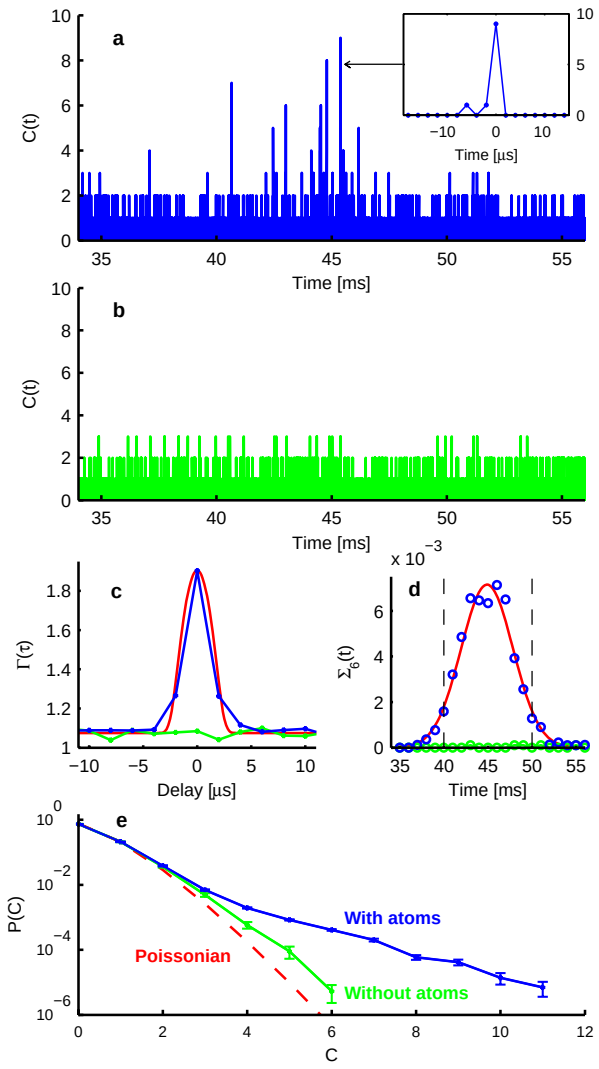

Figure 2.4: Measurements of the forward signal P_F in the presence of falling atoms (blue) and without atoms (green). (a, b) Single-photon counting events $C(t)$ as a function of time t after the release of the cold atom cloud at $t = 0$. $C(t)$ gives the total number of counts recorded for time bins of $\delta t = 2$ μs duration. (a) $C(t)$ for the case with atoms dropped and (b) $C(t)$ for the reference with no atom cloud. The inset in (a) shows the time profile for a single-atom transit. (c) Normalized cross correlation $\Gamma(\tau)$ of the forward signal counts from two detectors (D_{F1}, D_{F2}) showing the time profile associated with atom transit events. The smooth (red) curve is the theoretically predicted average cross correlation for a transit event with one atom, taking into account drop height of 10 mm and the spatial shape of the mode, as depicted in Figure 2.2(b). (d) Counts $\Sigma_6(t)$ obtained from $\bar{C}_{\geq 6}(t)$ by summing over 1 ms intervals, compared to a Gaussian distribution which fits the rate of atom transits assuming a 3 mm (FWHM) cloud of cold atoms dropped from 10mm above the microtoroid. (e) Probability $P(C)$ to detect C counts within $\delta t = 2$ μs bins for the central interval shown by the vertical dashed lines in (d), compared with Poissonian statistics with the same mean number of counts (~ 0.25 per 2 μs). The excess probability for large counts is predominately due to instability in the cavity temperature, which results in small fluctuations in the forward flux.

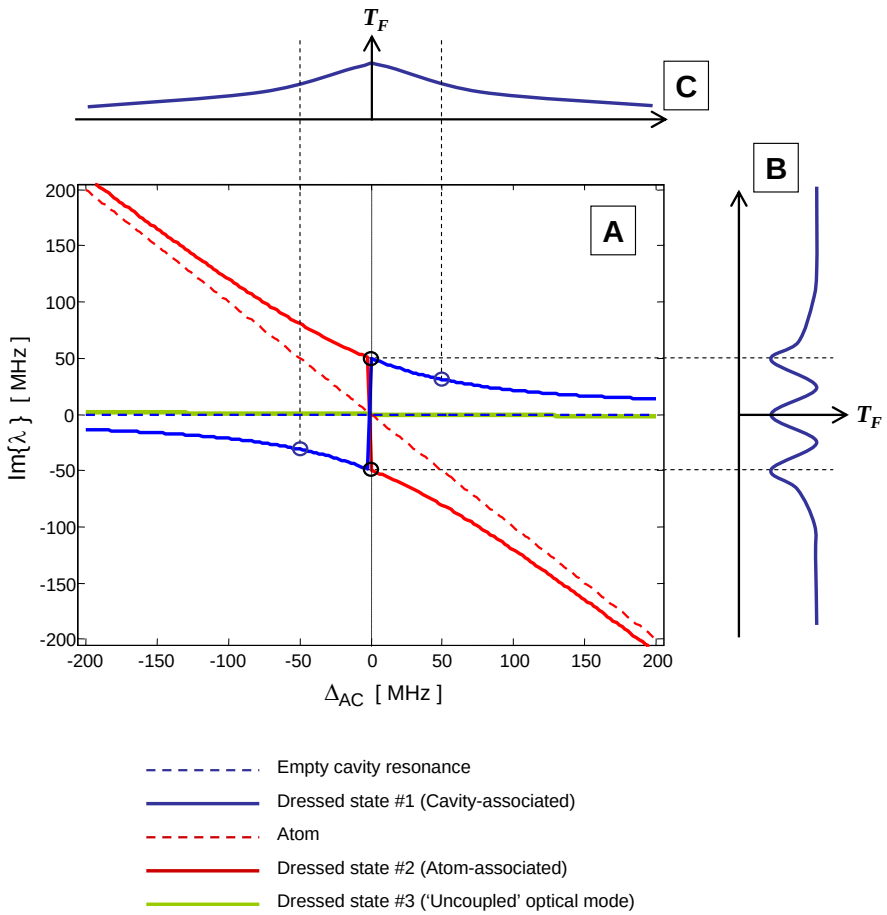

Figure 2.5: (A) The three eigenvalues of atom-toroid coupled system for (g,κ,h)=(50,18,5) MHz. (B) The forward flux T_F at fixed atom-cavity detuning $\Delta_{AC} = 0$ as a function of the probe frequency ω_p. (C) The forward flux T_F as a function of Δ_{AC}, with probe frequency fixed to be $\omega_p = \omega_C$.

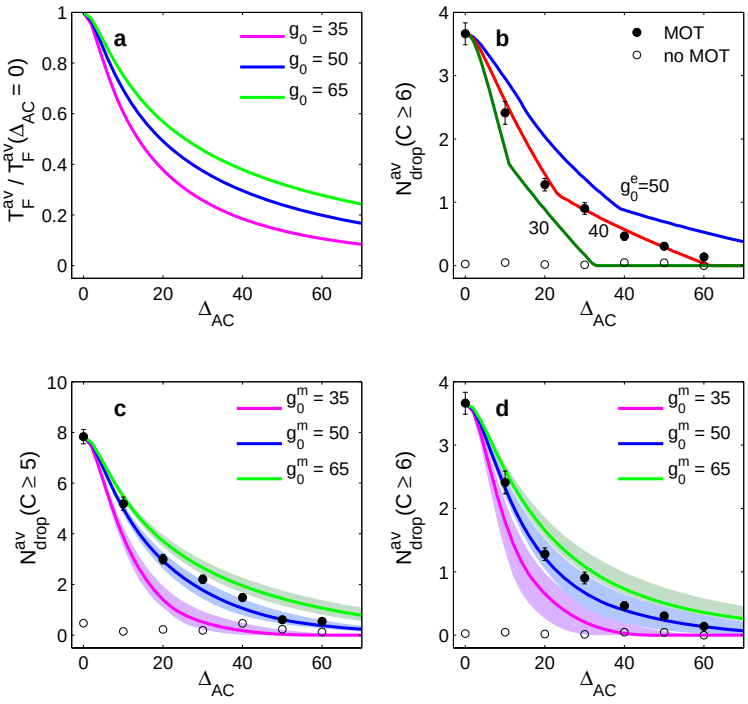

Figure 2.6: (a) Theoretical calculation for the average of the transmission $T_F(\omega_p = \omega_C)$ as a function of (Δ_{AC}, g_0). (b–d) Measurements for the average number of events per drop of the atom cloud $N_{drop}^{av}(C \geq C_0)$ versus the atom-cavity detuning Δ_{AC}, in the presence of atom (full circles) and without atoms (empty circles). (b, d) $C_0 = 6$; (c) $C_0 = 5$. The data are taken for probe frequency $\omega_C \approx \omega_p = \omega_A + \Delta_{AC}$. The full curves are theoretical results as discussed in the text. The widths of the curves are determined from the experimental uncertainties in (κ, h). (b) Theory for $N_{drop}^{av}(C \geq 6)$ without radial averaging to deduce an effective coupling $g_0^e/2\pi \approx 40$ MHz. (c–d) Theory for (c) $N_{drop}^{av}(C \geq 5)$ and (d) $N_{drop}^{av}(C \geq 6)$ with radial and azimuthal averaging leading to $g_0^m/2\pi \approx 50$ MHz

2.3 Experimental Design

Our apparatus, shown in Figure 2.7, consists of a vacuum chamber, various laser beam configurations, imaging systems, and motion control internal to the chamber. The substance of the experiment takes place inside the vacuum chamber, as this is where our resonator and atoms are located. The lasers have two purposes; one set is for trapping atoms above the resonator, the other is for probing the spectra of the resonator mode. The imaging is for aligning the resonator relative to the tapered fiber — which injects light into the resonator mode — as well as to the cloud of atoms. Finally, the resonator is on an apparatus which allows motion in all three spatial dimensions so that we can effectively control the overlap between its optical mode and that of the tapered fiber. Details pertaining to the design of each of these will be addressed in the following sections.

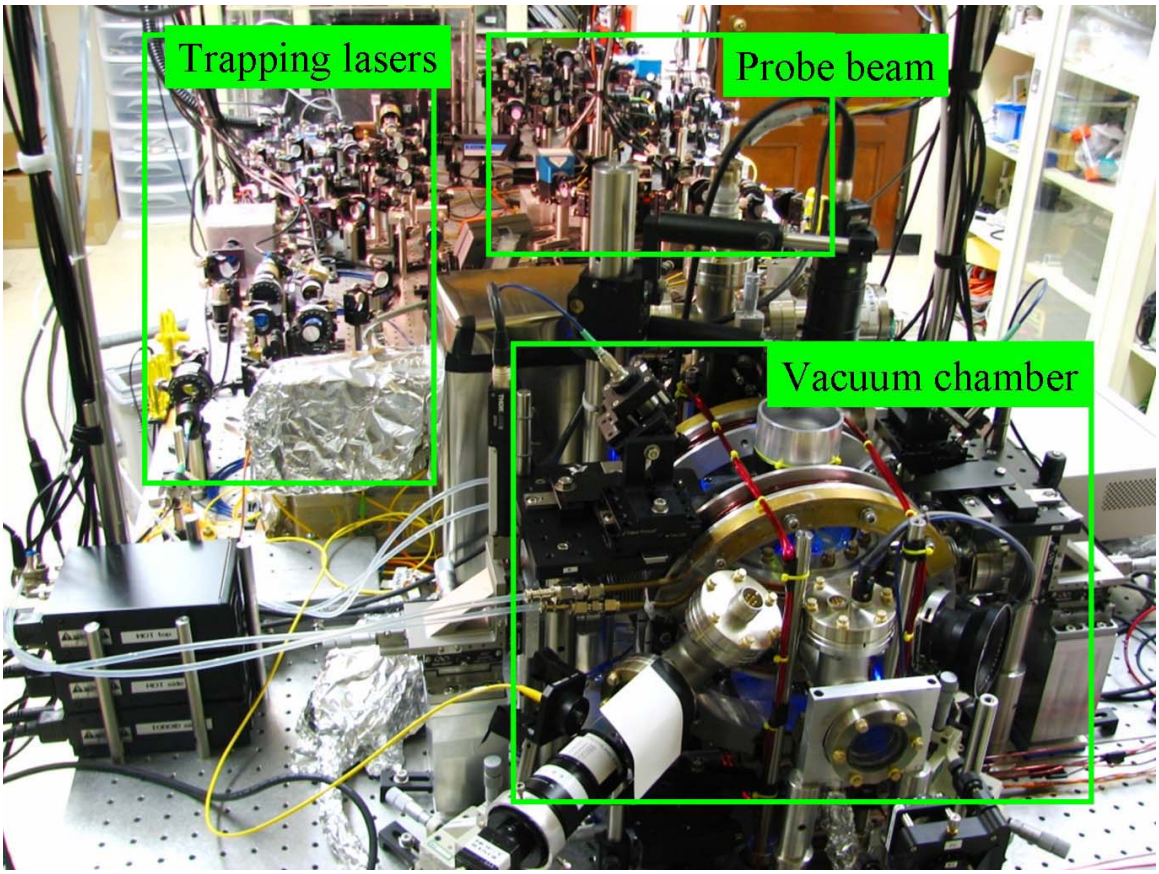

Figure 2.7: Photo of our experimental table. In the "Trapping Lasers" section, light from a high-power TiSaph laser is tuned in frequency and power in order to trap atoms in a MOT. A diode laser is used to "repump" the atoms into the correct state for trapping to occur. The "Probe Beam" configuration consists of a small tap of power from the TiSaph laser that is tuned in frequency and polarization to serve as a probe of the toroidal mode. Further, there is a separate diode laser that scans in frequency over the resonance, which provides the signal that allows us to tune the coupling between the taper and toroid, as well as the polarization of the probe laser. Finally, the vacuum chamber contains the majority of the experiment, as this is where the atoms and toroids are located.

2.3.1 Vacuum Chamber Design

Overview of physical design — One of my key roles during the first few years on this experiment was designing the vacuum chamber and the components that would be put inside. These components were modeled to scale using Solidworks, a three-dimensional modeling program, as represented in Figure 2.8. This allowed the experiment to be put together virtually before any parts were ever machined, enabling us to rectify many design flaws before the construction of the apparatus itself. Given the many constraints of the experiment, this modeling step proved invaluable. Additional drawings can be found in Appendix A and in the accompanying CD.

For example, we chose to use a stock chamber with eight small and two large viewports. But, in order to magnify a toroid enough to be able to image the coupling between it and the taper while maintaining a high enough resolution, the imaging system needed to be as close to the toroid as possible. Further, in order to make a MOT with the traditional six counter-propagating beam configuration, the chip needed to be in the center of the chamber (a mirror MOT configuration was considered, but this was rejected due to complications in other design factors such as toroid motion with attached mirrors and side beam paths). In order to minimize this distance, the chamber was placed on its side with the larger windows parallel to the optical table. However, this caused the magnetic coils necessary to create the MOT to be further away, larger, and to run higher current. Many scenarios were designed and virtually tested before one was decided upon in order to choose the least complicated that best met all requirements.

Coupling motion — Particularly challenging was maintaining structural integrity of the toroid positioning system while allowing the beams for atom trapping to pass unimpeded. In order to couple light into the optical mode of the toroidal cavity we use an optical fiber which has been tapered such that its diameter is less than one wavelength of light (see Chapter 3 for a more detailed discussion) [41]. Such a small diameter causes most of the light field to reside outside the physical structure as an evanescent wave. This evanescent wave couples into the mode of the toroid, the degree

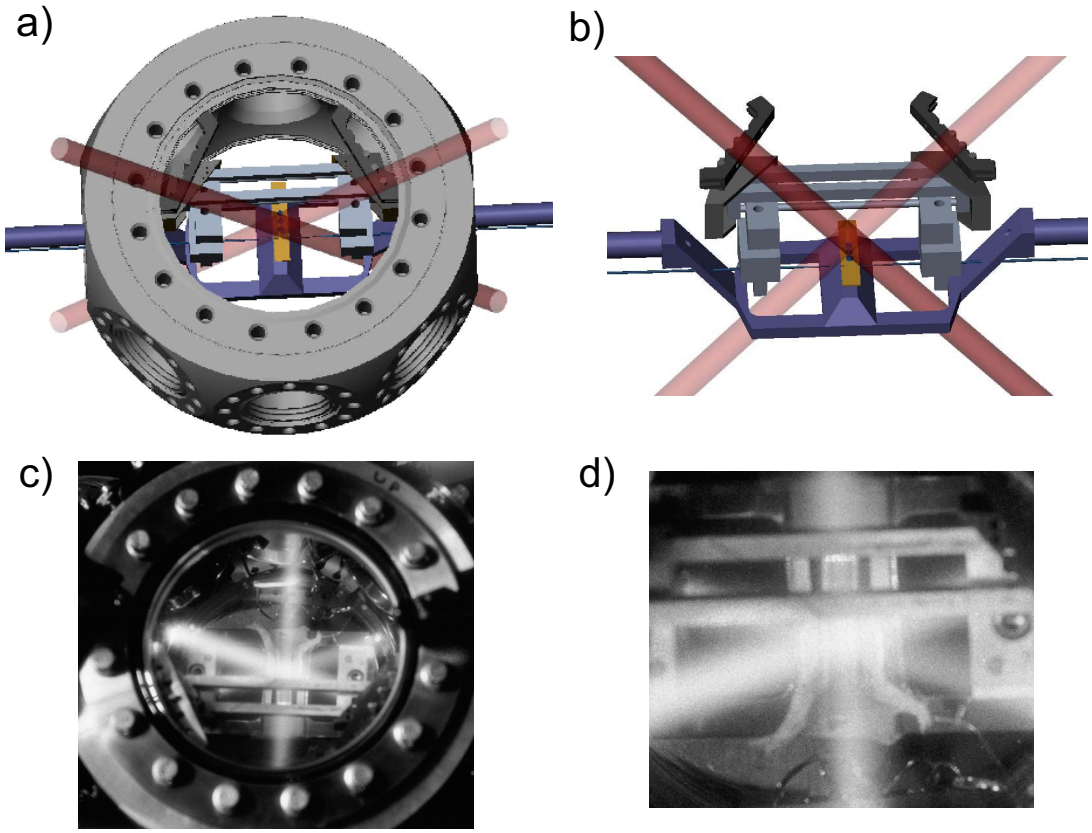

Figure 2.8: (a–b) Three-dimensional scale models, with the exception of the toroids, of our vacuum chamber and internal components; (c–d) Infrared photographs of the chamber from the same views shown in (a–b), with MOT beams visible by the excitation of background cesium atoms.

of which is determined by the relative positions of the two structures. This process of coupling light into the resonator will be discussed in depth later in Sections 2.5 and 5.1.2. In order to control this separation either the taper or the toroid must be able to move along the three spatial axes. To maintain a fixed imaging system while allowing the flexibility of choosing from among an array of toroids, we chose to move the toroid chip while leaving the taper stationary. As discussed previously, our goal was not to be able to tune the distance between the taper and toroid to fine precision in this version of the experiment, but rather to operate with the taper in contact with the toroid. Given this consideration, we are able to use a more economical and readily available method to control the motion of the toroid from outside the chamber, rather than requiring a sophisticated, vacuum-compatible positioning system capable

of moving over a centimeter with precision on the sub-micrometer scale; while now commercially available, at the time such systems were special order for ultrahigh vacuum applications.

The tapered fiber is mounted to a holder which is then fixed to the inside of the chamber using "groove grabbers," adaptors specially designed to attach components to the walls of our Kimball Physics vacuum chamber. Originally, our taper was held in the chamber by the same clamps which were also used to hold the fiber during the tapering process (this holder is shown in Figure 2.8). However, we learned that these rail mounted clamps did not give us the alignment precision necessary to consistently fabricate high quality tapers. We therefore changed our tapering system to use clamps which can be aligned independently and remain on the pulling system in order to minimize alignment errors between different pulls. The taper is then glued to a fork (Chapter 3) in order to put it in the vacuum chamber, saving precious space in the chamber as we no longer need to use bulky fiber clamps. For either method of holding the taper, it is important that the taper holder be attached to the chamber in a manner that lends itself to gentle installation, as the tapers break very easily. We chose to use a system in which the taper holder slides into small, fitted shelves positioned at either end of the taper holder, depicted in Figure 2.8b. A set screw is then pressed from each shelf onto the taper holder for added stability.

The toroid is mounted upon a stage which is controlled by a pair of three axis translation stages located outside the chamber, which connect to the stage by means of a flexible vacuum bellows (Figure 2.9). While this scheme is not stable enough to maintain the separation between the taper and toroid to within a micron, it does suffice to achieve the appropriate point of contact between the taper and the toroid. In designing the stage upon which the toroid is mounted (Figures 2.8b and 2.9b), the beams which will be used for the MOT must be taken into consideration. We need the toroid to be as close as possible to the atoms so that they acquire a minimum velocity from gravity before interacting with the toroid, thus extending the interaction time before they fall past. However, the stage must not clip or otherwise interfere with the beams. Therefore, in order to maintain the structural integrity of the stage while

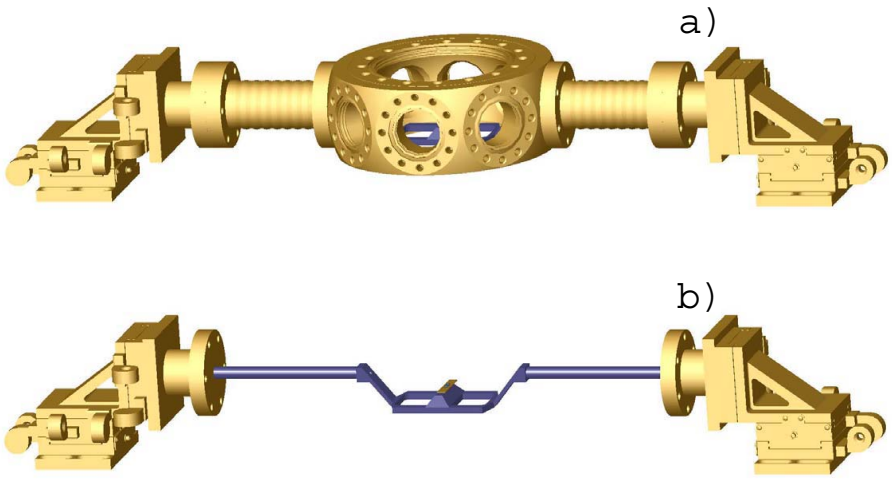

Figure 2.9: The motion of the toroid is controlled outside the chamber by two xyz translation stages that are coupled to rods inside of the chamber via flexible bellows. Each axis is controlled by a micrometer, with piezos on the tips of the micrometers that control the two fine motion axes. (a) Shown with the bellows and chamber; (b) shown without chamber and bellows in order to see the internal support system

allowing for the MOT beams, we incorporate a pseudopyramid-shaped platform for the toroid chip to sit upon, thus allowing the beams to pass unimpeded while avoiding a thin, weak center piece.

For additional information regarding these and other Solidworks files, see Appendix A.

Fiber into the vacuum chamber — As will be discussed in Section 2.5, efficient transfer of photons from the output of the toroid to our detectors is of the utmost importance. For this reason, among others, a tapered fiber is used to couple light into the mode of the toroidal resonator [41] as opposed to the historical prism coupling method [11]. In order to take full advantage of the efficiency from tapered fibers, it is necessary for the signal from the fiber to be efficiently transferred from the toroid to outside the vacuum chamber to our detectors. The most efficient way to do this is with one continuous fiber (more detailed discussion in Section 2.3.4). At the time of this experiment, commercially available systems were not able to send one continuous fiber

from atmospheric pressures into a vacuum chamber at our low pressures. Therefore, using the design outlined in reference [42], we machined a feedthrough that utilizes a standard Swagelok coupler welded into a vacuum blank with a teflon plug. This teflon plug has holes precisely drilled to the diameter of the fiber. The Swagelok is tightened in order to compress the teflon around the fiber, thus creating a seal which will hold vacuum down to 10^{-11} Torr. Important to note is that the teflon needs to be tightened whenever the chamber is heated; the holes in the teflon expand when heated and do not return to the same size when they are cooled, thus allowing a slow leak of air into the chamber and limiting the background pressure. This is usually remedied with a half turn tightening. Since a tightened Swagelok cannot be loosened without compromising the vacuum seal and there is a limited range that the bolt can be tightened, it is best to tighten modestly while observing the chamber pressure and only retighten when necessary.

Imaging — In order to couple the toroid to the taper, which is less than 1 μm in diameter, we require an imaging system with a minimum resolution on order of 1 μm. Our system, designed by Barak Dayan and Tal Carmon, consists of a camera lens mounted above the vacuum chamber window and a focusing lens approximately 1–2 meters away in order to obtain a large enough magnification. The image is then focused onto a CCD camera and is displayed on a monitor. The resolution of the image was optimal when illuminated with a blue LED due to the wavelength being on the short end of the visible spectrum. Two such systems are used, one from the top and one from the side. In order to image the MOT, the lens above the vacuum chamber is removed and a IR sensitive lens/camera system with a focal length aligned to the MOT location and an appropriate magnification is put in place.

2.3.2 MOT

The interaction distance from the surface of a 30 μm toroid is approximately 500 nm, for a modal height of approximately one micron, giving an area over which atoms can interact with our toroids on order of 10^{-2} μm^2. In order to maximize the chances

of an atom interacting with our toroid we must make the atom cloud as dense as possible in the vicinity of the resonator. To do so we use standard atom trapping techniques to trap, cool, and drop the atoms over our chosen toroid. First, we trap the atoms in a standard magneto-optical trap [43] at the crossing of three pairs of counterpropagating, red-detuned lasers; this crossing is aligned to be at the zero of a magnetic field created by two current-carrying coils set up in an anti-Helmholtz configuration. We then cool the atoms to a temperature of approximately 10 μK using polarization gradient cooling (PGC) [44], [45]. We measure the temperature of our atom cloud by turning off the trap and taking fluorescence images of the atoms at different time delays. From these images we can determine how fast the cloud is expanding and translate this into a temperature by the relation $\frac{3}{2}k_BT = \frac{1}{2}mv^2$.

Alignment — After PGC, we have a few million atoms in a spherical trap that measures a couple of millimeters in diameter. Comparing the surface area to the interaction area of the toroid, we expect a few out of every million atoms to interact with the toroid. With so few atoms passing through the resonator mode, we need to maximize the interaction time of each one by minimizing the atom velocity at the height of the toroid. For any drop longer than tens of microns, the velocity acquired by gravity, $v_{gravity} = \sqrt{2gh}$, is dominate over the velocity associated with the finite temperature of the atoms, $v_{thermal} = \sqrt{\frac{3k_BT}{m_{Cs}}}$. For a drop of 1 cm, as is comparable to our system, the difference in velocity, and hence time, between gravitational and thermal velocity is one order of magnitude; hence, the need to minimize the height of the atom cloud drop relative to the toroid chip. While a shorter distance is desired, in order to obtain a MOT closer to the toroid than a few millimeters a different trapping configuration is necessary, such as a mirror MOT [46]. As the goal of this iteration was to design an experiment as simply as possible, we will leave more exotic MOT configurations to future generations of this experiment.

Equally important to the density of the atom cloud is ensuring that the atoms will hit the chosen toroid when the trap is turned off. To do this, we visually align the MOT directly above the toroid using our imaging system. Any stray magnetic

and light fields need to be eliminated as they will cause the trajectory of the atoms to differ from that caused by gravity; additionally, they will cause the atom cloud to deform and expand as it falls, lowering the density and hence the probability of an atom-toroid interaction. To remedy this, we lower the beam power in the MOT until the atoms are just visible. We then adjust the magnetic fields in order to maximize the number of atoms. The atoms are then released and their density is measured at various times; we again adjust the magnetic fields to maximize the number of atoms and ensure that they are indeed falling straight down, continuing this process until the proper behavior is achieved. Imbalances in beam power and polarization misalignments can also cause the MOT to receive a "kick" when the trap is turned off and must likewise be corrected.

Cesium source — Historically in our group, ampules of cesium have been used as the source of atoms in our vacuum chambers. Ampules are glass containers holding solid cesium which are broken under vacuum in a separate chamber which can be isolated from the rest of the experiment by a valve. At the time we were building our chamber, however, we made the decision to switch from ampules to getters as cesium dispensers. Getters are compact reservoirs of particular materials, in our case cesium, from which the material is released in a thermal spray when a current above threshold is applied across the reservoir. Getters have many advantages over ampules. First, getters are turned on and off electronically, whereas cesium from ampules is controlled by opening and closing a valve intermittently throughout the experiment. The cesium from a getter is quickly pumped away once the getters are turned off, whereas that from the ampules lingers. Getters release a smaller amount of cesium than ampules, which coat the chamber quicker, thereby providing a higher background pressure of cesium relative to other matter. While more cesium atoms in the chamber is clearly an advantage to building a large MOT, cesium is corrosive and has been known to damage valves, wires, mirror coatings, etc. Therefore, a vacuum chamber ideally will contain the minimum amount of cesium required to build a MOT of ample size. Lastly, getters are relatively easy to install, as they are compact and only require a

connection to current, while a glass ampule must be broken under vacuum.

After having used getters for the last several years, we have found a number of disadvantages over their ampule counterparts. Getters emit cesium at high temperatures $T_{getter} \sim 1000$ K, giving high thermal velocities $v_{getter} \simeq 250$ m/s compared to the room-temperature atoms from an ampule, $v_{ampule} \simeq 140$ m/s. Since the number of atoms trapped in a MOT is proportional to $(\frac{1}{v_{thermal}})^4$ [47], the loading is ten times more efficient for atoms from an ampule as opposed to a getter. Therefore, in order to decrease the temperature of the atoms, we are required to wait until a monolayer of cesium has built up upon the inside surface of the chamber, which can take several days of running the getters; at this point the cesium atoms are able to bounce off the walls, losing some amount of energy until they are cold enough the be caught in our MOT. Ampules, on the other hand, contain solid cesium which is slowly emitted at v_{ampule} and more easily captured. Getters can also run out of cesium with little or no warning, requiring the chamber to be opened in order to install a replacement, setting the experiment back by the length of time it takes the chamber to pump down (generally a week or two). More important, each time the chamber is opened the toroid and taper are at risk of being damaged. As such, it is common practice in our group to install many getters, from different batches, every time the chamber is opened in order to decrease our chances of ending up with only faulty or short-lived getters. Cesium from an ampule has been known to last for over a decade in one experiment, albeit the chamber has not been opened in this period of time.

In an attempt to increase the size of our atom cloud we aimed our getters directly at the trapping region, which is located directly above our toroids. However, immediately after this realignment we observed that the resonance linewidths increased by over an order of magnitude directly after turning on getters. Similarly, the efficiencies of tapers have degraded simultaneously with the turning on of getters. Previously, our getters were located near the bottom of the chamber, aimed upwards, ensuring that the toroidal surfaces were not directly in the atomic beam path. Therefore, these adverse effects may be due to the increased flux of cesium at the surface of the toroid.

A simple calculation comparing the flux of cesium due to the newly positioned

getters to that from the dropping of atoms trapped in the MOT shows that this is indeed plausible. The getters emit 10 μg/min of cesium [48], which corresponds to 10^{15} atoms per second. Assuming that the getters emit evenly across the hemisphere, when a 30 μm diameter toroid is located 10 cm away from the getters the resonator surface occupies a fractional area of 10^{-8}. This leads to a flux of $\sim 10^7$ atoms per second. However, a MOT with a diameter of 3 mm containing one million atoms produces a flux of only 100 atoms per drop. Since the MOT is dropped about once per second, this is an increase in atoms bombarding the toroid of $\sim 10^5$ atoms per second.

The coating of atoms on the surface alone may increase scattering and thus linewidth. However, if the cesium interacts with water vapor that may be on the resonator surface, then cesium hydroxide, CsOH, can be formed. CsOH is the strongest known base and is corrosive to glass [49], therefore likely to adversely effect the surface of our resonator. Yet another explanation may be that there are impurities emitted during the baking of the getters that are now more likely to hit the toroid surface do to the repositioning.

A separate problem that resulted from realigning the getters was due to the heat created by the getters. The threshold current required to emit cesium from the toroids is approximately four Amps; since the resistance of a getter is on order of one Ohm, this gives a power consumption of about 16 W, thereby generating a large amount of heat. The getters radiantly increase the temperature of everything in the chamber, including the toroids. This additional heating makes temperature tuning of resonances to lower temperatures (higher frequencies) even more difficult, as will be addressed in Section 2.3.3.

Fiber MOT — A significant change made in this MOT over previous implementations of our group is the use of fibers to transport our MOT beams to the vacuum chamber. The motivation behind the change was primarily due to space constraints in our experiment, but after implementation other advantages soon emerged. The traditional way of building a MOT is with three pairs of counter-propagating trapping

beams, collinear with a repumping beam that ensure the atoms stay in the appropriate energy level. The trapping beams are made by dividing one high-power beam into six beams of equal power using wave plates and polarizing beam splitters. The repumping beams are aligned into the path of the trapping beams at some point in the splitting. Each of these beams are then guided with mirrors to enter the chamber at the appropriate angle. While simple in principle, this process requires many optical components, many of which must be attached or mounted near to the chamber. Not only does this take up valuable space and optical access for apparatuses such as imaging and magnetic coils, the proximity of these mirrors lends themselves to inadvertent misalignment. Tracking down and correcting these misalignments is time consuming and often tedious. Therefore we changed our system to use a polarization-maintaining fiber beam splitter that takes two beams and combines them into six with powers equal to within $\sim 2\%$ of one another. While this fiber beam splitter is not as precise as a free-space design, the benefit of stability outweighs this lack of precision in power balance.

The trapping beam is plugged into one input of the splitter, the repumper into the other. The fibers are then connected to free-space fiber couplers which are mounted into rotatable mirror mounts for precision alignment. The fiber couplers are commercially aligned to expand the beam to a diameter of 1 cm. The rotation of the mirror mount allows us to adjust the linear polarization of the outgoing light by rotating the polarization-maintaining fiber (through which light propagates with a linear polarization). This linear light then passes through a rotatable quarter waveplate, also mounted to the mirror mount, in order to obtain the proper circular polarization. This mirror mount apparatus is the only object needing directional alignment for each MOT beam, greatly simplifying the alignment and inevitable debugging processes.

2.3.3 Tuning of Resonance Frequencies

For a cesium atom to interact with our resonator in the particular detection scheme we have chosen, the frequency of the toroid resonance must be very close to that of the atomic transition we are probing, namely the $6S_{1/2}, F = 4 \longrightarrow 6P_{3/2}, F' = 5'$ transition of cesium. We tune the frequency of the resonances using temperature [18]. A change in temperature affects both the physical size of the resonator, due to thermal expansion, as well as the index of refraction of the silica structure. Both of these phenomena work together such that an increase in temperature leads to a negative frequency shift and vice versa. We have observed a frequency shift of approximately -2.5 GHz for every degree Celsius of temperature change. To accomplish this change in temperature, we use a ceramic vacuum-compatible peltier; we have had good experience with the Melcor Aluminum Nitride ET1.9-35-F1N-H1-C1. This peltier has allowed us to tune, through heating, approximately 30 GHz under vacuum.

While both heating and cooling are possible over a much larger range than 30 GHz in atmospheric pressures, vacuum limits tuning abilities due to difficulties in removing heat from the system. In vacuum there is no convection. This not only limits cooling from the peltier itself, it also diminishes thermal contact between pieces which are screwed together since the only method of heat transfer is through points of contact and radiation. To improve thermal conductivity between components we used a vacuum-compatible grease in joints; specifically, we use Apiezon L Grease due to its low vapor pressure over the relevant temperature range. However, remaining limitations in heat removal have caused overheating of the peltier when too much current is applied. Therefore, we limit ourselves to 100 mA of current, which corresponds to about 30 GHz in frequency shift.

Our tuning range is further limited by our inability to maintain a frequency shift which corresponds to a cooler temperature. First, a peltier is able to cool an object by maintaining a temperature differential between each of its sides. If the hot side is not able to effectively dispose of any generated heat (e.g., resistive heating), then its temperature will rise. Thus, even though the cold side of the peltier is a set number

of degrees cooler than the hot side, the entire device is warmer. A larger temperature differential, thus more current, is now needed to maintain the same temperature for the cold side. This additional current produces more heat, requiring more current to maintain the same temperature, continuing until we have exhausted the range of the peltier. The second reason cooling is not a viable option for our toroids is that they become a "cold finger" in our vacuum chamber. The coldest object in a vacuum chamber, a "cold finger", causes background material to condense on it. This material is not only potentially damaging to the ultra-pure surface that gives these toroids high quality factors, it also makes the resonators slightly larger. One atomic layer can be enough to shift a resonance a few nanometers in the direction that mimics heating — detrimental when trying to cool.

Therefore, we are limited to choosing resonances that are cooler than our desired cesium transition. Taking into account other heat sources in the experiment such as radiating getters and MOT beams clipping the toroid chip (which is minimized but often unavoidable in the current geometry), we must allow a heat buffer of about 10 GHz. By this we mean that the resonance needs to be heated by at least this much in order to reach our desired frequency; as the other heating sources continue to heat the chip, we decrease the amount of current in the peltier, thus maintaining a constant temperature. With a buffer of this size we are able to run our experiment for several hours before the peltier needs to cool rather than heat in order to maintain the desired resonance frequency.

2.3.4 Optical Components

Toroid probe — In order to detect whether an atom has interacted with the mode of the toroid we must probe the mode of the toroid with an extremely low power laser to look for a change in the toroidal resonance spectrum. This laser is locked to the appropriate cesium transition using an error signal derived from a cesium cell in conjunction with standard Pound-Drever-Hall locking techniques [50, 51]. Once the toroid resonance is tuned to the same frequency as the probe, the overlap between the

taper and toroid modes is adjusted until the condition of critical coupling is met, at which point the transmission out of the toroid ideally drops to zero (see Section 2.5). At this point, with nearly no photons exiting the toroid, we have the optimal signal-to-noise ratio for our signal. When an atom approaches the surface of the toroid the resonance of the cavity splits, destroying the critical coupling condition, and hence changing the output of the toroid from nearly zero to nonzero, as demonstrated in Figure 2.1. The height of this nonzero transmission is a function of coupling strength, the toroidal modal profile as addressed in reference [19], and the detuning of the cavity from the atom. We exploit this last criteria, as explained in Section 2.2, in order to determine g_0. To achieve this detuning, the beam is double passed through an acousto-optic modulator, AOM, in order to shift the frequency of the beam from the atomic transition to which it is locked. Prior to being coupled into the tapered fiber, the light passes through a half-wave-plate/quarter-wave-plate configuration which, assuming linear incoming light, allows us to acquire any polarization necessary for coupling to the toroidal mode.

The laser power must be attenuated to the point where less than one photon is in the cavity at any given time, i.e., the intracavity photon number n_0 is less than one. This is to ensure that no more than one photon is interacting with any given atom. An atom is considered "saturated" when one photon has been absorbed by it, causing it to be excited; the atom cannot absorb more than one photon of this energy due to the energy level spacing, causing any additional photons to be blind to the presence of the atom. In this experiment, our intracavity photon number was $\simeq 0.3$. For this particular cavity, with a linewidth of 18 MHz, we found this to be the optimal experimental value. Once the intracavity photon number approaches 1, the atom is clearly saturated. Despite the fact that lower intracavity photon numbers are theoretically better in terms of contrast, for our experiment, input powers which yield less than 0.3 photons in the cavity led to too few photons counted per atom transit, hence our signal was lost in noise. Additionally, a higher-efficiency taper would allow the power, hence intracavity photon number, to be decreased by a percentage equal to the increase in efficiency. In this iteration of the experiment the taper had a total

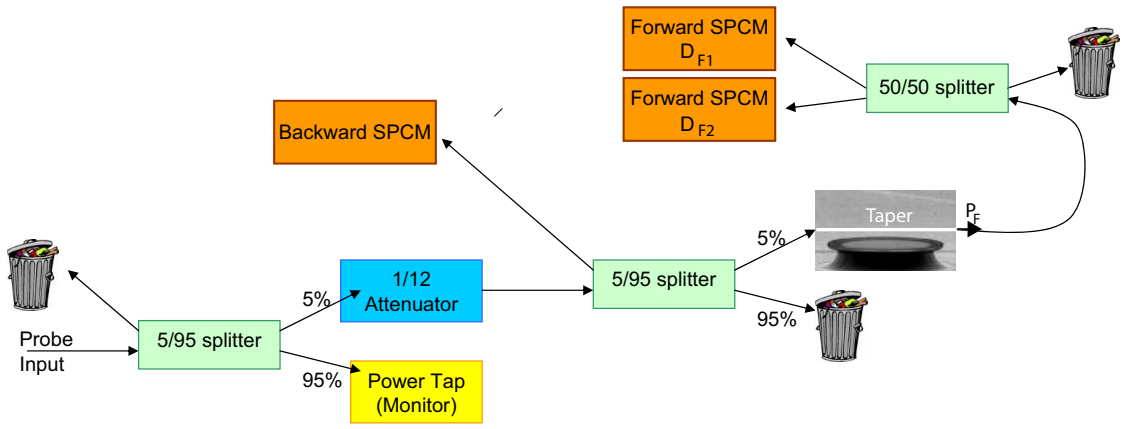

Figure 2.10: Schematic of fiber components used in our experiment. Once the probe is coupled into the fiber, the light is split by a 5/95 ratio fiber beam splitter. The larger of the two outputs functions as a power tap that allows us to monitor and calibrate the power that enters the tapered fiber. The smaller output is attenuated by 1/12 before entering another 5/95 fiber beam splitter with the 5% output entering the tapered fiber, giving a total ratio of 1/4500 between the probe beam and the power tap. This large attenuation is necessary in order to avoid saturating the atom. The second 5/95 beam splitter is used to monitor the light which is scattered into the counter-propagating mode of the toroid. At the output of the taper, the signal P_F enters a 50/50 beam splitter and both outputs are detected on single photon counting modules D_{F1} and D_{F2}. Two detectors are used in order to look for coincidences in the signal, helpful in detecting small signals and, ultimately, to probe photon statistics.

efficiency of only 4%, allowing room for improvement.

In order to calibrate such low power levels of light going into our taper, we have installed a power tap, shown in Figure 2.10. After the free-space optics have set the frequency and polarization of the probe light, it is coupled into the fiber network shown in Figure 2.10. The light passes through a fiber optic beam splitter that divides the input into two outputs with a ratio of 1:19, or 5% and 95%. The optical power is measured at the 95% output while the other light output passes through a 1/12 attenuator and another 5/95% beam splitter before entering into the taper/toroid. Therefore the power at the power tap is $\simeq 4500$ times larger than that which enters the taper, bringing it to a level easily measured by a standard power meter.

Detection — As will be discussed in Section 2.4, we measure the output of the taper, P_F in Figure 2.2a, on two detectors (D_{F1}, D_{F2}). In the data shown in Figures

2.4 and 2.6, P_F is directed to a fiber beam splitter whose outputs are detected by a pair of single photon counting modules (SPCMs) (D_{F1}, D_{F2}) each with overall quantum efficiency $\alpha \simeq 0.5$ and dark counts < 100 per second. Using two detectors enables us to avoid, or at least assess, phenomena that are related to the non-ideality of these detectors, such as their ~ 50 ns dead time, saturation at fluxes of few million counts per second and above, the "after-pulsing" effect which results in a small probability for a false second count following the detection of a single photon, etc. Thus, two detectors allow the detection of photons that are separated temporally by less than the dead time of these detectors (which are not number-resolving), and increases the maximal flux of photons that can be detected by our system before saturation effects take place. This method also enables further analysis of the photon statistics of the light. With two detectors we can perform cross-correlation between the two series of photon counts, as presented in Figure 2.4c. A single detector was used to monitor the backwards flux, namely light that was coupled into the cavity, scattered into the counter-propagating mode, and then transmitted backwards into the taper. When atom transits occurred, the observed increase in the forward flux was accompanied by a decrease in this backward flux.

In order to maximize efficiency, the signal P_F is split into two equal branches by a 50/50 fiber beam splitter which then plugs directly into the detectors. Maintaining the signal in fiber eliminates unnecessary losses that accrue when light is taken in and out of fiber. Additionally, this allows us to use a more compact system than one which uses free-space optics. Given that we are counting single photons, any background photons from sources such as room light and computer monitors are an additional source of noise; fiber networks are much easier to keep dark, as the fiber jacketing itself is a natural light shield and there are no mirrors to be bumped. However, we do observe that the noise floor diminishes significantly when the fiber network and detector are wrapped in aluminum foil and/or placed in a dark box.

In designing the detection scheme, consideration was given whether to use SPCMs or heterodyne detectors. Originally we chose to use heterodyne detection, but soon realized that this was problematic since the polarization of the probe beam must be

aligned to that of the local oscillator. A polarization misalignment between the probe and the local oscillator is evident in a nonzero value on resonance when critically-coupled. However, this nonzero value is exactly the signal that is used to align the polarization of the probe to the toroidal mode as well as the position of the taper relative to the toroid. In order to be critically-coupled to a resonance, the polarization must be aligned to the toroid mode with great precision or else a nonzero value of transmission on resonance will occur. Each time the taper couples to the resonance, the necessary polarization changes depending on the point of contact between the taper and toroid, as well modal shape. Clearly the same error signal for three degrees of freedom makes alignment exceedingly difficult. SPCMs, on the other hand, do not have a local oscillator and thus simplify alignment greatly.

Labview control — The timing of our experiment is controlled by a Labview program, written primarily by Barak Dayan. It controls the loading, polarization gradient cooling, and eventual dropping of the MOT by switching detunings and optical paths with AOMs. The probe is switched, corresponding to the timing of the MOT drop, from the low power necessary to not saturate an atom, to a higher power in between experiment cycles which allows us to monitor and adjust the degree of critical coupling with higher accuracy. Finally, a counter card is triggered to count photon clicks from each SPCM over a specified time interval.

2.4 Experimental Details

2.4.1 Preparation and Characterization of Cold Atoms

Each measurement cycle in our experiment takes about 2.5 sec, and includes approximately 2 seconds for loading a magneto-optical trap (MOT), followed by 20 ms of polarization-gradient cooling of the atoms (with the magnetic fields for the MOT turned off). The trapping and cooling beams are then switched off and the atoms fall on the microtoroid.

For each run, we measure the number and arrival times of atoms in the falling atom cloud 2 mm above the microtoroid with a laser beam resonant with the $6S_{1/2}, F = 4 \longrightarrow 6P_{3/2}, F' = 4'$ transition [52]. In each cycle we observe approximately 30 atom transits during the center 10 ms of our data-collection time window. This value is in a reasonable agreement with the theoretically calculated rate of 20 transits, which was derived by comparing the measured density of the falling atom cloud to the numerically calculated interaction area of the evanescent field. Every cycle with cold atoms is followed by an identical cycle with no trapped atoms for which the magnetic field for the MOT is turned off during the loading period. We have also carried out other tests for the "no atoms" case, including switching off the repumping light for the MOT (with all other parameters unchanged).

2.4.2 Excitation and Detection System

The frequency ω_p of the probe beam P_{in} in Figure 2.2a is actively stabilized to a fixed detuning from the atomic resonance $\Delta_{Ap} = \omega_A - \omega_p$ via saturation spectroscopy to within $\pm$100 kHz. The cavity resonance at ω_C is monitored relative to ω_A and ω_p for each drop of the atom cloud and each reference cycle, and is controlled by temperature tuning a thermoelectric device upon which the silicon chip is mounted, with a frequency shift of approximately 3 MHz per mK of temperature change. Data were being automatically recorded whenever the condition of critical coupling (i.e., $P_F < 1\%$ of the maximal value of 30 counts per 2 μs) was achieved, correponding to $\omega_p = \omega_C$ to within $\pm$ 2 MHz. Note that in our experiment we used blue detuning of the cavity and the probe relative to the atom, since red detuning could have lead to a resonant interaction with the $6S_{1/2}$ F=4 $\rightarrow$ $6P_{3/2}$ F$' = 4'$ transition at large Δ_{AC}. Additionally, blue detuning leads to an underestimation of g, as the dipole forces become increasingly repulsive as we blue-detune our cavity, possibly leading to a more rapid reduction in the probability of transits. However, our calculations indicate that in our current experimental settings the light forces are significantly smaller than the van der Waals forces over the entire relevant interaction region of the

atom with the evanescent field, and their effect on the atom's motion and temperature are small. This situation is mostly due to the small populations of the dressed states that are coupled to the atom for excitation with $\omega_p \approx \omega_C$. More specifically, in our experiment the probe field frequency is always tuned to the empty cavity resonance, between the two vacuum-Rabi sidebands which correspond to the two dressed states of the atom and the coupled cavity mode. Thus, as the energy splitting between these states (and hence the associated dipole potential) grows during the atom transit, their population drops dramatically (and so does their contribution to the mechanical potential experienced by the atom) as they decouple from the probe field (leading to the described increase in the forward flux T_F). The resulting forces are of the order of few MHz/μm, leading to estimated displacements of up to 40 nm during the 2 μs of atom transit for intermediate values of Δ_{AC}. Further measurements to explore the effect of light forces, along with its inclusion in the theoretical model, are in progress.

The forward propagating signal P_F is directed to a fiber beam splitter whose outputs are detected by a pair of SPCMs (D_{F1}, D_{F2}). These detection events are time-stamped relative to the drop time of the atom cloud, and stored for later analysis. The data in the figures refers to the total counts from the combined outputs of (D_{F1}, D_{F2}). The overall propagation efficiency ξ from the fiber taper at the position of the toroidal resonator to the input beam splitter for (D_{F1}, D_{F2}) is $\xi = 0.70 \pm 0.02$.

In the absence of an atom, the average intracavity photon number is $\bar{n}_0 \simeq 0.3$ for mode a for critical coupling with $\omega_p = \omega_C$. If the probe is then detuned such that $|\omega_p - \omega_C| \gg \kappa$, the average number of counts recorded in a 2 μs interval is $C_{\Delta \gg \kappa} \approx 30$, which provides a calibration of the flux P_F given the known propagation and detection losses.

2.4.3 Calculation of the Coherent Coupling Parameter g_0

For our particular toroidal resonator with major diameter $D \simeq 44$ μm and minor diameter $d \simeq 6$ μm, we find $\phi^{\pm}_{\rm tw}(\rho, \theta, x)$ numerically [12] for the lowest order traveling-wave modes of the resonator, from which follows the coupling parameters $g_0^{\rm tw}$ and g_0.

For the $6S_{1/2}, F = 4, m_F = 4 \longrightarrow 6P_{3/2}, F' = 5', m'_F = 5'$ transition of the D_2 line of atomic cesium, we find $g_0^{\text{tw}}/2\pi = 80$ MHz and so $g_0/2\pi = \sqrt{2} \times 80$ MHz. However, a circularly polarized field is required for coupling to this transition while the toroidal resonator supports linear polarization. Hence, for atoms uniformly distributed over the set of Zeeman states $\{m_F\}$ in the $F = 4$ ground state, we calculate g_0 from an average over Clebsch-Gordon coefficients for $\Delta m_F = 0$ transitions for $6S_{1/2}, F = 4 \longleftrightarrow 6P_{3/2}, F' = 5'$, leading to $g_0/2\pi = 70$ MHz, which is the value utilized above.

2.5 Critical Coupling

The signal caused when an atom passes by the toroid and destroys the resonance condition is exceedingly small and difficult to detect. When the toroid is not present, about thirty photons pass through the taper in a two microsecond window. Due to the modal coupling described in reference [19] less than half of these photons are actually transmitted, approximately ten photons over about two microseconds for an optimally coupled atom. However, most atoms only emit a few photons as they pass due to being finite distances from the resonator. A very dark background signal is crucial in order to detect these few photons, which can easily be lost in experimental noise. Our method of obtaining this dark background is to operate in the regime of critical coupling. As the distance x between the taper and toroid, shown in Figure 2.11, is decreased, the rate of coupling between these two waveguides increases. The amount of coupling is classified into three regimes: under-coupled, critically-coupled, and over-coupled. In under-coupling and over-coupling the rate at which the taper is coupling light into the toroid is respectively less than or greater than the total internal loss rates of the cavity; critical coupling is achieved when this coupling rate exactly matches that of toroidal losses. At critical coupling, light which is directly transmitted past the toroid, and is hence never coupled in, exactly destructively interferes with the light that couples back into the taper from the toroid. This causes the light output of the taper, P_F shown in Figure 2.11a, to be near zero on resonance [18].

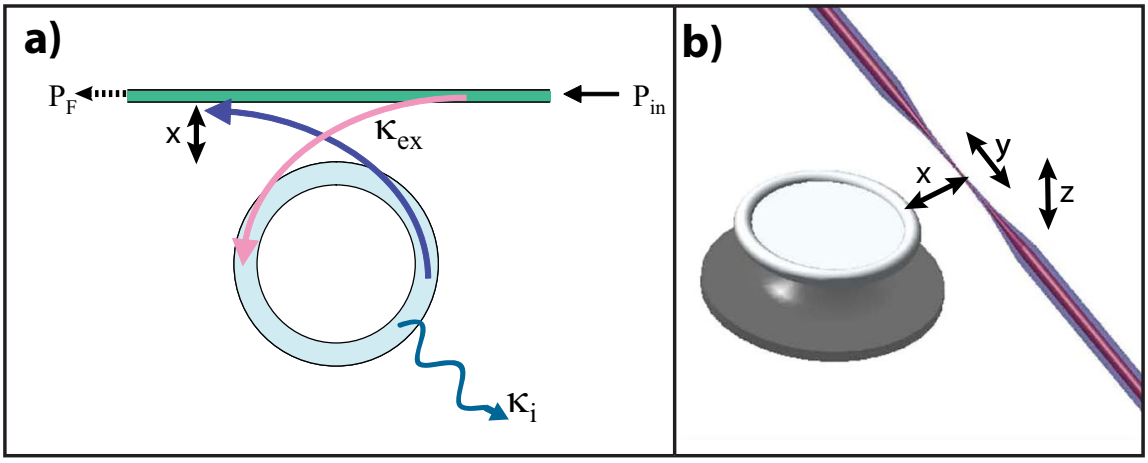

Figure 2.11: (a) Schematic of the taper coupling to a mode of the toroid. The power into the taper, P_{in}, is coupled into the toroid at a rate κ_{ex}. The light then circulates in the cavity, which has an internal loss rate given by κ_i, and is finally coupled back into the taper, again at a rate of κ_{ex}, to produce and outgoing power of P_F. (b) This cartoon defines x, the taper toroid distance, which is aligned in order to critically couple to the toroidal mode. The taper thickness is changed in order to mode match to the toroid by scanning along the length of the fiber, y. The height of the taper relative to the toroid is denoted by z.

2.5.1 Contact Mode

In order to obtain this near-perfect destructive interference at the output of the toroid, not only must the overlap between the optical modes be tuned, but the matching between the taper and toroid modes, as well as their respective polarizations, must be precisely aligned. Experimentally this is done by concurrently tuning the separation between the taper and toroid "x," the incoming light polarization, and the diameter of the taper at the point of coupling until a minimum transmission on resonance is obtained. The probe laser frequency is swept over a range large enough to encompass the resonance; the output of the taper, P_F, is connected to a pair of SPCMs which are monitored by a counting card in a computer. The percent of power extinction on resonance is then calculated and compared with the power levels off resonance; our experiment is operated with extinction levels of over 99%.

As discussed in Section 2.1, due to limitations in the accuracy and stability of this positioning system we have chosen to operate with the taper in contact with

the toroid, referred to hereinafter as "contact mode." Ideally, the separation between the taper and toroid is finely tuned to the desired level of coupling; this technique, referred to as "non-contact mode," is discussed in Chapter 5. Additionally, in the time since the inception of this initial experiment, this separation is now controlled and locked, as discussed in Chapter 6.

Obtaining critical coupling with P_F dark enough to observe atom transits by means of contact mode is significantly more difficult and potentially damaging to the toroid than non-contact mode and should therefore only be used when an appropriate positioning system is unavailable. Rather than arbitrarily choosing the separation between taper and toroid, we are only able to choose the point at which we attach the taper to the toroid. Each time the toroid is contacted with the taper we are potentially damaging the fine surface that is responsible for high quality factors. To simplify the process of finding resonance locations, as well as to minimize damage from contacting the taper, toroids should be characterized in a setup external to the vacuum chamber that is capable of operating in non-contact mode. This is more feasible without the constraints of a vacuum chamber and optics. Additionally, these parts are all commercially available and can be obtained rather reasonably compared to a system which is vacuum-compatible. For this experiment, the toroid chip was mounted to a stage attached to an xyz translation stage. Piezo-tipped micrometers were used to control the fine and coarse motion; the taper was rigidly mounted. A pair microscopes were used to image the toroid from above and from the side. A model of the system we used is shown in Figure 2.12 and the process of characterizing toroids is described in Chapter 4.

Once the desired resonance has been located, the chip is transferred into the vacuum chamber and contact mode coupling can begin. When the toroid is brought near the surface of the taper it is likely that they will be drawn together due to the van der Waals force. Hence, if contact mode is not desired, it is beneficial to use a thinner taper further from the surface of the toroid; the thinner the taper the larger its evanescent field, thus the larger the separation between it and the toroid. However, since we need to operate in contact mode, a thicker taper is necessary to produce the

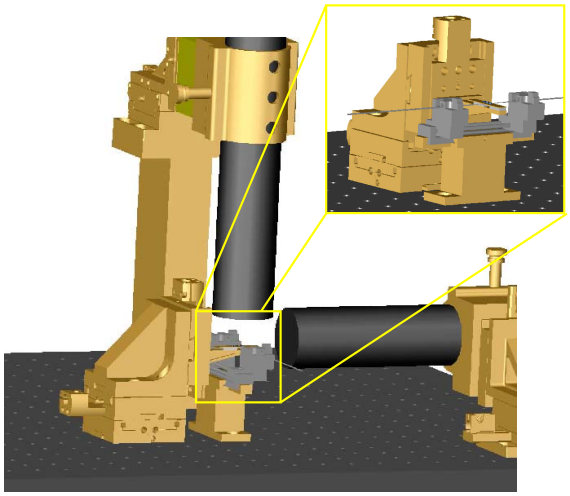

Figure 2.12: Model of our original, simple, external coupling setup. The toroid chip is fixed to a platform which is attached to a three-dimensional translation stage, shown in the inset. The stage is controlled by a piezo-tipped micrometer for each axis (not shown). The taper is held by clamps on either side on a fixed platform. Microscopes image the toroid from above as well as from the side.

correct amount of mode overlap for critical coupling. In order to obtain proper mode overlap and matching, proper choice of diameter of the taper and point of contact are critical. An arbitrary thickness is chosen at the beginning of the coupling procedure, to be fine tuned in an iterative process. Once the taper is contacted, the resonance is observed by monitoring the output of the taper with the probe laser scanning over the width of the Lorentzian. The toroid is then moved a large enough amount to drag the taper across its surface, thereby changing the amount of coupling. In order to compensate for the fact that the taper is in contact with the toroid, the taper needs to be placed either on top or beneath the toroid surface to allow enough separation between the modes while still being attached. It can be determined whether the toroid is over or under-coupled by observing how the resonance behaves as the taper is moved further from the edge of the toroid (i.e., away from the strongest mode field). Since moving the taper up the toroid is effectively increasing the distance between the modes, if the resonance gets deeper then it is moving from over-coupled towards critically-coupled. This means that the taper is too thin. If the taper is too thick,

then the resonance will get shallower as it is under-coupled, moving toward being even more under-coupled. The toroid should then be detached and moved along the taper in the appropriate direction in order to adjust the thickness. This process should be repeated until all three coupling regimes (under, critical, and over-coupled) are reachable by dragging the fiber along the toroid surface.

Once the proper taper thickness has been achieved, the taper position and light polarization are optimized for the deepest resonance, and hence darkest P_F on resonance, possible. Unfortunately, the taper does not slide smoothly on the toroidal surface but rather moves in a stick and slip motion. Therefore, care and patience must be taken in choosing the initial contact point between these two surfaces. The position can be fine tuned once contact can be made, but only over a very small range before the slip part of the motion occurs, moving the taper by more than intended. Once the best location has been chosen, the polarization of the probe light must be aligned to match that of the toroid mode. Using the free-space wave plates in the probe beam, walk the polarization until the minimum of the resonance is as dark as possible. Repeat the positioning of the taper and adjusting of the polarization until P_F reaches the desired level of darkness.

After many occasions of coupling the toroid at the same location with the same portion of taper, defects can occur that act as additional scatterers, hence broadening the resonance. This can often be remedied by either coupling the toroid from beneath, (or above if it was initially coupled to from beneath), or from the other side. This exposes the toroid to a new portion of the taper surface, thus causing the resonance to narrow.

2.6 Interesting Observations and Tricks

2.6.1 Taper Power Limitations

Fiber fuse — It has been observed that the power threshold for tapered fibers diminishes by many orders of magnitude once placed under vacuum. A taper at at-

mosphere can easily support several milliwatts of optical power without any adverse effects; no power limitations such as those observed under vacuum have been seen with tapers at atmosphere, although we have not attempted any light levels above approximately 10 mW. However, under vacuum, tapers have regularly had their efficiency drop to near zero, and in some cases physically break, with tens of microwatts of light. The level of light at which these effects occur appears correlated with the total original efficiency of the taper in question. While we do not have enough data to develop a trend where the exact power threshold was measured prior to the taper breaking, we do know that a taper that was 4% efficient died with 17 μW of light while another taper that was 32% efficient died at 45 μW. Other tapers have died with measured powers of 20 and 70 μW; however, these light levels were not slowly ramped up as they were for the previously mentioned tapers, therefore we do not know what the lowest power levels were that would damage these particular tapers.

In most of these cases, not only did the taper efficiency drop to zero but the fiber itself appeared to have melted when inspected with a microscope. From first glance, the main difference between tapers under vacuum and those at atmosphere is that those under vacuum do not have convection to aid in heat dissipation. For a simple analysis, the heat rate equations are given by:

$$\dot{Q}_{Total} = \dot{Q}_{in} - (\dot{Q}_{cond} + \dot{Q}_{conv} + \dot{Q}_{rad}) \tag{2.1}$$

which can be written as [53]:

$$mC\dot{T} = P_{in} - (\pi r_{taper}^2 k_{silica} \frac{dT}{dx} + 2\pi l k_{air} \frac{\Delta T}{ln(\frac{r_{air}}{r_{taper}})} + 2\pi l r_{taper} \epsilon \sigma T^4) \tag{2.2}$$

The total change in temperature of the taper from a given flux of heat, $\dot{Q}_{Total}$, is determined by the temperature T, mass m, and specific heat C of fused silica, which is $\simeq$ 700 J/kg·K for standard atmospheric conditions. The rate of heat loss from conduction is given by $\dot{Q}_{cond} \simeq -kA_{cs}\frac{dT}{dx}$, where $k_{silica} = 1.3\frac{W}{mK}$ is the thermal conductivity of silica, $A_{cs} = \pi r_{taper}^2$ is the cross-sectional area of the taper, and $\frac{dT}{dx}$

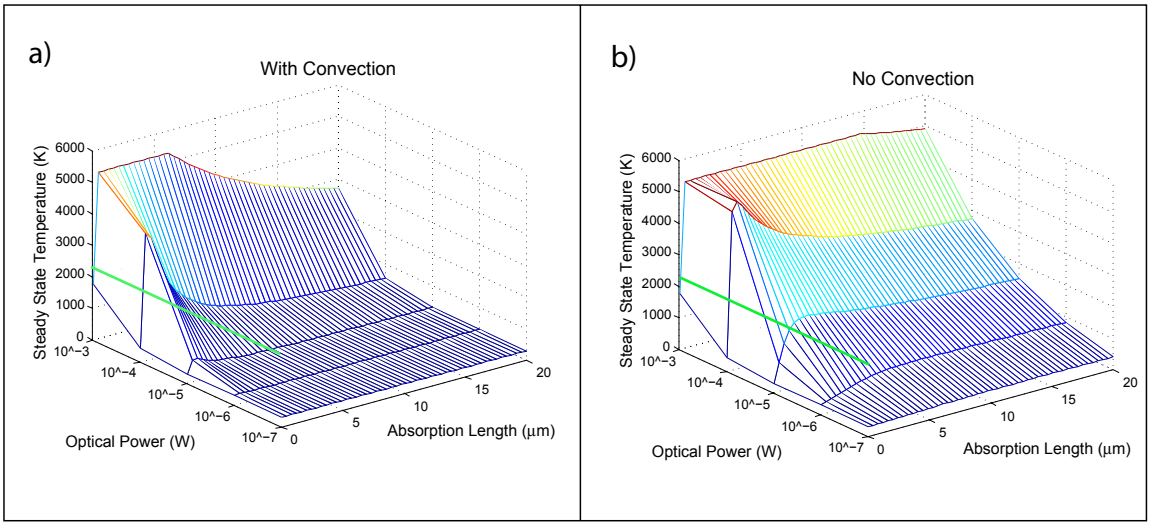

Figure 2.13: Calculation of equilibrium temperature reached by taper as a function of absorbed optical power and heat region length. Heat dissipation mechanisms included in both calculations are conduction and radiation. In order to simulate the difference between atmospheric and vacuum conditions, respectively, equilibrium temperature in (a) is calculated with convection and in (b) without convection. The melting point of fused silica is denoted by the green line at T = 2300 K. Note that in (a), the case which mimics atmospheric conditions, the steady-state temperatures are largely below this melting point. As the absorbed power becomes larger and the heat region smaller (thus more intense) this simulation expects that tapers will burn. By contrast, the vacuum conditions depicted in (b) where there is no convection lead to temperatures exceeding the melting point of fused silica over the range of heat regions for absorbed optical powers as low as tens of microwatts. This simple calculation shows that the lack of convection in vacuum can indeed be responsible for melting of tapered fibers by absorbtion of low light levels over localized regions.

is the rate of change of the temperature of the taper along its length. The rate of heat loss by convection for a cylinder of radius r_{taper} and length l is given by $\dot{Q}_{conv} = 2\pi l k_{air} \frac{\Delta T}{ln(\frac{r_{air}}{r_{taper}})}$, where r_{air} is the radial distance from the surface of the cylinder over which convection in air will occur, $k_{silica} = 0.024 \frac{W}{mK}$ is thermal conductivity of air, and ΔT is the temperature difference in Kelvin between the silica and the surrounding air. Rate of heat lost by radiation, $\dot{Q}_{rad}$, is given by the black body equation, where ϵ is the emissivity, $\simeq 0.8$, σ is the Stefan-Boltzmann constant $\simeq$ 6x10^{-8} $\frac{W}{m^2K^4}$, and T is the temperature of the taper in Kelvin. For fused silica at atmosphere the melting temperature is $>$ 2300 K.

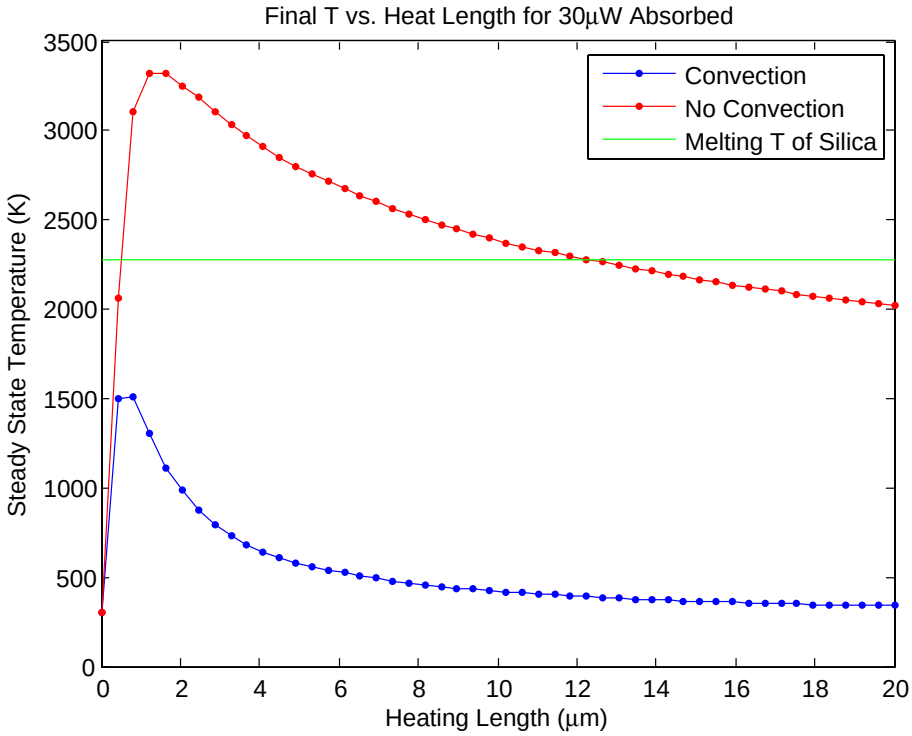

Figure 2.14: Calculation of equilibrium temperature reached by taper as a function of heat region length for 30 μW absorbed optical power. The blue trace shows the equilibrium temperatures reached when convection is present, while the red trace is without convection. The green line denotes the melting temperature of fused silica. For the majority of heat region lengths the temperature of the tapered fiber under vacuum (red) exceeds the melting point of fused silica, thus leading to breaking of the taper. However, the taper in air remains significantly below the melting point for all heating ranges calculated.

In order to determine whether the absence of convection is enough to cause a taper to melt with optical powers of order microwatts, a numerical analysis of this equation was performed for various heat region geometries and absorbed optical powers. In order to find the maximal contribution from each component of heat dissipation, as well as for simplification, the approximation has been made that the heating region of the taper is at a constant temperature while the air and tapered fiber surrounding it are at room temperature 300 K. Equation 2.2 is integrated over time in order to determine $T_{taper}(\infty)$ for various heat regions and absorbed powers. The results are presented in Figure 2.13 for a range of absorbed optical powers and heat ranges. A

slice of the plots in Figure 2.13 at 30 μW of absorbed optical power is shown in Figure 2.14 in order to clearly see the contrast in steady-state temperatures when convection is or is not present.

The comparison of the case with convection present (Figure 2.13a) with that under vacuum, and thus no convection (shown in Figure 2.13b) clearly demonstrates the significant effect that convection has on the ability of the tapered fiber to dispense of heat accumulated due to imperfections and absorbtion. In Figure 2.13a the steady-state temperatures are largely below this melting point, denoted as the green line at T = 2300 K. By contrast, the vacuum conditions depicted in Figure 2.13b lead to temperatures exceeding the melting point of fused silica for heat regions ranging from 10 nm to 20 μm, and absorbed optical powers as low as tens of microwatts. This behavior is in clear contrast to the behavior of the taper in the presence of convection and supports the claim that the melting of tapered fibers under vacuum is due to the lack of cooling due to convection. It should be noted that as the absorbed power becomes larger and the heat region smaller (thus more intense) this simulation expects that tapers will burn even in standard atmospheric conditions. This behavior should be tested in future experiments.

2.6.2 Getter Priming

Whenever new getters are installed they need to be primed in order to emit efficiently and cleanly. While the chamber is pumping down we begin running a low current through the getters. We gradually increase the level of current until the pressure in the chamber reaches $\simeq 10^{-7}$, at which point we wait until the pressure drops back down to a level of $\simeq 10^{-8}$; this drop can take anywhere from a few minutes to a few hours. This process is continued until the current is at a level of about 4–5 Amps, at which point cesium should be emitted. This can be tested by looking for fluorescence in the MOT beams, although the current level at which an adequate MOT can be built is much lower than that which produces visible beam tracks. Caution should be taken to avoid putting too much current through the getters, as they can release

their entire store of cesium at once if overheated.

2.6.3 Toroid Cleaning

After many hours of dropping atoms on the toroid chip, Cs begins to accumulate on the surface. This accumulation causes the resonance to shift to lower frequencies, as if heated, due to the effectively larger diameter of the toroid. Even a monolayer of Cs, which is approximately 1 nm [54], equates to a change in circumference of $\simeq$ 6 nm. Considering the free spectral range, approximated in a toroid by $\Delta\lambda_{FSR} = \frac{\lambda^2}{2\pi nR}$ [55], of this 22 μm radius toroid is about 3.5 nm, the shift due to cesium deposition can be quite significant. In addition, this cesium accumulation also causes the resonances to broaden due to additional scattering. However, we have found that we are able to "clean" the toroids by raising the temperature with the peltier by a few Kelvin for a few hours. After this mild bake, the resonances seem to be restored to their previous state. Unfortunately though, this does not work for removal of other material which may be emitted from the getters.

2.7 Improvements for Future Experiments

Given that the goal and scope of this experiment was primarily to observe first interactions between single atoms and a whispering gallery mode resonator, there are many improvements that can be made in future generations. Specifically, the ability to not only achieve critical coupling in vacuum without the taper contacting the toroid but to be able to lock this separation would allow much more flexibility in choice of resonance, as well as extend the lifetime of a given resonator. This has been accomplished, preliminarily, in a table-top apparatus detailed in Chapter 6. While this initial locking was accomplished outside of vacuum, all components used are vacuum-compatible and adaptation to a vacuum chamber should therefore be straightforward.

Trapping is of course a highly desired goal in order to have the ability to probe such phenomena as photon statistics. However, due to technical difficulties arising from

such factors as van der Waals forces near the surface and a very small modal volume this is a daunting task. One proposed method of trapping is to use a two-color trap [40] wherein beams both red and blue detuned from the atomic transition are injected into the mode of the cavity. The red beam acts to attract the atom to the surface while the blue beam repels. The power and detuning of each beam are adjusted to create a trapping region at a set distance from the surface of the toroid. However, higher efficiency tapers are necessary to potentially support the higher optical powers necessary to optically trap atoms near the toroid surface. The behavior of tapers with various efficiencies under vacuum needs to be investigated more thoroughly to evaluate the feasibility of using them to inject high optical powers into the toroid under vacuum.

Another possible improvement would be to use a standing wave, rather than a traveling wave as we currently do, to excite one of the native modes of the toroid. This would allow us excite only one of the standing wave eigenmodes visible in Figure 2.2 rather than both. This is desirable because we would not only have a system closer to that of a Fabry-Perot, which has one eigenmode excited at a time, but we would also ensure that any photons we detect did indeed interact with the atom. At this point, a photon will 50% of the time be in the wrong mode to interact fully with an atom.

Chapter 3

Tapering of Optical Fibers

The purpose of this chapter is to provide an overview of the taper pulling process, from the construction of an apparatus to the subtle techniques which determine the overall efficiency of a taper. While tapering of fibers has been developed by other groups [56, 17, 41], I have learned many skills which are worthwhile to pass on.

A fiber is tapered by applying a heat source to a section of the fiber while pulling each end in opposite directions. Commonly used heat sources are CO_2 laser beams [57] [58], small ovens [59], sapphire cylinders [60], and (as we use) a torch [17]. In order to determine the efficiency of a taper, as well as to ensure that it is single-mode for the specified wavelength, we inject light into the fiber and monitor the power output on a photodetector. Based on the behavior of this signal as a function of pull length, we can determine when the fiber has been tapered to the appropriate thickness.

3.1 Measures of Taper Quality

A standard fiber consists of a glass core surrounded by a glass cladding, all coated by a plastic buffer (removed at the tapering site), which gives the fiber bending ability. Due to a difference in the indices of refraction in the core and cladding, the light is confined via total internal reflection to the core. In 852 nm single-mode fiber the core is approximately 5 μm, while the entire glass portion of the fiber (core plus cladding) is 125 μm. As the fiber tapers, the core becomes exceedingly thin and the light is no

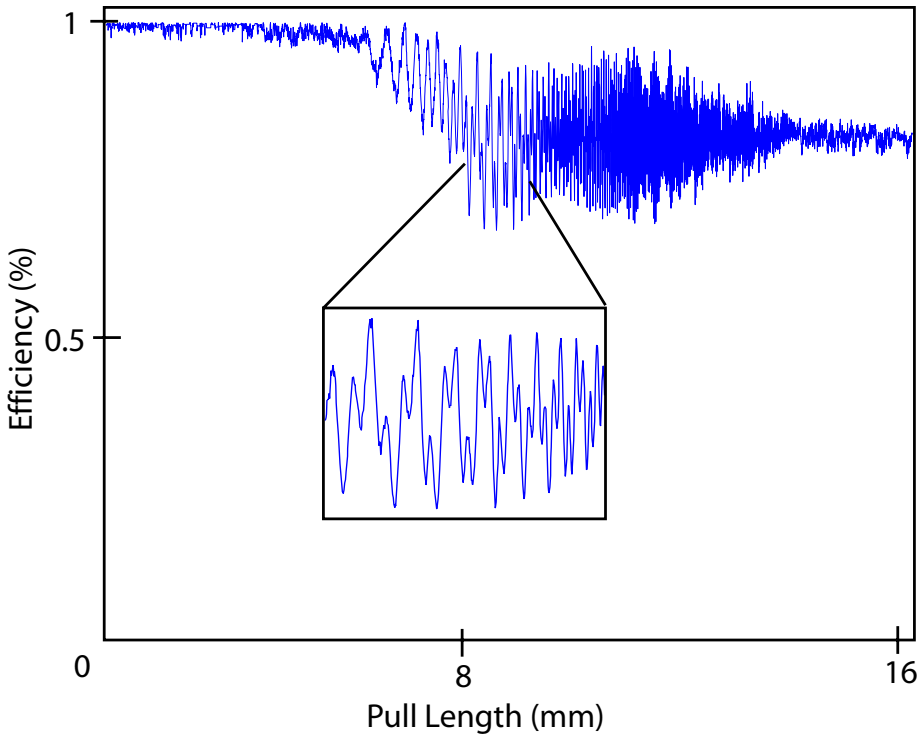

Figure 3.1: The normalized laser power transmission through the fiber while being tapered is shown here as a function of pull length. Oscillations occur as the fiber thins and the core mode interferes with higher-order cladding modes. The taper is single-mode once these oscillations cease.

longer confined between the core and cladding. Rather, the light is now confined by the boundary of the cladding and air. Once this transition occurs, multiple optical modes will be supported until the fiber (which is $> 99.8\%$ cladding) is on order of 1 wavelength of light in diameter, in our case < 1 μm. It is at this point, when the taper only supports the fundamental optical mode, that the taper is at the correct thickness for coupling to the toroid mode.

Figure 3.1 shows the normalized transmission through a typical taper as a function of the length that the fiber is stretched. The oscillations in the transmission are due to the interference between multiple optical modes supported at a particular taper thickness. As shown in the inset, there are many modes interfering to different degrees with respect to the thickness of the taper, manifesting themselves as frequencies in the oscillations, hence producing beat notes [17]. The point at which these oscillations end is when there are no higher-order modes supported to interfere with the fundamental

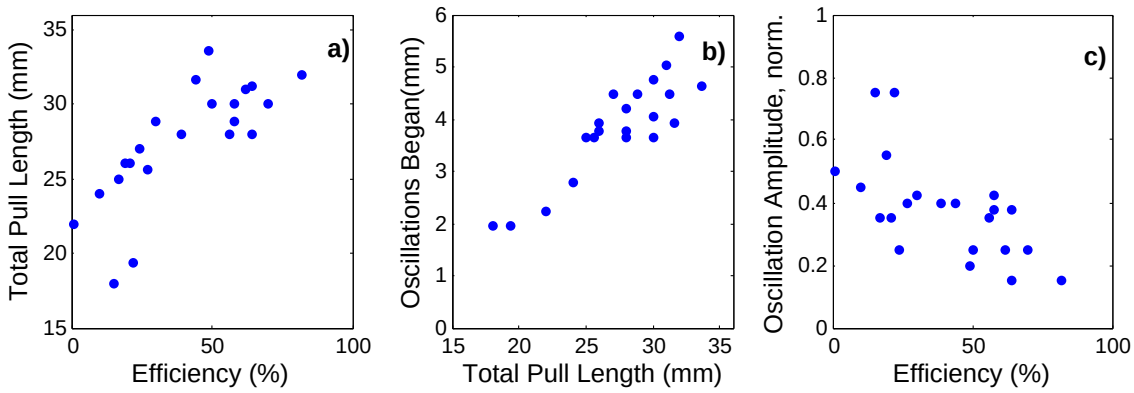

Figure 3.2: (a) Total pull length (mm), (b) pull length at which oscillations began (mm), and (c) size of initial oscillations (%) versus Final taper efficiency (%)

mode; the taper is then considered to be "single-mode". Any pulling beyond this length will increase the amount of the fundamental mode that will reside outside of the fiber in the surrounding air or vacuum as an evanescent wave. It is precisely this evanescent wave which is coupled into the optical mode of the toroid.

The final efficiency of a taper is a function of many variables which will be discussed in detail later in this chapter, such as torch alignment, gas flow into the flame, fiber alignment, and cleanliness of the fiber. Problems in these variables manifest themselves in the transmission pattern through the fiber, shown in Figure 3.1. As shown in Figure 3.2, the point at which the oscillations stop (i.e., when the taper becomes single-mode), the pull length at which the oscillations begin to occur, and the magnitude of the oscillations are directly correlated to the final taper efficiency. For a taper to be efficient, the radius must change slowly enough along the length of the fiber, dr/dl, to effectively contain the fundamental mode (i.e., it must change adiabatically). As dr/dl, approaches adiabaticity, shown in [16] to occur for a core taper angle dr/dl $< 10^{-4}$, the final efficiency trends towards unity. This is evident in Figure 3.2a in which the final length of the tapered region is plotted as a function of the final taper efficiency. This shows that the longer the taper (for a constant heated region) the higher the final efficiency. Given that the final radius for all pulls is the same (the thickness at which the cladding/air interface support one optical mode), this shows that a slower change in fiber radius over the length of the fiber will lead

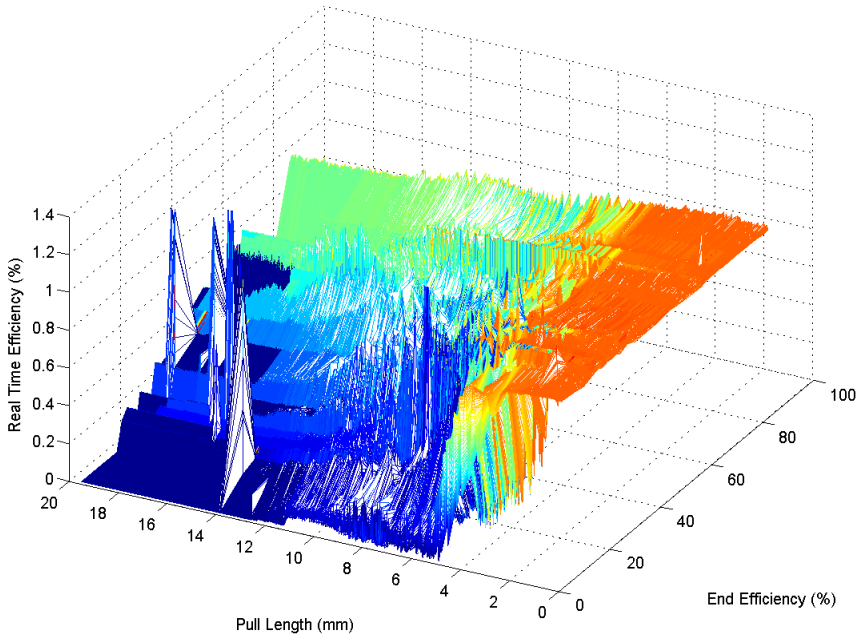

Figure 3.3: Normalized taper efficiencies as a function of final taper efficiencies (%) and stretch length (mm)

to a more efficient taper. It is necessary to note that in order to achieve a truly adiabatic taper one must use a heating region that is tuneable, such as by dithering the position of the torch in a time-dependent manner [61]. In a simple model for a constant heating region that does not take into account any external factors, such as taper torsion or misalignment, the pull length is given by

$$x = -2L_0 * ln(\frac{r_f}{r_0})[61] \tag{3.1}$$

where -L_0 is the length of the heating region and r_0 and r_f are the initial and final fiber radii, respectively. Initial and final radii values of 62.5 μm and .5 μm, together with a heating region of approximately 3 mm, give a pull length of $\sim$ 30 mm, which is consistent with our observations. Variability in this final pull length can be minimized with careful alignment, as described in the next section.

When this transition occurs too rapidly the fundamental mode begins to interfere with higher-order cladding modes [17], observable as the oscillations of Figure 3.1.

Earlier occuring oscillations are associated with shorter, and hence steeper dr/dl, tapers as shown in Figure 3.2b, which shows the pull length at which oscillations began versus the end taper length. The more severe the interference, the larger the oscillations and the less efficient the final taper. Figure 3.2c shows that the greater the peak-to-peak amplitude of early oscillations, the lower the efficiency.

Tapering that occurs too rapidly is often a manifestation of misalignments in the taper pulling setup. For example, when the taper is not heated enough due to either the flame being too far away or the gas flow being too low, the heated region is too small and will cause the tapering to occur faster than desired. Moreover, if there are misalignments in the fiber clamps which cause either a torsion or a bend in the tapered region, this produces results similar to tapering which occurs too rapidly (as the light which is being confined by total internal reflection is hitting the surface at an angle which is enhanced on one side by the amount of the bend). Unfortunately, these problems in the pulling setup have similar (often indistinguishable) characteristics in the taper throughput trace. In order to debug the system we must use other input, such as visual signals from the microscope. This will be addressed later in the chapter when we discuss alignment.

3.2 Apparatus

3.2.1 Components

As shown in Figure 3.4, the tapering apparatus consists of clamps mounted on motors which hold and stretch, a hydrogen torch to heat, and an imaging system for inspecting the fiber. The hydrogen flows from the regulator, through a flow meter, to a fine-adjust valve and small-diameter tubing system which regulate low flow rates. The gas is then emitted from a HTM-0 torch head which is mounted on a 3-axis translation stage. The fiber is held on either end with Ericsson FSU 250um Fiber Holders that are mounted atop Oriel Encoder Mike actuators. The actuators are both controlled by one 18011 Oriel Encoder Mike Controller. The imaging system consists

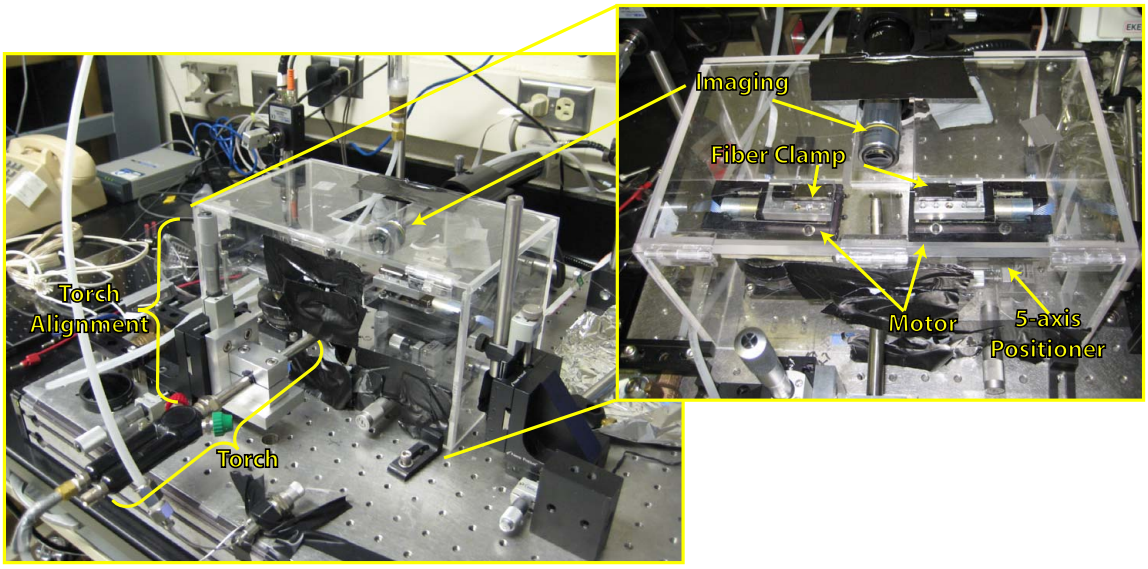

Figure 3.4: The taper pulling apparatus is shown with the key components labeled. The torch is attached to a three dimensional linear translation stage for alignment purposes. The majority of the apparatus is contained inside a plexiglass box in order to minimize air currents and dust in the vicinity of the tapered fiber (the inset shows, from above, the components contained in the box). The fiber is imaged with a microscope that is mounted to a positioner in order to align the microscope to the flame region. The fiber is held on each end of the flame by a clamp, which is in turn mounted to a motor. The rightmost clamp/motor is mounted atop a five-axis translation stage that moves along the three linear and two tilt dimensions. This allows the two clamps to be made collinear in order to avoid any torque on the fiber that will cause bends and losses in the final taper.

of a Navitar 12x Ultrazoom 1050503 microscope with a Hitachi KP-d20AU camera attached, all mounted on a three-axis translation stage. The output of the camera is sent to a monitor which is used for aligning the system as well as monitoring the tapering behavior in real time.

3.2.2 Fiber Alignment

The alignment of the fiber in the pulling device is critical in obtaining high-efficiency tapers. Bending or torsion of the fiber will manifest itself, once the fiber begins to thin, as large oscillations and lowered efficiency in the light throughput of the fiber. To minimize these effects, the clamps which hold the fiber on either side of the flame must be carefully aligned so that both ends of the fibers are collinear. Additionally,

they must be capable of positioning the fiber to the same orientation and location to within $\sim 10\mu$m, or 10% of the diameter of the untapered fiber each time a new taper is pulled.

Critical in achieving this careful, reproducible alignment is the quality of clamp which will be holding the fiber. The clamps which have worked best in my experience consist of a v-groove, machined specifically for 250 μm diameter fiber, in which the fiber will be held with a rubber arm that is held down with magnets. The v-groove must be free of dust and long enough for the fiber to lay flat. Dirt in the v-groove will cause the fiber to bend in an unrepeatable manner and thus not align properly to the opposite clamp. The rubber which holds the fiber in the groove must be of uniform thickness and elasticity in order to provide a constant force across the length of the fiber in the v-groove. Keep in mind that solvents will irreversibly alter the elasticity of rubber, causing it to become hard and brittle and should therefore be avoided. Nonuniform force from the rubber or rubber that is too long and thus hangs over the edge of the v-groove will cause the fiber to bend, again in a manner which varies every time a new fiber is clamped, making consistent alignment to within 10 μm impossible. I have had the most success with the Ericsson FSU 250 um Fiber Holders that are designed to work with fiber splicers.

Once repeatable positioning has been obtained with proper clamps, the clamps must be carefully aligned to be collinear. In this configuration, each clamp is mounted to the top of a motor which will pull the fiber, which is in turn mounted to a positioning stage. The left clamp/motor (Figure 3.4) is mounted to a stage which controls only the vertical (z) position, allowing the fibers to be within the range of the imaging system and torch. The right clamp/motor is mounted to a stage which controls x,y,z, and two degrees of tilt.

Alignment of the fibers is done using the imaging from the microscope and light propagating through the fibers. A fiber is inserted into each clamp, with each fiber ending in the center of the clamps. They are visually aligned such that both ends are roughly collinear and are then more carefully aligned until light propagates from one fiber end across the gap into the other. The fibers that are used for the alignment, as

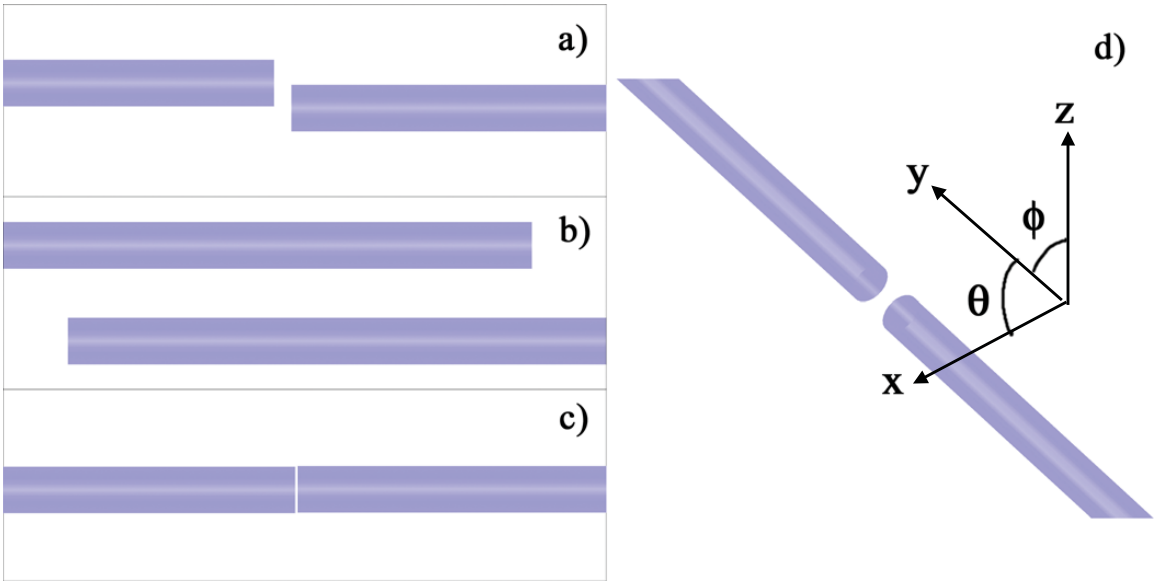

Figure 3.5: Simulated screen shots of fiber ends during the alignment of clamps. (a) Roughly align two fibers to be in focus together; (b) adjust θ and ϕ on five axis stage to make fibers parallel; (c) bring fiber faces together for fine alignment

well as for pulling a taper, must be very straight. As fiber generally is shipped and stored on spools, it has acquired a curvature that must be removed by heating. Two apparatuses that I have found adequate for straightening are a heat gun and a fiber oven. A heat gun on a low setting, to avoid blowing the fiber away, waved for about ten to twenty seconds about six inches away from the fiber will take away much of the curve. The other apparatus, a fiber oven, is convenient if one is handy (these ovens often come with a fiber splicer and are used to attach a heat shrink sleeve over a fiber splice). Slowly dragging the fiber through the oven a few times (again, for about ten to twenty seconds) will relax the fiber. After either heating method, hold the fiber up by one end, examine for any remaining bend, and repeat if necessary. Once the fibers are straightened, the fiber ends which will be aligned to one another need to be cleaved. A cleaver scores the fiber with a sharp blade and applies a stress which splits the fiber, leaving a very smooth surface perpendicular to the face. This is necessary in order to do the final fine alignment step which propagates light from one fiber to the other across the gap.

After straightening and cleaving, insert one fiber into each clamp with ends meet-

ing in between clamps, centered on the imaging screen. The end that is not between the clamps ("outside end") of one fiber should have light entering, and the outside end of other should be connected to a photodetector using a bare fiber adaptor (we use the Thorlabs BFTU). Adjust the zoom on the microscope until the width of a fiber is about 1/4 the height of the screen (Figure 3.5a). This visual representation will be the error signal used to align the fibers. The fiber which is only capable of vertical adjustment will remain stationary and thus we will focus the imaging on this fiber. Adjust the x axis of the five-axis stage so that this fiber is also in focus, then lower it below the other and move it toward other fiber so that they overlap significantly, for many screens (Figure 3.5b). In order to align both the θ and ϕ tilts, scan the microscope along y and adjust θ and ϕ until both fibers are in focus at same time as well as parallel. To make parallel, measure the distance in z between the fibers on the screen for two y values that are as far as possible from one another, adjusting ϕ until these distances are equal. Lastly, retract the y axis of the five-axis positioner until both fibers are on the screen, adjust z until they are level with one another, and bring the faces of both fibers as close as possible without touching (Figure 3.5c). At this point, observe the output of the photodetector that the output fiber is plugged into for any signal that shows the light from one fiber is traversing the gap into the other fiber. Make fine adjustments in x, y, and z (Figure 3.5d) in order to maximize this signal.

3.2.3 Torch Alignment

One of the more difficult aspects of aligning the taper pulling setup is that of flame alignment. The flame size is the largest variable due to the low flow rate of hydrogen gas needed to produce an ideal flame size. The flow rate can be roughly determined by observing the shape of the flame from the torch. The flame should approximate a hemisphere, as in Figure 3.6b. The combination of the fact that hydrogen flames are blue with a very low flow rate makes the flame difficult to see. In order to observe and hence tune the flame, the room must be made completely dark. It is important

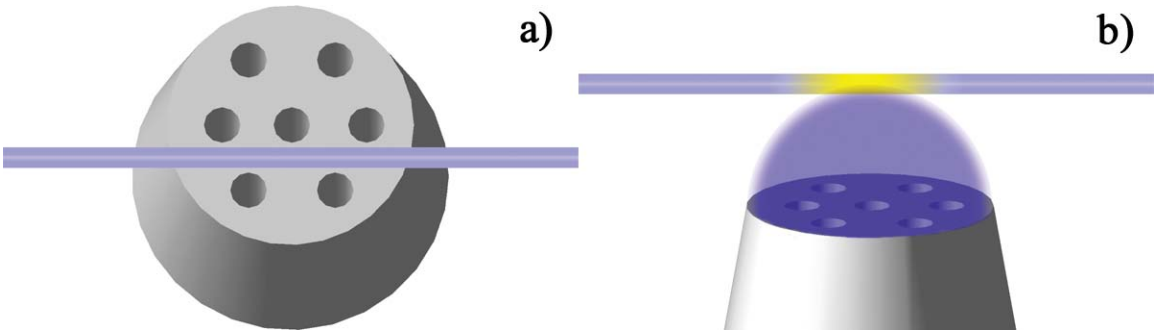

Figure 3.6: Position of torch relative to fiber (a) from above and (b) from the side with flame. The glow in the taper indicates adequate heat in the region of the fiber

that the flame not be too strong as the force from excessive gas flow will bend the fiber as it thins, leading to losses. However, the flame must be large enough to heat a long enough section of fiber for near-adiabatic tapering.

For rough torch alignment, begin with the flame off and move the torch so that the fiber, viewed from above with the torch pointing away, is positioned as in Figure 3.6a. The height of the torch is aligned by observing the flame position relative to the fiber. Note that the plastic buffer must be removed from the section of fiber which will be in or near the flame. The buffer will ignite and burn the length of the fiber until it hits a barrier, such as the fiber clamp. The fiber should be in the flame just enough that there is a slight glow visible when the room is completely dark, as shown in Figure 3.6b.

Fine alignment is a more tedious process which requires pulling tapers in order to obtain feedback. Due to variability from one pull to the next, it is best to pull at least three tapers with each setting and average the taper responses. A more detailed explaination for how to pull a taper is given in the next section. The imaging system will give the initial feedback necessary to the torch alignment. Here we can get a rough idea how fast the radius is tapering, how many waists are being formed, and if the taper is being blown by the hydrogen flow. Generally, if the fiber is tapering too quickly, it needs to be heated over a larger region. This means we need to move the fiber slightly more into the flame. However, if the fiber is developing two waists then it is too deep in the flame. Here the fiber is seeing the individual flame components

produced by the holes in the torch rather than the more homogenous heat region that lies further away from the torch head. Furthermore, as the fiber thins, if it appears to be drifting off the imaging screen, then it is in the path of the gas flow. To remedy this situation, the torch can be moved closer to the fiber so that the gas flows beneath it.

Once the fiber appears to be tapering with one waist, at a slow rate, and not moving off the screen, final fine adjustments can be made to the torch position using the signal from the light propagating through the fiber as a function of pull length. As discussed in the previous section, high-efficiency tapers have oscillations that are smaller in amplitude and start later than their low-efficiency counterparts. Again, pull at least three tapers per setting, finely adjust one axis on the torch translation stage at a time, and observe whether the taper output improves. Repeat for both the height and distance from the fiber until tapers with the desired efficiencies are obtained.

3.3 How to Pull

At the beginning of each day, in order to establish a constant heat source, it is beneficial to light the torch and let it burn for 10 to 20 minutes in order to let the gas flow stabilize. This will help to eliminate any air pockets that may have formed in the tubing since the last time the torch was used. Be sure to turn the torch off before installing fiber to avoid burns as the flame is nearly invisible and extremely hot.

The cleanliness and straightness of the fiber is of the utmost importance in pulling successful tapers. Fibers that have either remnants of the plastic buffer or specks of dust in the heating region will taper unevenly and too quickly. Always begin by straightening the fiber using the heating techniques discussed in the previous section. This is crucial to avoid any unwanted bending in the taper. Laser light should be fed into the fiber at one end while the other is plugged into a simple photodetector to measure the DC power signal. To attach the bare fiber into the photodetector, use a bare fiber adaptor as described in the previous section. In order to obtain an

accurate reading of the laser power emitting from the fiber, it must be cleaved to remove rough edges of glass that will scatter the light away from the detector.

The section of the fiber that will be in the flame must be stripped of its protective plastic buffer in order to avoid this catching on fire. However, the length which is to be stripped should be kept to a minimum as the buffer is necessary to prevent the fiber from easily breaking. For the size flame we use, 1 to 2 cm is adequate. Additionally, when the fiber is glued to its final holder, the glue must be placed on the buffer or the fiber will likely break upon moving. In order to strip the buffer, use a specially designed, commercially available, fiber-stripping tool to remove the buffer down to the 125 μm diameter where glass begins. The tool I have found most useful resembles a wire stripper but is calibrated for the specific diameters of fiber. First, be sure the stripping tool is clean with no remnants of previous fiber buffers, as they can scratch and stress the fragile cladding. Hold the fiber firmly (you can even wrap the buffered section around your fingers for a better grip) and use the tool as you would on a standard electric wire, pulling with the stripper at an angle to the fiber. In order to clean the stripped region of fiber use a clean, disposable wiper, such as a Kimwipe®, wet with acetone. Each time the fiber is touched use a clean section of the wipe so as not to spread buffer fragments on the surface. Clean numerous times until there is a "squeaking" sound. After this point, ensure the stripped section of fiber does not touch any surface and is not dragged through air unnecessarily as it will pick up dust particles.

Once the stripped section is clean it is ready to be put into the clamps. First, it is necessary to eliminate any torsion in the fibers that may occur due to being rolled on a spool. Place the fiber in the clamp furthest from the photodetector. Using a scrap piece of fiber (which has been wiped with acetone or isopropynol to remove dust) that is approximately one foot long and bent into a U shape, lift the fiber that is to be tapered after the stripped section and drag it with the scrap fiber out to the end, allowing it to fall naturally. Repeat this one or two more times to ensure that any twisting in the fiber is eliminated. Now grasp the end of the tapering fiber, pulling taut, and place in the second clamp. Careful placement of the fibers into the

clamps is crucial in successful, reproducible tapering. Often, small misalignments in the clamps, specks of dust in the v-grooves, or a slight bend in the fiber will cause the fibers to not lie completely flat in the grooves of the clamps. To minimize this, unclamp the fiber one side at a time, pull taut, place in the groove, then— holding the fiber in the groove with a fingernail— gently close the clamp. Repeat on each side until the fiber between the clamps does not move when a clamp is fastened. At this point, visually inspect the entire heating region of the fiber using the microscope signal on the monitor. If any blemishes are noticed within the heating region then the fiber must be removed and cleansed once again with acetone.

3.3.1 Pulling Rates

After the fiber is installed, light the flame and begin the motors pulling at 25 μm/second. Continue to visually monitor the fiber, looking for visual cues such as "micro-cracks," [18] dual waists, and the fiber moving off the screen. While the last two cues are symptoms of poor torch alignment, the first is characteristic of either a dirty fiber or trauma induced in the buffer stripping process. These micro-cracks appear as lines perpendicular to the length of the fiber that glow in the flame. As the fiber is heated and stretched, these micro-cracks can form hot spots, causing the fiber to rapidly taper at this location and often times break. This cannot be corrected once the pull has begun, reaffirming the need to be vigilant in the cleaning process, as well as to not bend the fiber unnecessarily after the protective buffer has been stripped.

3.3.2 When Pull is Done

The fiber should continue tapering at a constant speed until the oscillations in the taper's optical transmission cease. At this point the taper is thin enough to be considered single-mode. For ease of usability in a coupling set up, it is beneficial to pull an extra length past this point, as you will then have more flexibility in choosing a coupling point in which the taper mode matches that of the toroid at a given distance. Generally, an extra 500 μm of pull is sufficient. Once the taper has pulled the desired

length, the flame and the motors must be turned off as close to synchronously as possible. Since this is difficult, the motors should be turned off slightly before the flame, so as to avoid breaking the fiber by pulling on it while cold. Once this is complete the tapered region will be very loose and will move with air currents. This movement is problematic in efficient coupling and the taper must be tensioned. To do so, zoom in as far as possible on the thinnest portion of the fiber. Run the motors at 5 μm per second in 1–2 second intervals until the fiber no longer moves when the air around it is disturbed (such as by a hand moving nearby). If the fiber is not bent, the efficiency will either stay the same or improve. If there is a bend in the fiber, the efficiency will likely decrease by a few percent in the tensioning.

3.3.3 Removal of Taper

Since a tapered fiber is very fragile and will break with even slight strain, in order to move it to a setup where it can be coupled to a toroid, it must be attached to a device that will immobilize it. I have found that a glue of some sort is a better solution than clamping. Clamping requires the device to be aligned to the fiber to within very close tolerances to avoid stressing, and possibly breaking, the taper when it is grabbed on either end. Glue, on the other hand, is forgiving in that the fiber sinks into the glue while it is still liquid. Qualities to look for in a glue are short curing times, rigidity, and strength. The longer a taper sits in air the more likely it is to accumulate light-scattering dust particles, hence a speedy gluing process is necessary. It is important that the glue is hardened throughout its volume and not simply on the surface; a drop of glue that is liquid on the inside of a hardened shell will still allow the very thin fiber enough movement to cause it to break, given that this only takes a few degrees of motion on one end. For the same reason, the glue must be rigid in the end. Finally, brittle glue can easily break, hence breaking the taper, when a fiber is inadvertently pulled on outside of the immobilizing apparatus. Lastly, if the taper is to go in a vacuum chamber then the glue must not outgass. One glue which meets all of the above criteria is Ceramabond 835-M. This particular glue

is ceramic, thus not outgassing, and sets in 10–45 minutes, dependant on the amount of thinner used in the solution. Among glues that are not vacuum-compatible but will work in external coupling setups, Devcon Super Glue cured in $\simeq$ 6 minutes and was much stronger compared to other similar super glues and five-minute epoxies, most of which were not solid throughout after 15 minutes.

3.3.4 Labview

In order to record the transmission through the taper I have written a program using Labview which displays and records the output from the photodetector and the normalized efficiency in real time. A detailed description is given in Appendix A.

Chapter 4

Characterization of Toroidal Resonators

Over the course of characterizing many toroids it became clear that an efficient method that would enable us to quickly acquire a toroid's spectra over several free spectral ranges (FSR) would be extremely useful. By "characterize" we mean to probe and record all of a particular toroid's resonances for both orthogonal polarizations. This allows us to not only quickly locate the best resonance for our application, but to also monitor the behavior of a toroid's spectrum over time (e.g., is the entire spectrum shifting in frequency due to accumulation of cesium on the surface?). Also, in an environment when contact mode is used, as discussed in Section 2.5.1, resonances are often difficult to locate. Therefore, having an effective "map" of the spectrum eases the process of locating a particular resonance in an environment when temperatures, and hence frequencies, change and fine motion probing is not possible.

Toroids degrade quickly in atmospheric conditions due to water vapor and other impurities becoming embedded into the ultrapure surface, causing additional scattering and absorption which limit the lifetime of a photon in the mode of the cavity. Quality factors can degrade by orders of magnitude in the first few minutes, with the degradation slowing after this initial exposure to water vapor. Therefore, minimization of the time that a toroid is outside of vacuum is critical. Thus, I have developed a system which is able to characterize a toroid's entire FSR in a matter of minutes.

4.1 Characterizing Apparatus and Results

Ideally, when characterizing a toroid, the taper will be far away from the toroid surface so that we are well into the under-coupled regime, defined in Section 5.1.1. This will allow us to determine the intrinsic line width κ_i and splitting h of each resonance, with minimum influence from the external coupling κ_{ex}. However, when far under-coupled the resonance dip is very small, as demonstrated in Figures 5.1 and 5.4. A toroid with a radius of 15 μm has an FSR of $\simeq$ 6 nm [1], or about 2 THz, which means a resonance with a line width of 10 MHz, corresponding to a quality factor[2] of about 10^7, is about 10^5 times smaller than the FSR. In order to find these very narrow, small resonance dips we exploit the well developed method of using RF sidebands to create an error signal [50]. This error signal is essentially the derivative of the signal transmitted through the toroid. Since this signal is zero everywhere except where there is a frequency dependent feature, the signal-to-noise ratio is greatly improved. This is due to the fact that it is generally simpler to amplify a small signal in a quiet background than it is to observe a small dip in a large background.

In our characterization apparatus, the probe laser acquires RF sidebands of up to 1 GHz— a much larger frequency than any of the resonances that we are interested in recording— by going through a phase modulator. We monitor the probe output of the taper (P_F, as defined in Chapter 2), which exhibits the characteristic resonance dip. The AC portion of this output is mixed down with the RF frequency that is used to generate the sidebands to create an error signal. A small amount of the probe laser is tapped off before the phase modulator and is sent through a cesium cell saturation absorption setup [62]. The output of the saturation absorption gives us a well quantified frequency reference from the cesium D2 line transitions [3]. The inset Figure 4.1b shows a trace acquired from this cesium reference in which the trace has been zoomed into the lower frequency transitions of the D2 line. The frequency of the

[1] The free spectral range of a toroid can be approximated by $\Delta\lambda_{FSR} = \frac{\lambda^2}{2\pi n R}$ [55].

[2] The quality factor can be estimated by the line width of the resonance divided by the frequency location of the resonance, or $Q = \frac{\nu}{\Delta\nu}$.

[3] A useful resource for more information on the cesium D2 line can be found at http://steck.us/alkalidata.

probe laser is scanned over several nanometers in order to encompass an entire FSR. This characterization process is discussed in more detail in Section 4.2. Figure 4.1 is a representative output from such a characterization over the entire scan of $\simeq 15$ nm, where the blue trace is the output of the taper P_F, the purple is the error signal, and the green is the signal from the cesium source. It should be noted that it is extremely difficult to make out any resonances through the noise of the toroid output P_F, yet spikes are clearly visible at the resonance locations in the error signal. The zoom-in of the error signal in Figure 4.1c shows more clearly the repetition of a resonance over an FSR of this particular toroid. The fundamental mode resonance is clearly visible above the noise, allowing for quick characterizing. This particular trace is in the extremely under-coupled regime, thus we are only able to see the fundamental modes; higher-order modes are visible upon decreased taper-toroid separation. As shown in Figure 4.1d, each Lorentzian toroid resonance produces an error signal similar to that acquired from reference cells, such as cesium, in laser locking schemes. This has in fact been used to lock the laser to a particular toroid resonance, as discussed in Chapter 6.

An important phenomenon worth addressing is power broadening of a resonance [18]. When the frequency of a laser coupled to a toroid is tuned to a resonance, the amount of optical power in the toroid increases by many orders of magnitude, as addressed in Section 5.1.1. This additional power leads to heating of the toroid, shifting the resonance towards lower frequencies. Therefore, when the laser frequency is scanned across the resonance and the laser is scanning towards lower frequencies, the resonance will chase the laser and effectively broaden the resonance. If instead the laser is scanned toward higher frequencies, the resonance will be narrowed. Either of these shifts are problematic when attempting to characterize a toroid since accurate line widths are necessary. The degree to which the resonances are either broadened or narrowed is dependent upon the power in the laser; of course, less power will lead to less heating. The problem with using excessively low probe powers is that the signal-to-noise of the output of the taper degrades, making the already small under-coupled resonances even more difficult to find. Again, the error signal amplifies these

small signals out of the noise, allowing these resonances to be more easily found and characterized.

4.2 Experimental Details

The characterization setup consists of three main parts: optical components, electronics and computer control, and taper-toroid coupling. The optical components tune the frequency, polarization, and apply RF sidebands to the carrier signal. In addition a cesium source is used as an absolute frequency reference. The electronics supply the RF source for creating sidebands and create an error signal from the light exiting the toroid. Figure 4.2 is a schematic of these components. A computer runs a program written in Labview which controls the laser frequency as well as acquires the data. Finally, vast improvements to the system which controls the coupling between the taper and toroid have been made over the original system described in Chapter 2.

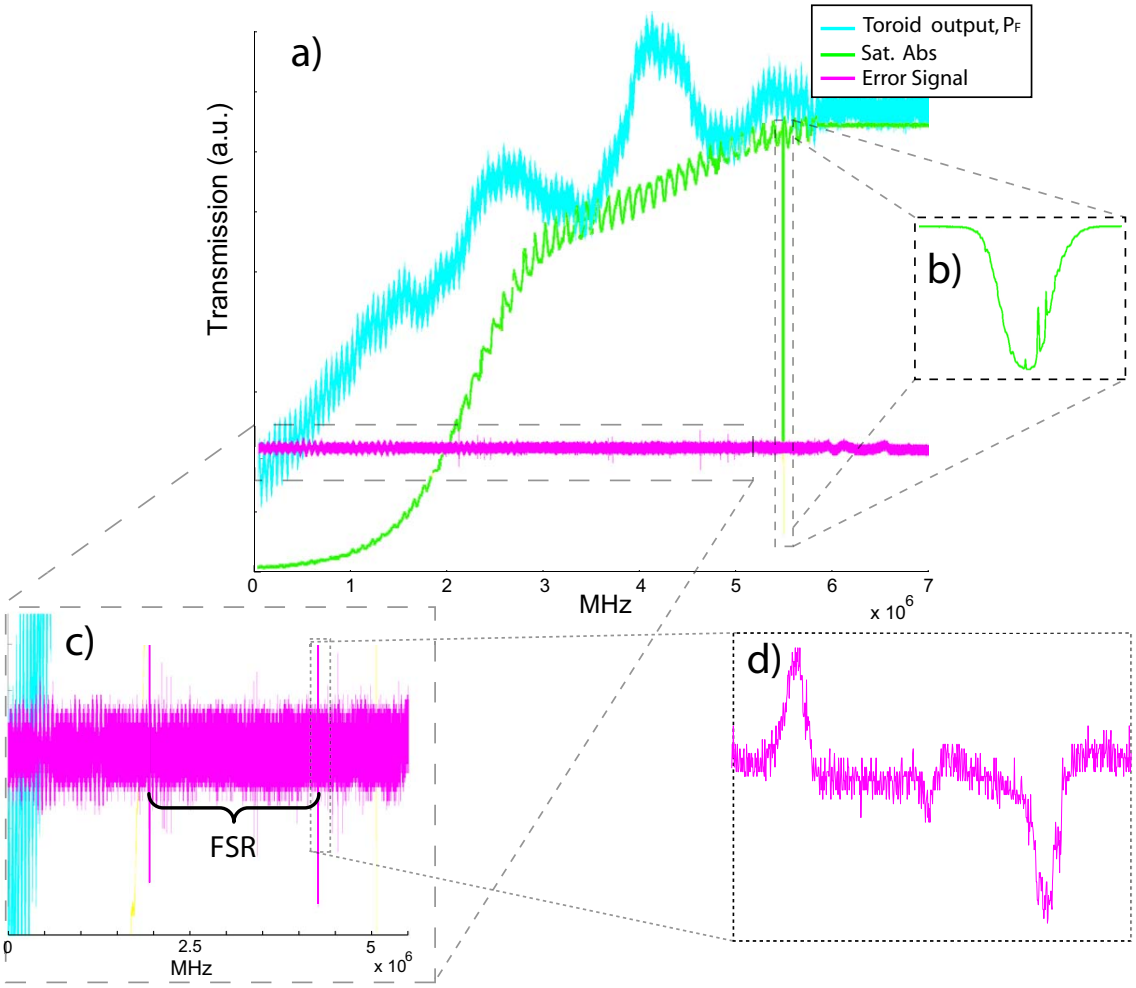

Figure 4.1: Shown is a representative output of a toroid characterization, where the blue trace is the output of the taper P_F, the green is the signal from the saturation absorption, and the purple is the error signal. The drop in power at lower frequencies is behavior of the laser as it scans over such a large range; this is not visible in the error signal because any DC offsets are lost in the signal mixing. (a) The entire scan of $\simeq 15$ nm is shown. Note that it is extremely difficult to make out any resonances through the noise of the toroid output P_F while spikes are clearly visible at the resonance locations in the error signal. (b) Zoom-in of the saturation absorption signal from the cesium cell; shown are the lower-frequency transitions of the D2 line. (c) A zoom-in of the error signal over more than one FSR of this particular toroid. The fundamental mode resonance is clearly visible above the noise, allowing for quick characterization. This particular trace is in the extremely under-coupled regime, thus we are only able to see the fundamental modes; higher-order modes are visible upon decreased taper-toroid separation. (d) A zoom-in of an error signal from one Lorentzian

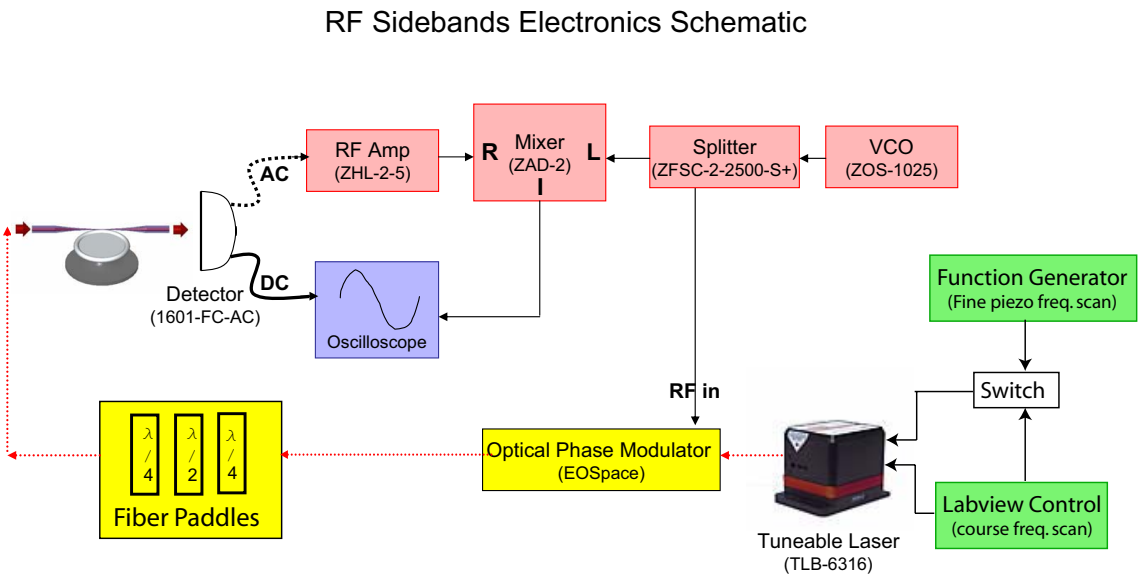

Figure 4.2: The frequency of a tuneable laser is either scanned over a fine range by tuning the piezo in the laser or over a coarse range using the laser controller; a Labview program controls whether fine or coarse scan is used, as well as the amplitude of the coarse scan. The light then goes through a phase modulator where it acquires sidebands corresponding to the RF signal generated by the voltage controlled oscillator (VCO). The polarization of the light is tuned by use of fiber paddles to optimize the depth of the toroid resonances (if none are visible then the polarization is left at an arbitrary value until resonances are located); it then enters the taper which is coupled to the toroid. The output of the taper is plugged into a high-frequency detector which splits the signal into its DC and AC components. The DC component, P_F, is the blue trace of Figure 4.1, and the AC component is amplified before being mixed with the RF signal in order to produce the error signal (purple trace in Figure 4.1).

4.2.1 Optical Components

In order to probe and record a full FSR of a toroid, the probe laser must be able to scan, mode-hop free, over at least 7 nm for a toroid with a radius of 15 μm. Our tuneable laser is the New Focus Velocity TLB-6316, which is capable of scanning from 838-853 nm, mode-hop free, where the D2 line of cesium occurs at $\simeq$ 852 nm. The laser will scan this entire range, or a portion thereof, when prompted by the Labview control. If a particular resonance is to be probed then a scanning range of hundreds of megahertz rather than tens of nanometers is desired; in this case the frequency is tuned by applying a triangle waveform from a function generator to the piezo tuning input on the laser controller.

The output of the laser is split into two paths. The majority of the light is coupled into polarization maintaining (PM) fiber while a small amount is sent into a saturation absorption setup. The output of the saturation absorption beam is detected on a standard Si detector which converts the power from the incident light into a voltage. This voltage is then collected and stored on the computer by Labview. This signal, shown in Figure 4.1b, is used as an absolute frequency reference. The distance between the various peaks and valleys is capable of being measured with extremely high precision and we can therefore use this to determine the line widths and frequencies of the various resonances.

The light which is coupled into the PM fiber goes through a fiber phase modulator where it acquires sidebands corresponding to the RF signal generated by the voltage controlled oscillator (VCO). The RF signal drives an electric field across a nonlinear optical material, in this case Lithium Niobate. The electric field changes the index of refraction of this crystal, thereby changing the phase of the emitted light. The phase is therefore modulated at a frequency equal to that of the driving RF.

The phase modulator we use, produced by EOSpace, is completely fiber-based and capable of producing sidebands of up to 9 GHz. This modulator minimizes losses since we do not have to take the light in and out of fiber, saves on space, and is less likely to be misaligned. PM fiber is required since the phase modulator is polarization

dependent. Care should be taken to avoid putting too much power into the sidebands. Since these sidebands are at a frequency different than the carrier by the amount of RF applied, the sideband light will not be resonant with the toroid at the same time as the carrier. This means that the level of darkness that can be achieved on critical coupling is limited by the amount of power in the sidebands. For characterizing toroids this is not a problem. However, if the error signal is necessary to lock the laser frequency to the resonance of the toroid in an application such as observing atom transits (Chapter 2), for example, then the RF power should be turned during the times in which transits are being observed.

After the phase modulator, the polarization of the light is tuned by fiber paddles in order to align the light to the chosen mode of the toroid, thereby optimizing the depth of the toroid resonance. The paddles apply a stress on a section of the fiber that has been coiled a specific number of times. A combination of three paddles, with varying lengths of fiber coiled, allows any polarization of light to be obtained at the output. Paddles were ultimately chosen over free-space wave plates due to the fact that polarization optimization for the specific resonance must be done after the fiber-based phase modulator as it requires light with a linear polarization. Were free-space wave plates used, the light would need to be taken out of fiber after the phase modulator, which is not efficient. Therefore, we could either use a free-space phase modulator or a fiber-based polarization control; due to component availability as well as space constraints, we chose the latter.

This fiber is then spliced to the tapered fiber, which is then coupled to the toroid. The power out of the toroid is coupled back into the taper and then detected on a photoreceiver.

Mathematically, the modulated light field entering the toroid can be represented as

$$E = E_0 e^{i(\omega t + \beta sin(\Omega t))} \tag{4.1}$$

where ω is the unmodulated frequency of the light (i.e., the carrier frequency) and β and Ω are the depth and frequency of the modulation, respectively. This can be approximated by

$$E \simeq E_0 e^{(i\omega t)}[J_0(\beta) + 2J_1(\beta)\sin(\Omega t)] \tag{4.2}$$

$$= E_0[J_0(\beta)e^{i\omega t} + J_1(\beta)e^{i(\omega+\Omega)t} - J_1(\beta)e^{i(\omega-\Omega)t}] \tag{4.3}$$

where $J_i(\beta)$ are the ith order Bessel functions of the first kind. Sidebands are evident in the last two terms of equation 4.3 in which their frequencies are shifted by $\pm\Omega$ with respective phases of (0,π). The electric field exiting the toroid can then be written as

$$E_{out} = E_0[J_0(\beta)\bar{a}_{out}(\omega)e^{i(\omega t} + J_1(\beta)(\bar{a}_{out}(\omega+\Omega)e^{i(\omega+\Omega)t} - \bar{a}_{out}(\omega-\Omega)e^{i(\omega-\Omega)t})] \tag{4.4}$$

where $\bar{a}_{out}(\omega)$ is the normalized complex amplitude of the field, $a_{out}(\omega)$, as a function of frequency as determined by the resonant structure, given explicitly by equation 5.3. When ω is near the cavity resonance and the modulation is much larger than the parameters of the cavity resonance, $\Omega >> \kappa, h$, the cavity has little effect on the far detuned sidebands, meaning $\bar{a}_{out}(\omega \pm \Omega) \simeq 1$. In this realm the field out of the toroid can be approximated as:

$$E_{out} \simeq E_0 e^{i(\omega t}[J_0(\beta)\bar{a}_{out}(\omega) + 2J_1(\beta)\sin(\Omega t)] \tag{4.5}$$

The quantity that we measure on the photodetector, optical power, is given by the square of the electric field given in equation 4.5, and, after some algebra, can be written as

$$P_{out} = P_C|\bar{a}_{out}(\omega)|^2 + 2P_S + 2\sqrt{P_C P_S}\sin(\Omega t)[\bar{a}_{out}(\omega) + \bar{a}^*_{out}(\omega)] \tag{4.6}$$

where terms of order 2Ω that are due to the sidebands interfering with each other have been dropped and the power at the carrier and sideband frequencies are given by $P_C = (J_0(\beta)E_0)^2$ and $P_S = (J_1(\beta)E_0)^2$, respectively. The first two terms only vary as fast as the frequency of the laser is swept, in this case 30 Hz. Since this is much slower than any of the other frequencies in the signal, this portion can be considered the DC component to the signal. Since the power in the sidebands is much smaller than that in the carrier, $P_C >> P_S$, the first two terms approximately represent the spectrum of the resonator for the carrier frequency.

The final term of equation 4.6 is proportional to the real component of the electric field out of the toroid, $Re(a_{out})$, shown in Figure 4.3. The real component of a_{out} is antisymmetric about the toroid resonance, enabling us to differentiate between a blue or red detuned probe laser. Note also that this term oscillates sinusoidally at the frequency of the RF sidebands, Ω. Since Ω, on order of 1 GHz, is much faster than the rate at which the frequency of the laser is scanned, this is considered the AC component and will be extracted with electronics as described in the next section.

For the detection, a 1 GHz bandwidth New Focus 1601-FC-AC photoreceiver is used to convert the optical power to a voltage. It is then internally amplified and split into DC and AC components. The DC is low passed at 20 kHz while the AC is high passed at 30 kHz. The DC output of the detector is proportional to the spectrum of the toroid and is displayed in blue as "Taper Output, P_F" in Figure 4.1. Together with additional electronics, the AC coupled output is used to create the error signal shown in purple of the same figure; this procedure is discussed in more detail in the following section.

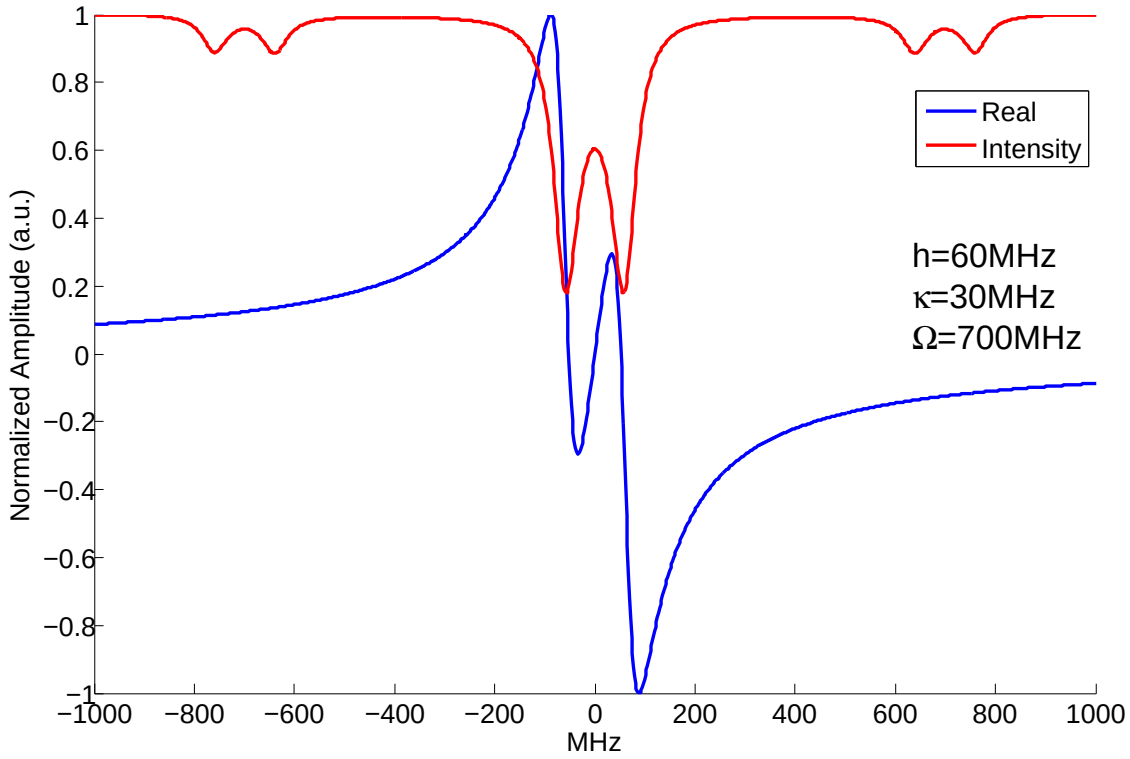

Figure 4.3: The real component of the electric field (blue) and the light intensity (red) out of the toroid are calculated with equations 4.4 and 5.3 for the parameters $\kappa = 30$ MHz, $h = 60$ MHz, and $\Omega = 700$ MHz. The sideband modulation depth is exaggerated for graphical purposes. The high-frequency intensity output of the toroid is proportional to the real portion of the electric field out of the toroid, $Re(a_{out})$, as shown in equation 4.6. Note that this signal is antisymmetric about the bottom of the toroid resonance, unlike the intensity profile, thereby making for a useful error signal. This high-frequency component will be extracted electronically by mixing with a local oscillator and will then be used as an error signal relating the frequency of the laser to the resonance frequency of the toroid.

4.2.2 Electronics

The RF input for the phase modulator is created by either a voltage-controlled oscillator (VCO) or a high-bandwidth function generator, depending on the accuracy necessary for the application. For characterizing toroids, shifts in the phase of the error signal that are caused by RF fluctuations are unimportant and thus an economical VCO can be used as the RF source. Not shown in Figure 4.2 is the voltage source used to control the VCO; we use a simple voltage divider which is adequately stable for characterization, although phase fluctuations are clearly visible as this is not a precision voltage source. For locking purposes, the phase of the error signal is important and therefore either a precision voltage source should be used with the VCO or a high-bandwidth, high-precision function generator should be used. Specifically, if $\Omega \rightarrow \Omega + \pi$ then the $\sin \Omega t$ term in equation 4.6 that is responsible for creating the error signal will change phase, thereby causing the feedback to be out of phase and the system to fall out of lock.

The RF output is split into two portions, with one half driving the phase modulator and the other entering a wideband (1 MHz – 1 GHz) frequency mixer. This RF is mixed with the amplified AC output of the photoreceiver in order to extract the portion of signal that is due to the sidebands and create an error signal. The frequency mixer multiplies the voltage signal from the photoreceiver, $V_{detector} \propto P_{out}$ from equation 4.6, with the RF that was used to create the sidebands, $\sin \Omega' t$:

$$\begin{aligned} V_{mixer} \propto & [\text{DC terms of } P_{out}] * \sin \Omega' t \\ & + 4\sqrt{P_C P_S} Re[a_{out}(\omega)] \sin \Omega t * \sin \Omega' t \end{aligned} \tag{4.7}$$

where

$$\sin \Omega t * \sin \Omega' t = \frac{1}{2}[\cos((\Omega + \Omega')t) - \cos((\Omega - \Omega')t)]. \tag{4.8}$$

Since $\Omega \simeq \Omega'$, low passing of V_{mixer} with a cutoff frequency less than Ω will leave

only the voltage proportional to the amplitude of the AC component of P_{out}, defined here as V'_{mixer}:

$$V'_{mixer} = 2\sqrt{P_C P_S} Re(a_{out}(\omega)). \tag{4.9}$$

Therefore, the low passed output of the mixer, V'_{mixer}, is a voltage whose amplitude is proportional to the real component of the electric field out of the toroid that is shown in blue in Figure 4.3. V'_{mixer} is amplified and can be used as an error signal relating the frequency of the laser to the resonance of the toroid, as displayed in purple in Figure 4.1.

4.2.3 Computer Control

A Labview program controls the characterization process, from the laser scan to the recording and displaying of data from the detectors. Detailed in Appendix B, Section B.2.2, the Labview program, a virtual instrument (VI), allows the user to set such values as the wavelength range for the laser to scan and at what resolution the data will be acquired. The VI communicates with the laser controller via serial port and, through a GUI, the user can set the characterization in progress. Upon execution the laser is scanned over the determined range and the data from the DC output of the toroid, the error signal output from the mixer, and the detector output from the saturation absorption is recorded and displayed. When the toroid is not being characterized, and therefore scanned over a large wavelength range, the laser is scanned over a range of hundreds of MHz in order to probe specific resonances and adjust the coupling between the taper and toroid; this fine scan is controlled by a function generator plugged into the piezo control input on the laser control box. When data is being taken, however, this scan must be stopped in order to avoid confusion from two scans at once. The VI automatically sends a signal to a TTL switch which turns off this fine scan input for the duration of the characterization.

4.2.4 Improved Taper-Toroid Coupling

In order to couple the taper to the toroid in non-contact mode, as detailed in Section 5.1.2, a more precise positioning system than that used in Chapter 2 was necessary. The new positioning system must be able to hold the relative positions of the taper and toroid to less than 100 nm, but also be capable of moving over distances on order of 1 cm. Additionally, the scope of this new coupling system was not only to characterize toroids but also to prototype a new method of coupling for the next vacuum chamber. Therefore, the positioning system must be compatible with pressures as low as 10^{-10} Torr, preferably lower. While such a system was not commercially available at the time of the experiment outlined in Chapter 2 (it was available through special order, but this was time and cost prohibitive as well as untested), in the meantime we located Attocube[4], a company which produces piezo-based positioners that meet all of the above criteria. These positioners use precision voltages applied to piezos in order to obtain the fine motion, and a "slip-stick" motion for the coarse movement. The slip-stick uses a sawtooth shaped voltage, in which the quick voltage change from the steep end of the sawtooth moves the piezo fast enough that it overcomes the force of static friction between it and the piece that we wish to move. The less steep slant of the sawtooth is slow enough that the piezo drags the motion piece. This motion is repeated at relatively high frequencies, allowing speeds of ~ 100 μm/sec or higher. This coarse motion allows us to choose from tens of toroids on a single chip without any resetting of the chip position.

Figure 4.4 shows a model as well as a photograph of this new coupling system. The taper is glued to an aluminum holder which slides into place on an adaptor which is attached to a stack of two positioners. It is very important that the taper be easily installed for two reasons. First, the taper is very delicate and can easily break with excessive motion. Second, and more important, the Attocube positioners are extremely fragile due to the nature of their piezo slip-stick motion; any excessive torque will render them motionless. In order to efficiently couple to a toroid mode

[4]http://attocube.com

the taper must be parallel to the toroid. Since tapers can bend and bow in the pulling process, it is necessary that the tilt of the taper holder be tuned for each new taper. The thickness of the taper must also be matched to the mode of the toroid; since the thickness of the taper varies along the taper's length, this can be controlled by motion along the axis of the taper. Thus these positioners control the tilt of the taper and the position along the taper, y. The chip is mounted with a vacuum-compatible carbon conductive double-sided adhesive disc[5], such as those used in scanning electron microscopes, to a custom-designed aluminum chip holder. This chip holder slides into an aluminum adapter plate and is locked in place with a set screw; this ease of installation is again important in order to avoid damaging the very delicate positioners. This adapter plate is attached to a separate stack of two positioners which control the height of the chip, z, and the horizontal distance between the toroid and taper, x. The x positioner also allows us to select a particular toroid from among the array on the chip. The x and z positioners are the only axes in which fine motion is necessary, as these control the relative separation between the taper and toroid.

This new coupling system not only allows us to couple in non-contact mode, it is stable enough that a resonance will remain coupled without contacting for several minutes or even longer. We have been able to extend this stability to over an hour through implementations of a simple locking scheme as will be discussed in Chapter 6.

[5]At the time of this writing, these are available from http://2spi.com/.

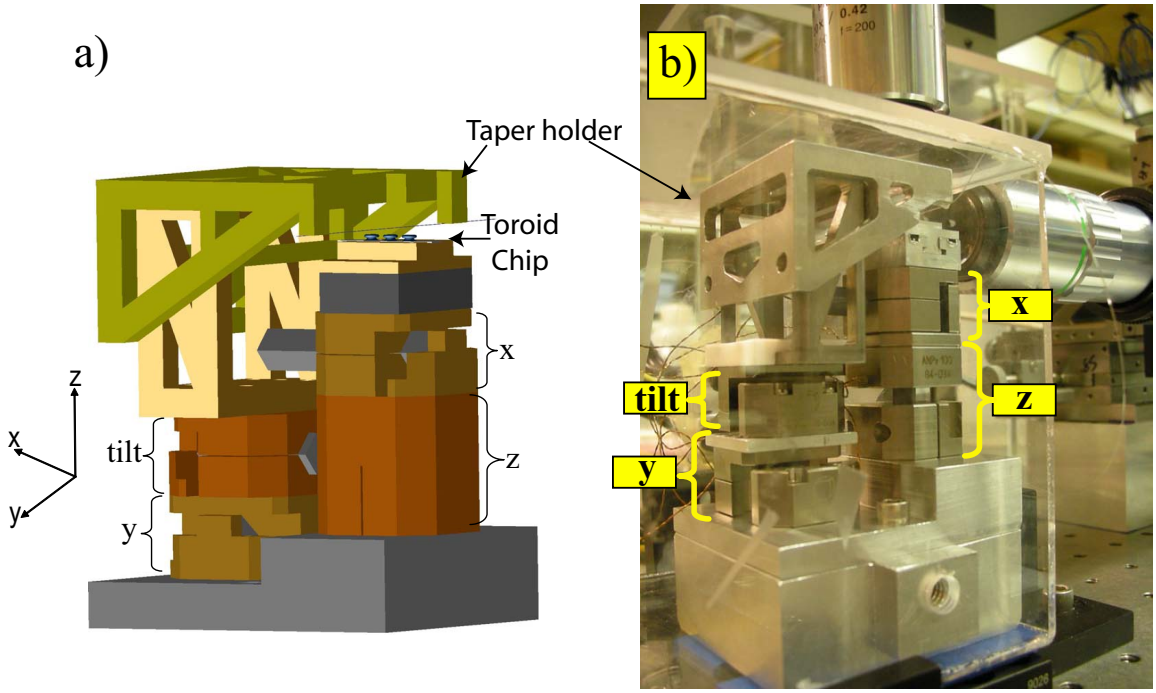

Figure 4.4: An improved positioning system for controlling the relative positions of the taper and toroid. Each axis is able to move coarsely over a range of $\simeq$ 1 cm as well using a slip-stick motion. The piezos in the positioner are also able to move with sub-100 nm resolution, limited by the accuracy of the voltage source. (a) A scale, three-dimensional model of the coupling system. The taper is held on a stack of two positioners which control the tilt of the taper, which allows us to make it parallel to the toroid, and the position along the taper, y, which allows us to control the taper thickness at the location of the toroid. The chip is placed on a separate stack of two positioners which control the height of the chip, z, and the horizontal distance between the toroid and taper, x. The x positioner also allows us to select a particular toroid from among the array on the chip. (b) A photograph of the actual coupling system

Chapter 5

Resonance Behavior as a Function of Coupling Strength

In the process of characterizing toroids the behavior of resonances displayed more complexity than simply a change in depth of toroid mode during a scan in frequency. Presented is a preliminary attempt to take data for a single resonance over a continuum of taper-toroid separations that span the various regimes of coupling.

5.1 Taper-Toroid Coupling

5.1.1 Coupling Regimes

Light is coupled into the toroidal mode via the evanescent field of a tapered fiber. When a fiber is tapered to a diameter that is on the order of one wavelength of light, a significant portion of the traversing field lies outside the physical structure of the fiber as an evanescent wave. Similarly, the toroid is small enough that a portion of its mode also exists as an evanescent wave. When these two evanescent fields overlap, the two waveguides are considered coupled. The degree to which they are coupled is determined by the amount of overlap and is quantified by the rate of external coupling, κ_{ex}, with decreasing taper-toroid separation leading to increased κ_{ex}. Due to the high quality factor given by the low loss rate of the toroid mode, κ_i, the optical power in the cavity builds up by a factor inversely proportional to the external loss rate and,

more importantly, the total internal loss rate squared [1] [18]. Once the optical power in the toroid mode has built up and steady-state is achieved, the output power of the taper P_F exhibits a dip on resonance. This is caused because the light which is coupled into the toroid at rate κ_{ex} is coupled back into the output of the taper, again at a rate κ_{ex}, and destructively interferes with the light in the taper that was never coupled into the mode. The degree of this interference is given by the relative values of the external coupling rate κ_{ex} and the internal loss rate of the cavity, κ_i; this is due to the fact that the total amount of power coupled back into the taper not only depends on κ_{ex} but also on the amount of power in the toroid at the time. Three coupling regimes are defined by how this external coupling rate compares to the rate of internal losses of the toroid, κ_i:

under-coupled	$\kappa_{ex} < \kappa_i$
critically coupled	$\kappa_{ex} = \kappa_i$
over-coupled	$\kappa_{ex} > \kappa_i$

These regimes are shown as a function of resonance depth in Figure 5.1. By resonance depth, the difference between the minimum transmission on resonance and zero is implied and shown explicitly in Figure 5.3. The majority of this chapter will address how this depth and other features of the resonance change as a function of taper-toroid separation.

5.1.2 Experimentally Obtaining Critical Coupling

Of particular interest in our experiment is the regime of critical coupling. It is at this point, when $\kappa_{ex} = \kappa_i$ and transmission drops to zero on resonance, that we are most easily able to observe atoms interacting with our toroid. In Section 2.5.1, the method of critically coupling a taper to a toroid was described for operations where the taper is contacted to the toroid. Here we present a more general method of coupling when the separation between the taper and toroid can be finely controlled.

[1] According to reference [18] section 3.3.3, this power buildup factor is given by $\frac{P_{cav}}{P_{in}} = \frac{c\Delta\lambda_{FSR}}{\lambda^2}\kappa_{ex}\frac{1}{(2\kappa_{ex}+2\kappa_i)^2}$.

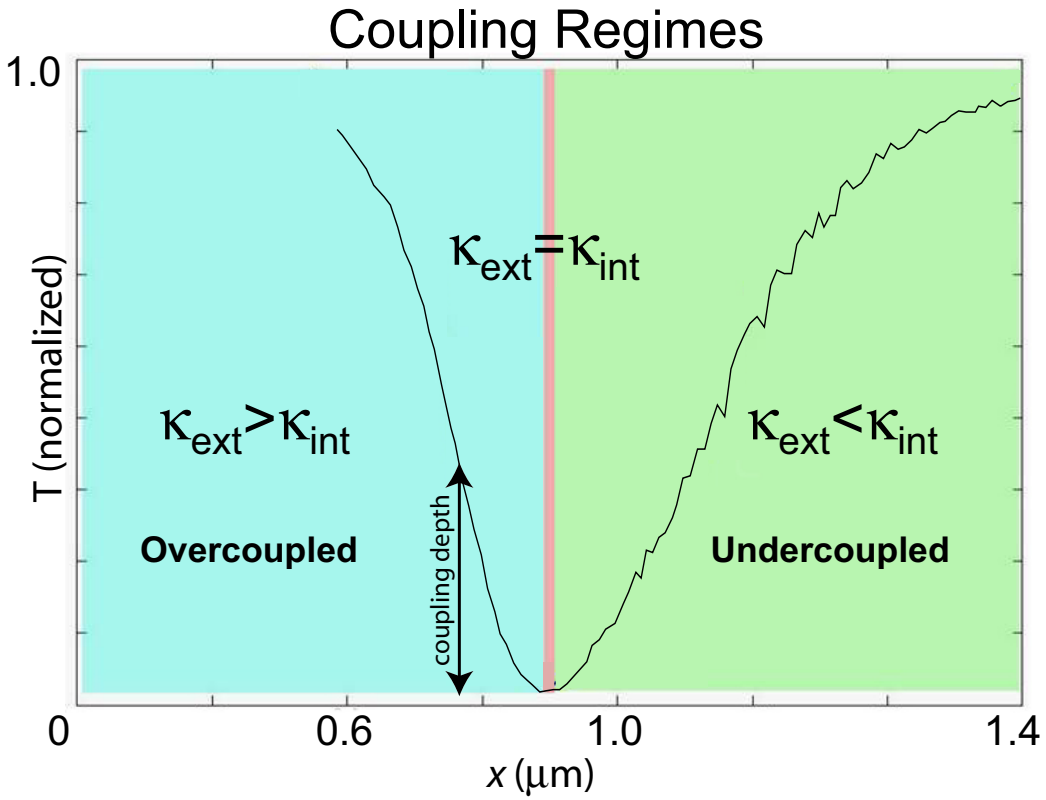

Figure 5.1: The relative value of κ_{ex} compared to κ_i (defined in Figure 2.11) defines to what degree of coupling the toroid is being driven. As the separation between the taper and toroid is reduced, the strength of coupling, κ_{ex}, increases. As this coupling strength increases from $\kappa_{ex} < \kappa_i$ to $\kappa_{ex} > \kappa_i$ the toroid progresses from under-coupled to over-coupled, passing through critical coupling when $\kappa_{ex} = \kappa_i$. Plotted here is actual data of the transmitted light T on resonance as a function of taper-toroid separation x where the far-off resonant value is normalized to one. Of experimental importance (Chapter 2) is the fact that at critical coupling the transmission on resonance drops to near zero.

The first step in coupling is to align the distance between the taper and toroid. Move the taper close enough to the toroid so that the resonance dip is visible. On the imaging system, provided IR light is not filtered, the mode of the toroid should be visibly excited, as shown in Figure 5.2. Move the taper away until the excitation is just barely visible and adjust the height of the taper relative to the toroid in order to maximize the glow. While maximizing this excitation, continue to move the taper away from the toroid in order to avoid accidentally contacting the taper to the toroid. Once the proper height is determined, walk the polarization by scanning the quarter waveplate while walking the half waveplate until the dip in transmission is at its deepest point, such as that shown in purple in Figure 2.3. As the taper moves closer, the resonance deepens as critical coupling is approached; after this point, in the over-coupled regime, the resonance will begin to broaden and become shallower. Adjust the taper separation until the resonance is at this deepest point

In order to obtain efficient transfer of light between the mode of the taper and toroid, losses to other modes must be minimized [41]. This mode matching is achieved by tuning the geometries of the respective waveguides. Since the minor diameter of the toroid is determined during the manufacture, the taper diameter must be matched to the toroid. Due to the nature of a taper, the diameter of the fiber changes as one moves along its length. It is precisely this gradual change in taper thickness that we exploit in order to match the mode of the toroid. The proper thickness can be determined by again minimizing the depth of the resonance dip. Move along the taper in one direction to see if the resonance tends closer to zero; if it does not seem better matched, then move the taper in the other direction. Continue this iteration until the desired level of darkness is achieved.

5.1.3 Modal Coupling

One particular feature of whispering gallery mode resonators (such as toroids) that distinguishes them from the more typical Fabry-Perot resonator is modal coupling [63]. Scatterers in the mode of the resonator will preferentially scatter light circulating

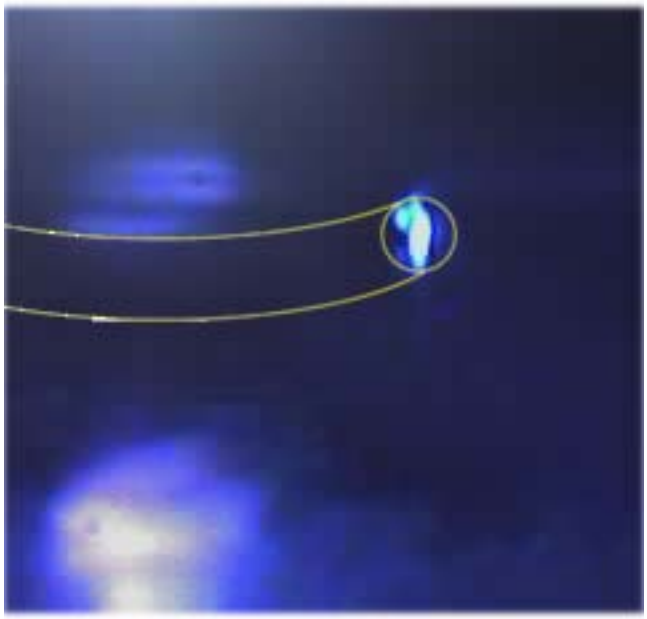

Figure 5.2: Screen shot of an excited toroidal mode. To compensate for the imaging system being focused on the mode, a partial outline of the toroidal structure has been highlighted in yellow. We can use the relative strength of this excitation to position the taper in the ideal location for exciting a particular toroidal mode.

in a clockwise manner, a, at a rate "h" back in a counterclockwise direction, b. These two traveling waves interfere to produce two standing waves $A = \frac{a+b}{\sqrt{2}}$ and $B = \frac{a-b}{\sqrt{2}}$, where A represents the symmetric and antisymmetric modes of this interference, separated in frequency by the amount h. This splitting of modes is visible in the experimentally obtained trace in Figure 5.3. This modal coupling changes the physics of the interaction between an atom and the toroid. As described in detail in reference [19], the atom can only interact with one mode at a time, leaving the other mode untouched, thus reducing our transit signal. Additionally, this splitting broadens a critically coupled resonance by being an additional loss rate which must be added in quadrature.

Following the derivation presented in reference [64], the symmetric and antisymmetric modes inside the toroid are given by

$$A_{ss} = -\frac{i}{\sqrt{2}} * \frac{\varepsilon_a + \varepsilon_b}{\kappa + i(\Delta_C + h)} \tag{5.1}$$

and

$$B_{ss} = -\frac{i}{\sqrt{2}} * \frac{\varepsilon_a - \varepsilon_b}{\kappa + i(\Delta_C - h)} \tag{5.2}$$

where $\kappa = \kappa_{ex} + \kappa_i$ is the total decay rate for the cavity modes, with κ_{ex} and κ_i as the external coupling and intrinsic loss rates of the cavity, respectively. Δ_C is the frequency detuning of the laser from the cavities resonance and h is the coupling rate between the clockwise and counterclockwise traveling waves in the resonator. Experimentally, we are unable to observe the modes inside the cavity directly. Rather, we monitor the "forward" and "backward" transmissions out of the taper. Here, forward is defined as the direction the light travels in the fiber in the absence of a toroid and backward is the opposite direction. The field out of the toroid in the forward direction is given by (where the light is input in the clockwise direction)

$$\begin{aligned} a_{out} &= \text{input field} + \text{clockwise field out of toroid} \\ a_{out} &= \frac{i\varepsilon_a}{\sqrt{2\kappa_{ex}}} + \sqrt{\kappa_{ex}}(A + B) \end{aligned} \tag{5.3}$$

Similarly, the field out of the toroid in the backward direction is given by

$$\begin{aligned} b_{out} &= \text{input field} + \text{counterclockwise field out of toroid} \\ b_{out} &= \frac{i\varepsilon_a}{\sqrt{2\kappa_{ex}}} + \sqrt{\kappa_{ex}}(A - B) \end{aligned} \tag{5.4}$$

However, we observe the intensity experimentally. The normalized intensities for the forward and backward directions are given by

$$I_F = \frac{|a_{out}|^2}{\frac{|\varepsilon_a|^2}{2\kappa_{ex}}} \quad \text{and} \quad I_B = \frac{|b_{out}|^2}{\frac{|\varepsilon_a|^2}{2\kappa_{ex}}}. \tag{5.5}$$

The experiments described in this thesis are all driven only in one direction, giving $\varepsilon_a \neq 0$ and $\varepsilon_b = 0$.

5.2 Resonance Behavior as a Function of Taper-Toroid Separation

This section explores the behavior of a single toroidal resonance as the distance between the taper and toroid is varied. Data from the forward output of a coupled toroid is taken over the range of coupling strengths, κ_{ex}, and fit to the theory outlined in Section 5.1.3.

5.2.1 Observations [2]

As we change the degree of coupling between the taper and toroid modes we observe changes in characteristics of the resonance line shape. Figure 5.3 shows data taken from the output of the taper P_F when under-coupled to a toroid resonance as the laser frequency is scanned over an adequate range. The figure labels the various parameters used to quantify a given resonance in the following discussion. The full width at half maximum of each dip is given by the intrinsic loss rate of the mode, κ_i, combined in quadrature with the rate of external coupling, κ_{ex}, which is dictated by the mode overlap between the taper and toroid. This width is denoted for the left and right dips by κ_{left} and κ_{right}, respectively. This total width is given by the sum of the squares of the intrinsic and external rates, namely $\kappa_{left} = \sqrt{(\kappa_{i\ left})^2 + (\kappa_{ex})^2}$, similarly for the Lorentzian to the right. The amount of transmission P_F above zero at the bottom of each dip is given by the "coupling depth." Additionally, as the amount of coupling

[2] Daniel Alton contributed significantly to the taking of data presented in this section.

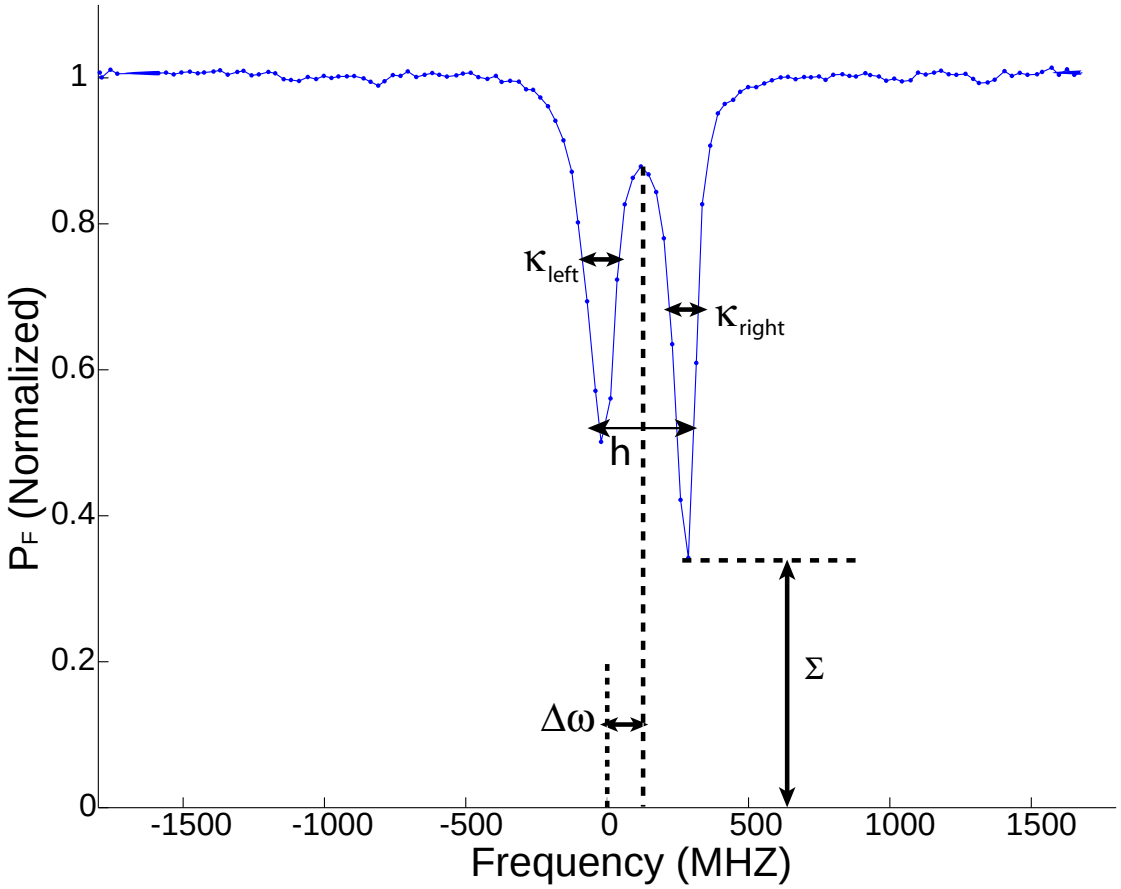

Figure 5.3: Data from a typical resonance is shown here, under-coupled and exhibiting splitting caused by the interference of two counter-propagating traveling waves in the resonator. The attributes used for characterizing are labeled. The degree to which the counter-propagating modes are coupled is evident in the amount of splitting of the resonance, denoted here by the value h. The width of each of these dips, κ_{left} and κ_{right}, result from the intrinsic linewidth of each mode defined from internal losses, $\kappa_{i\ right}$ and $\kappa_{i\ left}$, and the rate of external coupling, κ_{ex}, added in quadrature. As κ_{ex} is increased (taper-toroid separation is decreased), the entire resonance shifts by an amount $\Delta\omega$ and the coupling depth Σ changes in the manner shown in Figures 5.1 and 5.4.

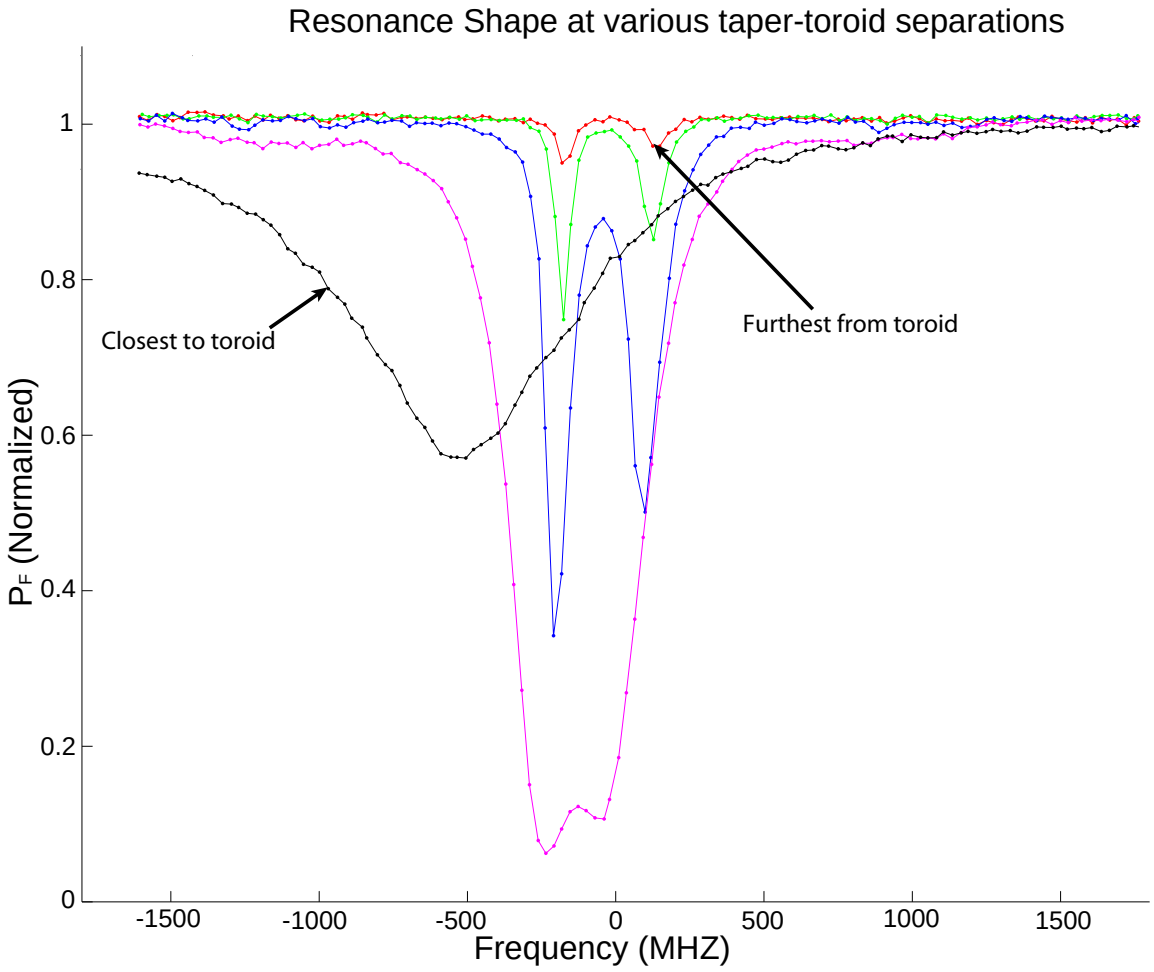

Figure 5.4: Shown here is the data from the spectra of one resonance for different taper-toroid separations. The red trace is when the taper is furthest away from the toroid, the black trace is closest, and green, blue, and pink are in between. Note that as the separation decreases, the resonance widens, shifts, and the two modes mesh into one. The depth also increases as critical coupling is approached, and then recesses as the over-coupling is entered.

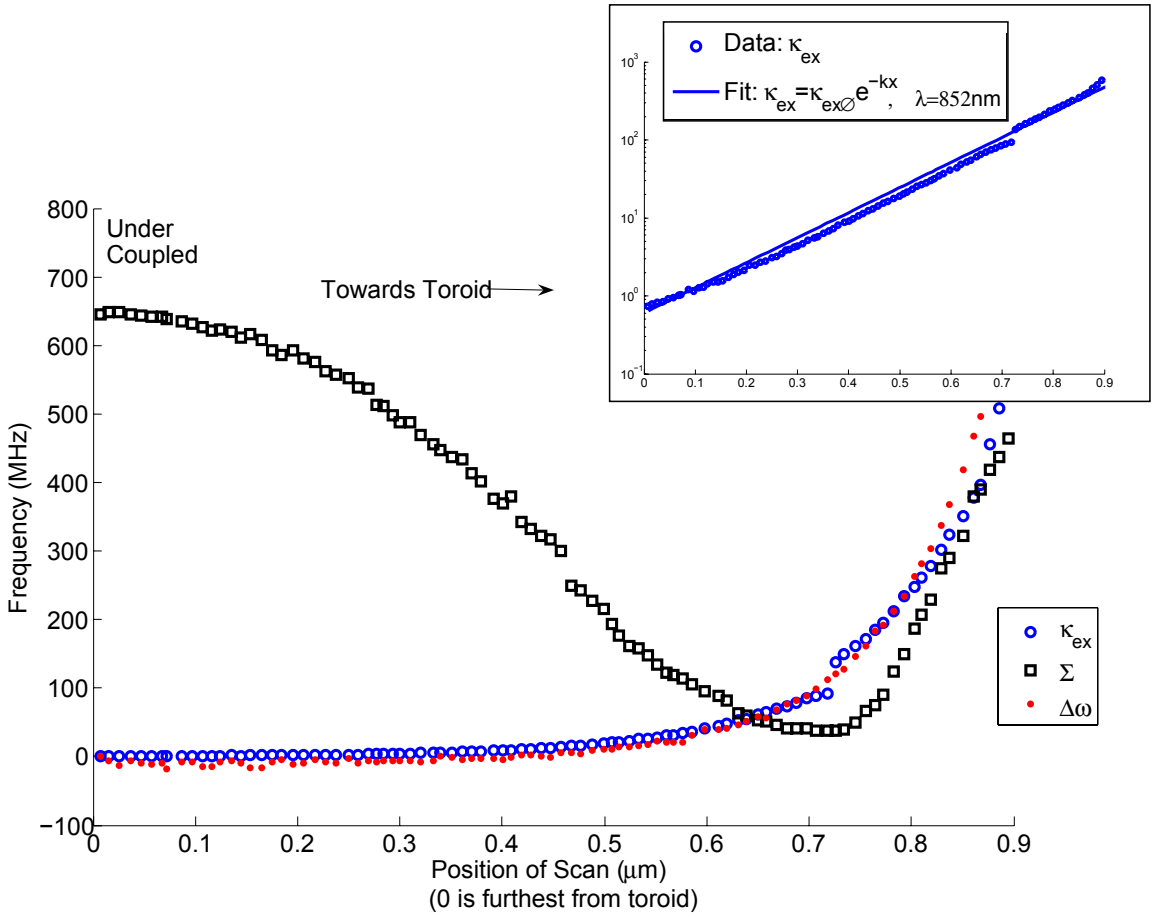

Figure 5.5: Plotted here are the parameters for our resonance at various separations between the taper and toroid found by fitting the data to the theory outlined in Section 5.1.3. The intrinsic linewidth κ_i was measured to be 45 MHz, and the splitting h to be 120 MHz. As the distance between the taper and toroid decreases, the external coupling rate increases as $\kappa_{ex} = \kappa_{ex0}e^{-kx}$, where $k = \frac{2\pi}{\lambda}$ for $\lambda = 852$ nm and κ_{ex0} is the coupling strength at the nearest approach and x is the distance from the surface of the toroid. The inset shows the $\kappa_e xt(x)$ data along with the exponential fit $\kappa_{ex} = \kappa_{ex0}e^{-kx}$ on a semi-log scale. The magnitude of the shift in resonance frequency, $|\Delta\omega|$ is plotted since these shifts are all to negative frequencies, as denoted in Figure 5.4. For reference, also shown is the minimum of power transmitted on resonance, Σ, as defined in Figure 5.1. (Note that the y axis of Σ does not correlate to frequency but rather transmission, where $\Sigma(\kappa_{ex} = 0)$ is normalized to one) In taking data, we were limited in our distance of nearest approach between the taper and toroid and were unable to reach total over-coupling. Therefore, the minimum transmission Σ does not return to unity for over-coupling in this plot. Also note that the horizontal axis plots the "position of scan," or displacement, in micrometers, where 0 μm is furthest and 1 μm is the closest to the toroid. This scale was chosen due to the lack of precision in our knowledge of absolute distance from the taper to the toroid; however, we are able to know the relative distance that the toroid has moved from our positioning system.

changes the resonance shifts in frequency by an amount $\Delta\omega$. Finally, as previously described, the distance between the two dips "h" is the rate of scattering into the counter-propagating mode.

Figure 5.4 again shows the output P_F as a function of laser frequency for a taper coupled to a toroid, as in Figure 5.3. However, each trace is taken for the same resonance but with a different separation, and hence a different degree of modal coupling, between the taper and toroid. As the distance between the taper and toroid decreases and κ_{ex} increases with respect to κ_i, the coupling moves from under-coupled through critically coupled to over-coupled, as described in Section 5.1.1, and the shape of the spectrum changes accordingly.

When the taper is furthest away and the toroid is therefore under-coupled, shown here in the red trace, the dips are shallow, leading to a large "coupling depth" as defined in Figure 5.3. This is also made apparent in Figure 5.1 by the data found in the light-green under-coupled region, when the taper-toroid separation is large; here the coupling depth is at a maximum. Also notable is that the linewidths, κ_{left} and κ_{right}, are at their narrowest values. This is because κ_{ex} is very small, causing κ_{left} and κ_{right} to be essentially equal to their respective intrinsic loss rates, κ_i. As the distance between the taper and toroid decreases (as shown in the green and blue traces of Figure 5.4), κ_{ex} increases and the resonance dips become deeper and wider. This agrees with Figure 5.1 in that the coupling depth decreases as the taper-toroid separation decreases from under-coupled toward critically coupled. The deepest line shape shown here in pink is given by a resonance that is nearly critically coupled. Not only are the dips very deep — nearly to zero — but they are becoming wide to the point where resolving the left and right dips individually grows difficult. At the point of critical coupling, as shown in Figure 2.2, the dips will drop all the way to zero and appear as one — rather than two — Lorentzians. The shift in frequency becomes more apparent at this point as the resonance frequency is red shifted from the under-coupled value. Finally, once the coupling reaches the regime of over-coupled, the two Lorentzians are no longer distinguishable, the overall full width at half maximum is much broader than when under-coupled, and the entire resonance is severely red

shifted. When measurements of the intrinsic linewidths $\kappa_{i\ left}$ and $\kappa_{i\ right}$ or the splitting h are desired, one must operate as far under-coupled as possible in order to prevent the external coupling from dominating the spectrum.

5.2.2 Data Fitting to Coupled Mode Theory

In order to quantify the behavior of the parameters κ_{ex}, h, and $\Delta\omega$ as a function of taper-toroid separation, the spectrum of a resonance was recorded and the data was fitted to the theory presented in Section 5.1.3. Specifically, a probe laser was injected into the tapered fiber which was coupled to a toroid resonance. The frequency of the probe was scanned over a range of $\simeq 3GHz$ with a center frequency ω_0 equal to the resonance frequency ω_c. The forward going optical power was measured on a photodetector with the output voltage recorded by a data acquisition card. The distance between the taper and toroid is scanned in order to vary the coupling rate κ_{ex}. The position scan rate is much slower than the frequency scan, allowing us to make the approximation that the taper-toroid separation, and hence κ_{ex}, is constant over each frequency scan cycle. The data-taking procedure is detailed in Section 5.2.3.

The resonance data for each frequency scan is then fit to equation 5.5 in order to determine κ_{ex}, h, and Δ_C. $\Delta\omega$ is determined from $\Delta_C = \omega_p - \omega_c$, where ω_p is the frequency of the probe and ω_c is the cavity resonance frequency. ω_c is calculated for each value of κ_{ex} and $\Delta\omega(\kappa_{ex}) = \omega_c(\kappa_{ex}) - \omega_c(\kappa_{ex} = 0)$ where $\kappa_{ex} = 0$ occurs when the coupling between the taper and toroid is minimal. The intrinsic loss rate $\kappa_i = 45$ MHz was found by fitting equation 5.5 to a minimally coupled resonance. While the intrinsic loss rates between the two modes $\kappa_{i\ right}$ and $\kappa_{i\ left}$ can be different due to the fact that these modes are spatially out of phase [19], and hence see different surface imperfections [63], for this calculation they were taken to be the equal, $\kappa_{i\ right} = \kappa_{i\ right} = \kappa_i$. The Matlab code used for this fit is available in Appendix B

The calculated values are presented in Figure 5.5 as a function of taper-toroid separation. In this plot, the horizontal axis is the relative displacement between the taper and toroid, with zero being the position of the taper that is furthest from the

toroid (i.e., extremely under-coupled) rather than the absolute separation. This is chosen to be the zero value because: a) the absolute separation between the taper and toroid is not known (only the change in relative position is known), and b) the scan begins away from the toroid.

As shown in the inset of Figure 5.5, the data for κ_{ex} can be fit to an exponential of the form $\kappa_{ex} = \kappa_{ex0}e^{-kx}$, where k is the wavenumber $k = \frac{2\pi}{\lambda}$ for the laser wavelength $\lambda = 852$ nm, κ_{ex0} is the coupling strength at the point of nearest approach for the taper relative to the toroid, and x is the distance from the surface of the toroid. This is consistent with our expectation since the fields outside the taper and toroid are both evanescent and therefore decay as $\sim e^{-kx}$. Due to experimental limitations, we are unable to determine more than a lower bound of 600 MHz for κ_{ex0}. Our measurement of taper-toroid separation was relative to an arbitrary start position and not to the toroid itself.

Interesting behavior is observed in the shift in resonance frequency, $\Delta\omega$, which is red shifted as the taper approaches the toroid. The presence of the taper waveguide increases the amount of silica that the light in the mode of the toroid must traverse, thereby increasing its effective propagation constant. This can be compared to the classical model of a damped driven harmonic oscillator [65] in which the resonance frequency shifts according to the level of damping present in the system. In this situation the damping term is quite small as the proportional shift in frequency $\frac{\Delta\nu}{\nu}$ is $\sim$ 1x10^{-6}, which is consistent with the theory presented in reference [65] over the $\simeq 1$ μm we are moving the taper relative to the toroid.

As a first-order approximation we would like to determine whether the the shift in the effective propagation constant would be proportional to the fraction of the toroid's evanescent field traversing the tapered fiber, defined here to be E_{taper}. In order to determine E_{taper}, the evanescent field of the toroid was integrated over the volume of the tapered fiber for various taper-toroid separations. The external field of the toroid is taken to have an amplitude proportional to e^{-kr}, where $k = \frac{2\pi}{\lambda}$ is the wavenumber for $\lambda = 852$ nm and r is the distance from the surface of the toroid, shown qualitatively in Figure 5.6a.

Figure 5.6b shows E_{taper} compared to the measured values for $\Delta\omega$ versus the distance over which the toroid has scanned. This scan distance is relative to the starting separation of the position scan, with 0 meaning the taper is furthest from the toroid. Given that the intent of this calculation is to determine how E_{taper} varies as a function of taper-toroid separation, rather than to predict absolute frequency shifts, E_{taper} is normalized to have the same maximum value as the data. For larger taper-toroid separations (smaller scan distances) E_{taper} fits well with the data. However, when the separation between the taper and toroid becomes very small the calculated shift departs from the measured shift. This is thought to be due to the van der Waals force, which becomes significant for small separations. At this point the actual separation between the taper and toroid is smaller than the translation stage displays due to the two surfaces being attracted together, thereby compressing the shift data versus distance. This hypothesis that the taper is being pulled closer to the toroid by the van der Waals force is observed experimentally as the taper abruptly jumps into contact with the toroid for separations slightly smaller than those presented here. Once contacted the taper must be pulled far away from the toroid before the taper is released from the toroid surface.

5.2.3 Data-Taking Procedure

Sweeping of frequency and position— In order to determine the behavior of a resonance as a function of coupling strength, the taper-toroid separation must be scanned over a range large enough to encompass all regimes of coupling. The rate at which this scan occurs must exceed any drift in the system; since we are only scanning the x axis, as defined in Figure 2.11, the relative height of the taper relative to the toroid will drift over time (as it is not locked). This drift causes a change in necessary polarization since the orientation of the toroid mode relative to the taper, and hence light, changes. However, since we are also scanning the frequency of the laser over the range of the resonance, this scan must be slow enough so that the taper-toroid separation is essentially constant over one sweep of the frequency. Therefore,

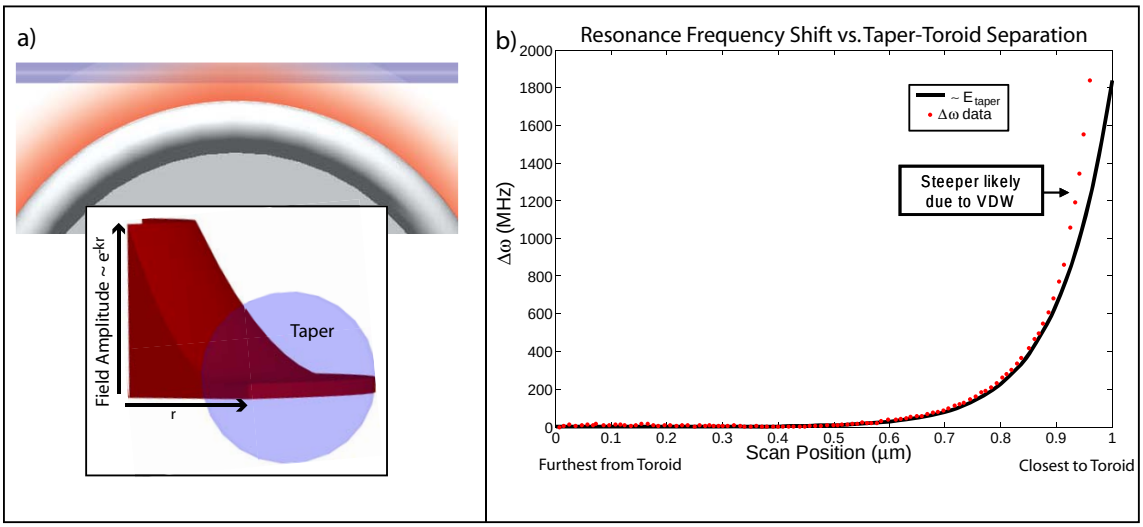

Figure 5.6: In order to determine if, to first-order approximation, the shift in the toroid's resonance frequency is due to the presence of the taper, the $\Delta\omega$ is compared to the percentage of the toroid's field encompassing the tapered fiber, E_{taper}, as a function of taper-toroid separation, d. a) The exponentially decaying evanescent field from the toroid overlaps with the tapered fiber. The amplitude of the field is integrated over the extent of the tapered fiber to determine E_{taper} for various taper-toroid separations. b) The measured frequency shift $\Delta\omega$ (red dots) is plotted with the normalized E_{taper} (black line). Note that the distance plotted on the x axis is relative to the starting separation of the position scan, with 0 meaning the taper is furthest from the toroid. The intent of the calculation is to determine how E_{taper} varies as a function of taper-toroid separation, rather than to predict absolute frequency shifts, therefore E_{taper} is normalized to have the same maximum value as the data. Note that the data fits well with E_{taper} until the separation between the taper and toroid becomes very small and van der Waals forces become significant. At this point the actual separation between the taper and toroid is smaller than the translation stage reads, due to the two surfaces being attracted together, thereby compressing the shift data versus distance.

we sweep our laser frequency at a rate of 30 Hz and the position at $< \frac{1}{2}$ Hz. The frequency sweep of the laser is accomplished by plugging the triangle output of a function generator into the piezo scan input of the laser control box. The position of the toroid is swept by sweeping the position of the Attocube positioner upon which the toroid chip is mounted. A triangle signal, generated by the data acquisition card in the computer, is connected to the external voltage input of the control box for the positioner; this external voltage input allows an arbitrary waveform to control the motion of the Attocube. Both of these signals are acquired concurrently with the output of the photodetector to which the output of the taper is connected.

Representative data— A representative data acquisition is shown in Figure 5.7 with output of the taper, P_F, in blue, the frequency sweep of the probe laser in green, and the red being the function which sweeps the position of the toroid relative to the taper. The inset shows a few cycles of the laser frequency sweep; note that the position driving function is effectively constant over this time segment, ensuring that the coupling does not change appreciably during one cycle of the frequency sweep. The output of the taper is recorded with resolution of 8000 points per position sweep, corresponding to ~ 100 points per frequency sweep. Data with a resolution of 80,000 points per position sweep was also acquired. However, while the calculations were much more intensive and time consuming for the computer, the results were effectively the same. Therefore, the 8k data was used for the presented analysis.

In order to acquire data as shown in Figure 5.7, a resonance is located by the methods described in Chapter 4 and coupled to the fiber taper. The frequency of the laser is adjusted so that it is sweeping across the resonance with a range that is several times the resonance linewidth. The taper is moved just far enough away from the toroid so that the resonance is no longer visible on the signal P_F. The position is then swept, using the signal generated by the computer, over the entire accessible coupling range of the resonance; the range is adjusted until the entire range of coupling regimes is visible, going as close as possible into the overcoupled regime without contacting the taper and toroid.

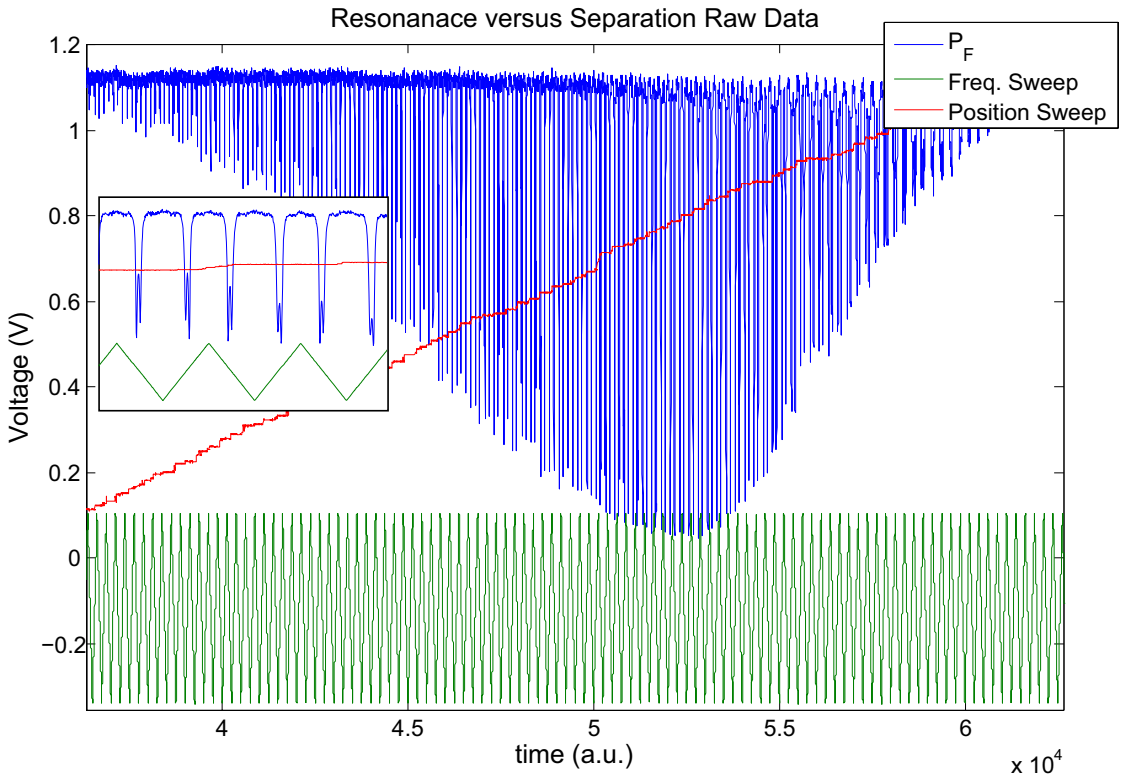

Figure 5.7: Shown is an example of the raw data taken during one sweep of the separation between the taper and toroid. The horizontal axis is time in arbitrary units that are dependent on the sampling rate of data acquisition, the vertical axis is voltage as read by the data acquisition card in the computer. The blue trace is the output of the taper, P_F, the green is the function which sweeps the frequency of the probe laser, and the red is the function which sweeps the position of the toroid relative to the taper. The inset shows a few cycles of the frequency; note that the position is effectively constant during each cycle of frequency sweep, ensuring that the coupling does not change appreciably as the frequency is swept.

Calibration— After this data has been taken, the frequency is calibrated by scanning with the same frequency range over the D2 lines of cesium in a saturation absorption setup (described in Section 4.1). In order to accomplish this calibration, the settings on the function generator remain untouched, while the center frequency of the laser is shifted to the wavelength of cesium manually on the control box. The scan is then acquired along with the data from the detector in the saturation absorption setup and used to convert a given number of data points (essentially time) into an absolute frequency difference.

In order to convert the voltage of the position scan of the Attocube positioner into distance, the positioners were calibrated using a diffraction grating of 1200 lines/mm. The grating was imaged with a microscope and the positioners were given an input of 100 V. The position difference was measured relative to the line spacing of the grating for a conversion factor of 6.8 μm per 100 Volts.

5.2.4 Fitting Procedure

The data was parsed and analyzed using Matlab; the code is presented in Appendix B and outlined below.

Data sorting— The data files from each of the ten runs of the experiment are each separated into full, single scans of position and saved as one master data file; the data file contains all three signals that are shown in Figure 5.7. The data from each run is then divided into single-frequency scans and sorted by taper-toroid distance. Finally, the different runs for each distance are averaged together.

The cesium reference detector output and sweep data are also separated into single, full sweeps of the laser frequency. The cesium reference is plotted and the user manually inputs the distance between the transition being used for the calibration. This value is used throughout the analysis in order to convert number of points into frequency difference.

Chapter 6

Locking of Taper-Toroid Separation

In our experiment it is important to be able to maintain a constant degree of coupling, typically critical coupling, for an extended period of time. In an experiment such as described in Chapter 2, hundreds of runs of the experiment were required to obtain enough data in order to determine the strength of coupling between an atom and the resonator. In that version of the experiment, the taper was contacted to the toroid in order to have constant coupling for a long enough time to take this amount of data. However, in next generations of this experiment, a goal is for the taper to be coupled to the resonator — without contacting — for the reasons detailed in Section 4.2.4. The distance between the taper and toroid needs to be locked in order to maintain this non-contact coupling for an appreciable length of time and to suppress vibrations that will convolute the small signal produced by single atoms.

Presented in this chapter are results from a preliminary locking scheme, implemented on the apparatus introduced in Chapter 4, that reduces slow drift in the taper-toroid separation by over 40 dB. By isolating the coupling apparatus from the environment we have reduced the noise floor by as much as 60 dB. Using a simple PID locking system, the low frequency component of the taper-toroid separation has remained locked for over one hour. Daniel Alton contributed significantly to the implementation and quantification of noise quantification and reduction presented in this chapter.

6.1 Minimizing Background Noise

6.1.1 Measurement Procedure

This data was taken, without locking, by monitoring the output of the fiber taper, P_F, while it was coupled to the minimum of a resonance. Since we are only interested in noise caused by relative motion between the taper and toroid, the resonance used in this quantification was very broad, several GHz. This minimizes noise contributions from frequency noise in the laser as well as temperature fluctuations in the toroid that, as discussed in Section 2.3.3, shift the resonance frequencies. Relative motion between the taper and toroid will be manifest in a change in κ_{ex}, which in turn changes the resonance spectrum, as shown in Figure 5.4. A change in κ_{ex} corresponds to a change in Σ, as evident in Figure 5.5. The probe frequency is set such that the power exiting the toroid in the forward direction, P_F, is minimized, thus ensuring that $\omega_p = \omega_c$ and $P_F \propto \Sigma$. Therefore, changes in the relative taper-toroid separation will be manifest in changes in P_F

P_F is detected on a photodetector with a bandwidth of 1 GHz. The output of the photodetector, $V_{detector}$, is broken into its frequency components by taking the fast Fourier transform (FFT) on a network analyzer. The FFT signal obtained is $FFT_{detector} = 10log(\frac{P_{detector}}{P_{ref}})$ where $P_{detector} \propto V^2_{detector}$ and P_{ref} is the reference of the network analyzer. The signal from the photodetector, $P_{detector} = P_\Sigma + P_{background}$, consists of the signal due to the variance in taper-toroid separation, P_Σ, as well as the signal from other noise sources, $P_{background}$. In the case of $P_{background} >> P_\Sigma$, P_Σ will be difficult to discern. In order to quantify $P_{background}$, the FFT is taken when the taper is far away from the toroid in order to obtain the signal $FFT_{background} = 10log(\frac{P_{background}}{P_{ref}})$. It can be shown that

$$10log(P_\Sigma) = log(10^{FFT_{detector}} - 10^{FFT_{background}}). \tag{6.1}$$

This subtraction allows us to isolate P_Σ from the background noise and therefore

quantify changes in noise for various experimental configurations.

6.1.2 Floated Table

Prior to locking the separation between the taper and toroid, environmental noise needed to be minimized. The apparatus was initially built upon a breadboard that was set upon a standard table (not an optical table). As shown in Figure 6.1, after moving the experiment onto a floated optical table, the noise floor was lowered by as much as 60 dB over the frequency range of 30 – 500 Hz; no appreciable improvement was seen over the remainder of frequencies in the 1 Hz – 1 kHz range tested.

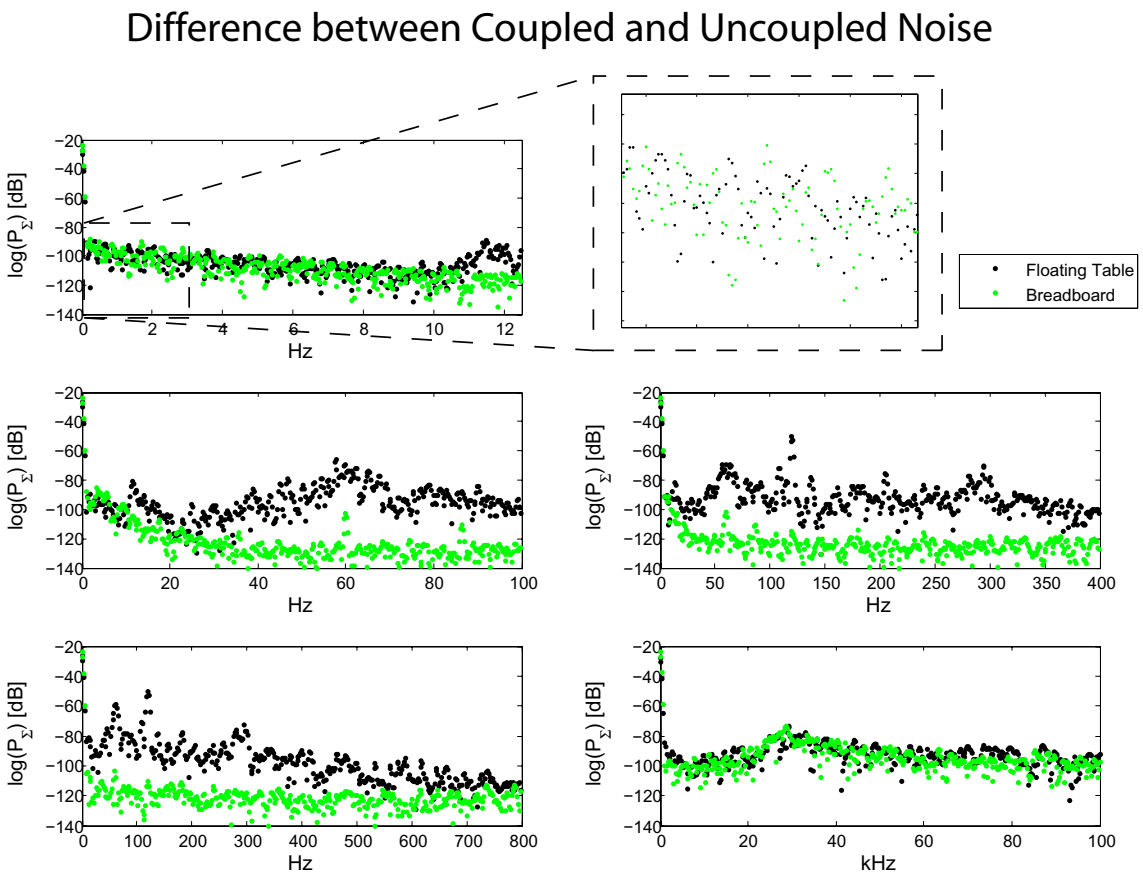

Figure 6.1: $log(P_\Sigma)$ is plotted for two scenarios. First, represented by green squares, the apparatus is mounted on a breadboard and second, shown in black dots, the apparatus is mounted on a floated optical table. There is significant noise suppression of up to 60 dB for frequencies of $\simeq 30 - -500Hz$, while the inset shows no significant suppression for very low frequencies. However, the large improvement at higher frequencies when the apparatus is mounted to a floating optical table will greatly improve the stability of non-contact coupling.

6.1.3 Isolation from Table

In an effort to further isolate the coupling apparatus from environmental noise we mounted the apparatus on three pieces of soft, cured silicone sealant. In order to better characterize the noise in the coupling for each of these scenarios, an improved version of the technique used in Section 6.1.1 was used. Rather than taking the Fourier transform of the photodetector output directly, improved signal-to-noise was achieved by using the error signal that was implemented in Chapter 4 and defined by equation 4.9 as $V'_{mixer} = 2\sqrt{P_C P_S} Re(a_{out}(\omega))$. On critical coupling, the change in DC output of the photodetector $\delta V_{detector} \propto \delta a_{out}(\omega, \kappa_{ex})$ for small changes in κ_{ex} is very small. As can be seen in Figure 4.1c and d, as well as in Figure 4.3, the slope of the error signal is much steeper than the DC output of the detector, thus enhancing the signal due to changes in coupling. This error signal is then sent to a network analyzer that takes its Fourier transform. Data is taken, for each isolation scheme, both when the taper is critically coupled to the toroid and when the taper is far away from the toroid. The difference between these is presented in Figure 6.1.3.

The apparatus was initially set upon the sealant with no support from the sides, providing the best isolation from the table, as it is effectively floating with minimal contact. As shown in Figure 6.2, this configuration yields the best noise improvement. However, it soon became apparent that the slow drift of the sealant — which is responsible for much of the noise improvement because it is very soft and therefore dampens high-frequency noise — affects the polarization of light in the fiber. When the apparatus — including the tapered fiber — drifts relative to the fixed length of fiber that leads to the taper, the resulting mechanical stress changes the birefringence in the fiber, causing the polarization to change. Therefore a slow drift in the position of the apparatus causes a slow drift in the light polarization coupled into the toroid, in effect causing the degree of coupling to drift. While polarization-maintaining (PM) fiber would eliminate this drift, non-PM fiber must be used in fabrication of the tapers since arbitrary polarizations are needed when coupling light into the toroid; light coupled into PM fiber must be aligned to an axis of the fiber and therefore cannot

be tuned arbitrarily as needed. An additional problem caused by the slow drift of the apparatus is the change in the relative position of the toroid and the fixed imaging system. Since the toroids are $\simeq 30$ μm in diameter, a drift of one millimeter (although it typically drifts by more than a centimeter) is enough to require realignment of the imaging system — a tedious process that disrupts the experiment. Therefore, support from sides was installed in order to suppress this slow position drift. Silicone balls attached to L-brackets and pressed to the four sides of the apparatus accomplished this suppression. While this configuration still results in a vast improvement over the noise in the signal when the apparatus was mounted directly to the table, the noise floor is 5 – 10 dB higher than when the silicone is only on the bottom. However, the stability achieved in the polarization and imaging justifies this compensation.

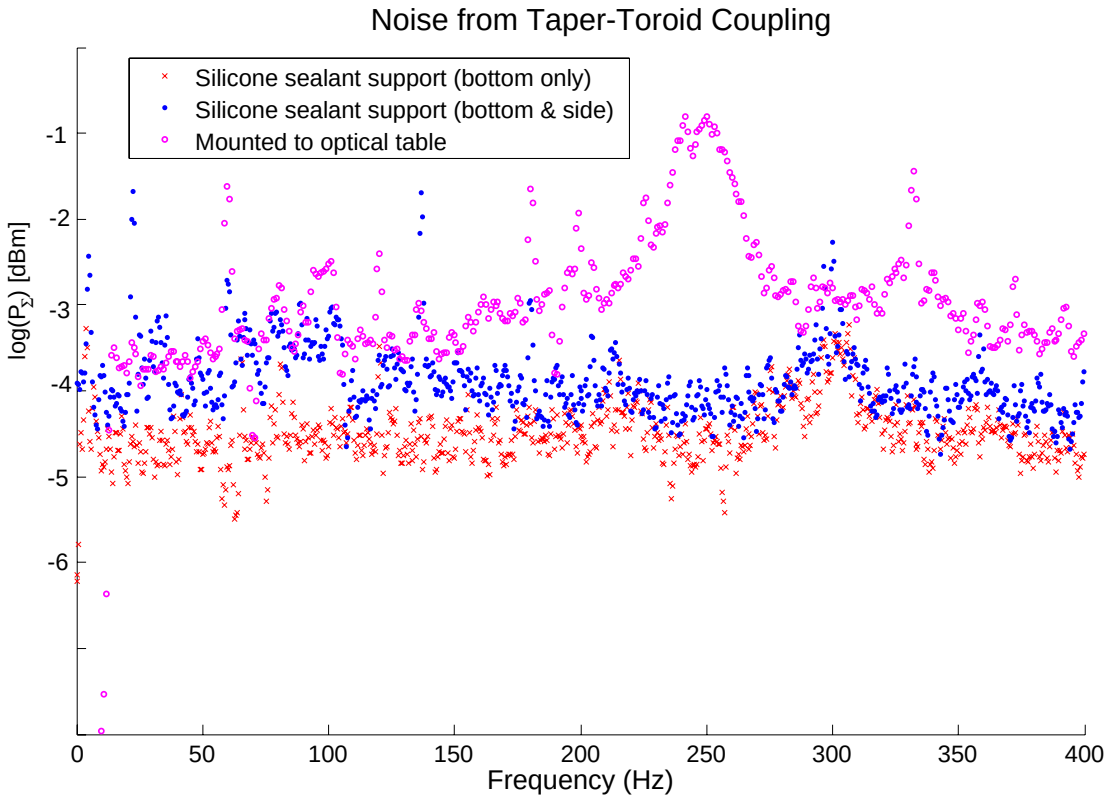

Figure 6.2: In order to further suppress noise from the external environment the apparatus was mounted atop silicone sealant rather than directly to the optical table. Three scenarios were tested and are presented here: mounted directly to floated optical table (pink open circles), set on silicone sealant with no side support (red x's), and silicone sealant not only below but also from the side (blue dots). Data was acquired in a similar manner as in Section 6.1.2, but using the error signal (Section 4.1) rather than the DC output from the taper as the signal into the network analyzer. Improvement of up to 30 dB is evident for both cases of silicone sealant over the apparatus being mounted directly to the table. While the apparatus is more decoupled from the environment when mounted on sealant only from below, leading to lower noise for all frequencies — particularly those below 100 Hz — we ultimately used the silicone support on the sides as well as below. This additional support is necessary for stability in polarization of the light in the fiber as well as for maintaining a constant position of the apparatus relative to the imaging system.

6.2 Locking

6.2.1 Locking Laser to Toroid Resonance

When the separation between the taper and toroid drifts away from critical coupling the result is an increase in transmission through the taper, P_F. However, the frequency of the non-scanning laser drifting off the resonance frequency of a toroid (or vice versa) produces the same change in P_F. Therefore, in order to lock the taper-toroid separation, the laser must first be locked to the toroid resonance.

This has been accomplished, at least in preliminary form, by using the error signal used in the characterization of toroids (Chapter 4) as the input to a simple proportional-integral-derivative (PID) locking program written in Labview (detailed in Appendix B). While the bandwidth of this virtual lock box is very low, about 200 Hz, the laser remains locked to the resonance with drift of less than 5% in the normalized amplitude of the toroid probe on resonance for more than an hour. Even then, it is generally a drift in the separation that causes the resonance dip, and hence the error signal, to disappear. The PID values are tuned in order to achieve a response that is both fast and stable over time. The proportional portion of the feedback, as its name implies, is a signal that is proportional to the error signal by a given gain value. The proportional gain is responsible for controlling fast deviations from the zero point. This value is increased until oscillations are observed in the taper output, then decreased just enough so that they disappear. The integral portion of the controller compensates for any drift accumulated over the long term that the proportional controller does not address. The integral gain is increased until the taper output becomes unlocked, at which point the value is decreased slightly. For this application the derivative aspect of the PID controller was not used. A more thorough explanation of PID controllers can be found in reference [66].

It should be noted that a precise, digital, high-bandwidth signal generator is used to generate the RF frequency for the optical sidebands when locking the frequency. Fluctuations in the magnitude of the signal driving the RF cause the phase of the error signal to change — effectively changing the sign of the PID gain values — thereby

chasing the frequency away from resonance rather than towards it. A high-precision voltage source in principle could also be used to drive a VCO, since the underlying requirement is stability in frequency.

6.2.2 Locking Taper-Toroid Separation

Once the laser has been locked to the chosen resonance frequency, a similar method is used to lock the separation between the taper and toroid to an arbitrary degree of coupling, diagramed in Figure 6.3. A drift in the position of the taper from critical coupling, both to and from the toroid, results in a rise in taper transmission P_F, as can be seen in Figure 5.1. In order to distinguish between these two directions the position needs to be dithered. When this dithering is mixed with P_F a phase difference (i.e., an error signal) occurs that is dependent on the direction of the drift. The dithering is produced by connecting the sinusoidal output of a function generator into the AC input of the Attocube positioner controller. However, it has been found that these positioners have a resonance at $\simeq 250$ Hz, which limits our bandwidth to frequencies well below this value. The error signal is used to control feedback created by a PID controller in Labview, similar to that described in Section 6.2.1. The proportional and integral gains are determined in the same way as they were for locking the laser frequency, once again the derivative gain is not used. The feedback signal is sent into the x-axis position controller, thereby locking the separation. Again, this locking has a very low bandwidth, < 100 Hz, but it has kept a toroid in the critically coupled regime for over an hour.

In order to quantify the stability and bandwidth of the locking scheme, the noise measurement from Section 6.1.3 is repeated. The difference between the Fourier transforms of the error signals for both the coupled and uncoupled taper is plotted for various values of P and I in Figure 6.4 (this plot is representative of many taken in order to fine-tune the proper combination of P and I gains). Of primary interest in this first locking attempt is the response at near DC, as this is the slow drift that we currently correct by manually adjusting the positioner. In the inset of Figure 6.4,

noise suppression of up to 10 dB at near 0 Hz can be seen. This is the quantified long-term stability, experimentally observed as a resonance maintaining a state of critical coupling for a long period of time. However, it is evident that for all but the lowest frequencies < 2 HZ, the noise floor is higher for all values of P and I than it is when the locking circuit is disconnected from the system. Since this is true even when all the gains (P, I, and D) are set to zero and the controller should in principle simply be outputting zero feedback, this can be attributed to some sort of noise in the computer setup (e.g., the data acquisition card producing the feedback voltage, the computer itself, or perhaps even the DC in connection on the position controller). In this preliminary attempt at locking of the taper-toroid position, this noise source was not determined but will need to be eliminated in order to achieve higher performance. Additionally, the large spike at 60 Hz was due to a ground loop and has since been eliminated.

If a non-contact coupling scheme is to be used to look for atom transits, a system which will lock the separation between the taper and toroid and suppress vibrations that convolute the signal from atoms — in a more effective manner than the system presented — is necessary. In future implementations of this locking scheme, an electronic servo, rather than computer based, will provide a higher bandwidth and, through judicious choice of components and design, a lower noise floor. Additionally, a separate, higher bandwidth piezo can be used to dither the separation. While the attocubes are ideal for the slow drift due to their long, fine-motion range of 7 μm, higher bandwidth piezos will potentially allow us to suppress not only the Attocube resonance at 250 Hz but also lower the entire noise floor for higher frequencies. Currently, atoms interact for $\simeq 2$ μs, which corresponds to a frequency of 500 kHz. Therefore, it is particularly important to suppress noise at this frequency; piezos are available that have bandwidths beyond this and should therefore be able to aid in this suppression.

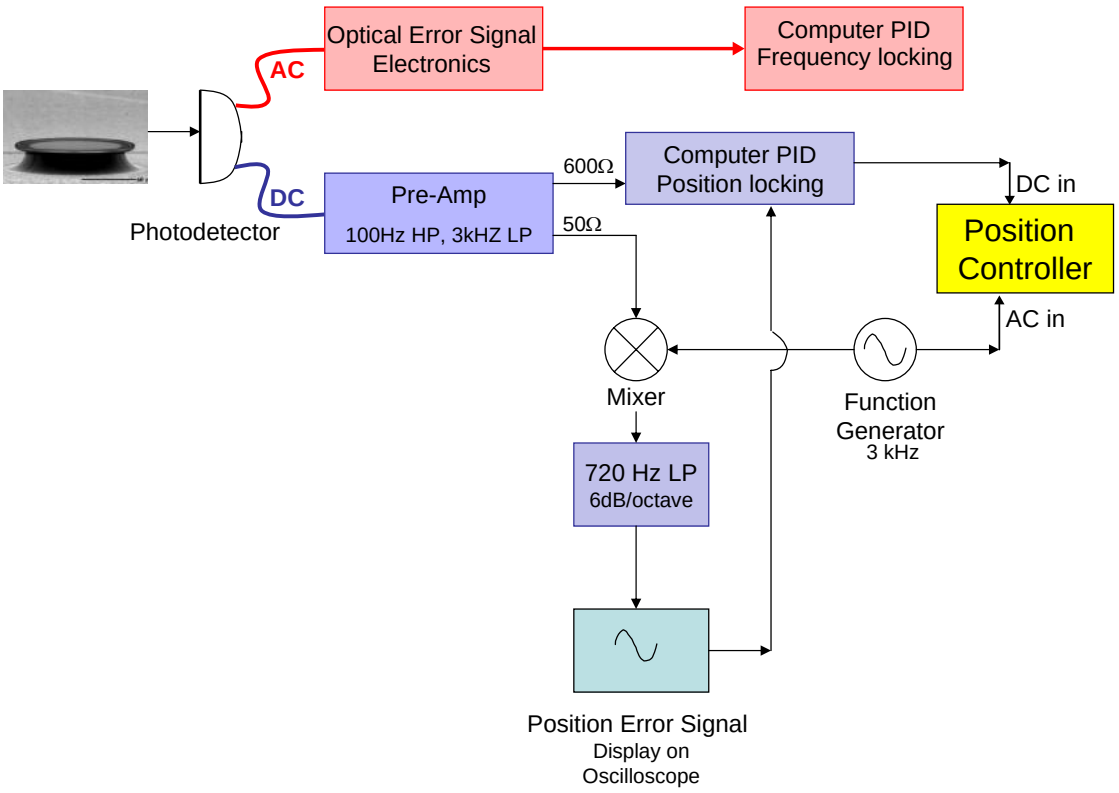

Figure 6.3: A computer is used to generate the locking feedback to the toroid positioner. While the laser is locked to the bottom of a resonance, the x-axis separation between the taper and toroid is dithered at 3 kHz in order to create a distinction between the directions of drift. The DC output of the photodetector is amplified. Both the 600 Ω and 50 Ω impedance outputs of the amplifier are used for simplicity in splitting the signal. The 50 Ω amplifier output is mixed with the dithering signal (3 kHz is low enough to be considered DC) to create an error signal. This error signal and the 600 Ω impedance output of the amplified DC signal from the photodetector are used by a Labview program on the computer to create feedback to the positioner, thereby locking the separation.

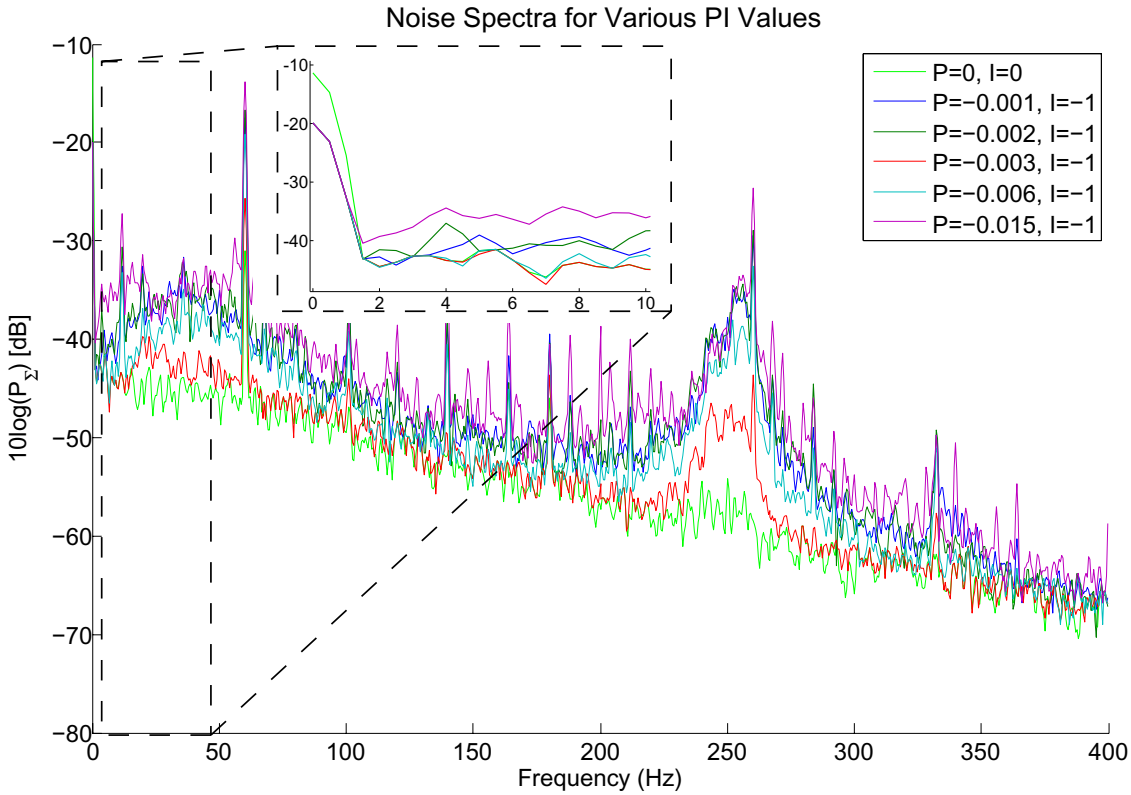

Figure 6.4: In order to fine-tune the parameters of the proportional and integral gains in the PID controller, the noise spectrum for various combinations of gain is taken. Shown is representative data in which the difference between the Fourier transforms of the error signals for coupled and uncoupled taper, plotted for various values of P and I. The spike at 60 Hz was due to a ground loop and has been eliminated. At frequencies below $\simeq$ 2 Hz the noise is suppressed by approximately 10 dB compared to the signal with no locking circuit. However, it is clear that the locking controller acts to add rather than suppress noise for higher frequencies. However, the goal for this first attempt at locking was to suppress the slow drift in taper-toroid separation that currently requires human intervention to correct, which was accomplished.

Appendix A

Appendix A: Solidworks Files

A key aspect to designing the preceding experiments was modeling components prior to manufacture and installation. Below is an overview of some pieces designed in the course of my work. These and many more are available on the accompanying CD.

A.1 Vacuum Chamber Design

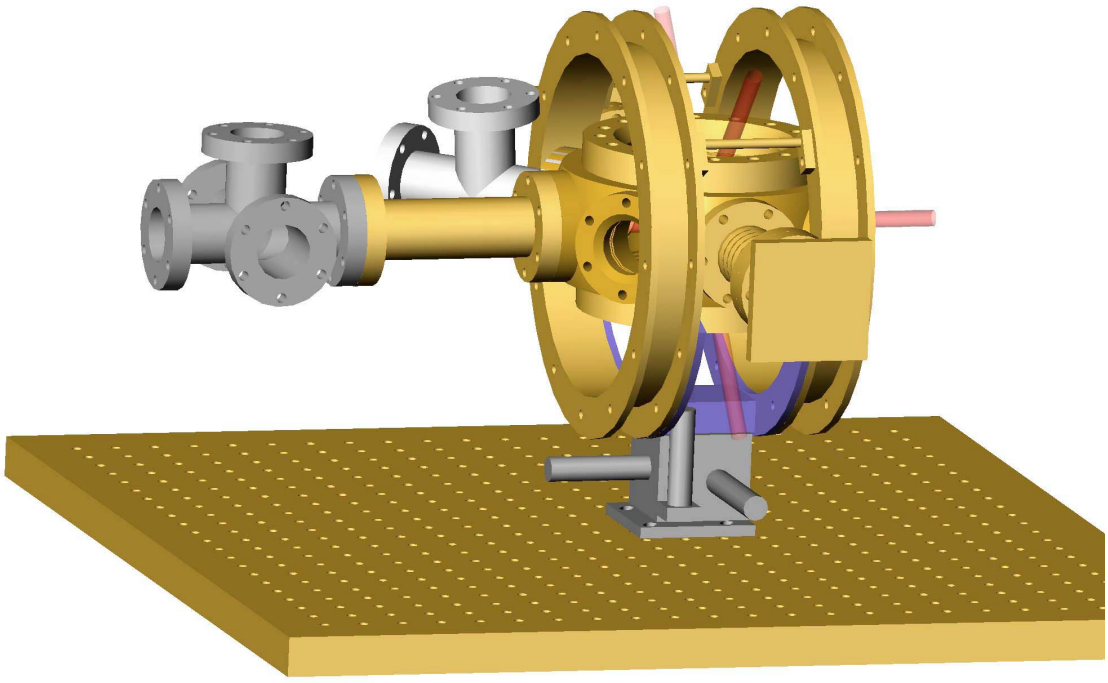

Figure A.1: Shown is a model of vacuum chamber setup for observing atom transits. All components are to scale and were modeled prior to any machining. The coils that produce the magnetic field for the atom trap are mounted on a positioner in order to finely align the MOT. All components, including optical beams, were included in order to conduct a virtual test of the experiment and ensure that components would not conflict with one another.

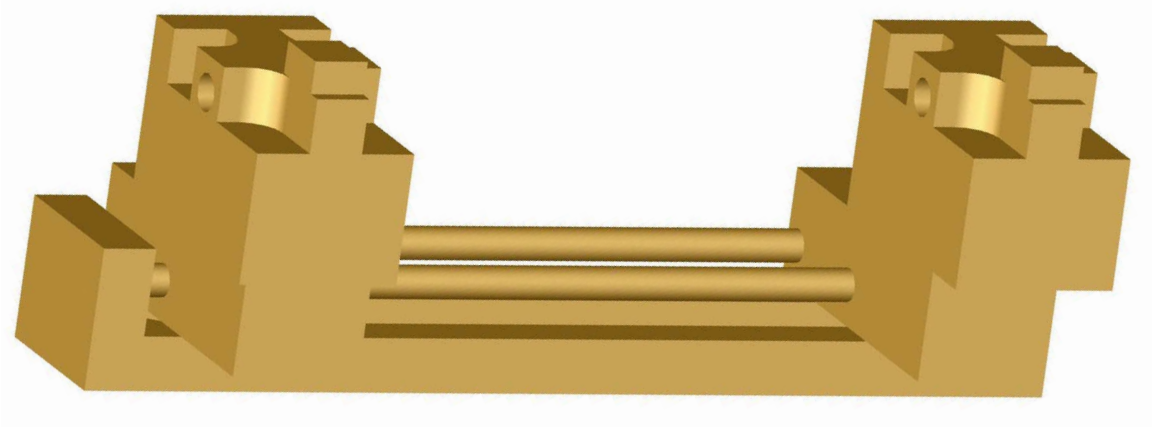

Figure A.2: The taper holder shown above was used in the first stage of the atom transit experiment from Chapter 2. This version employed clamps that were attached to the holder itself. In later versions the clamps remained fixed to the pulling apparatus while the fiber was glued to a more streamlined holder that fit in the same shelves shown in Figure A.3.

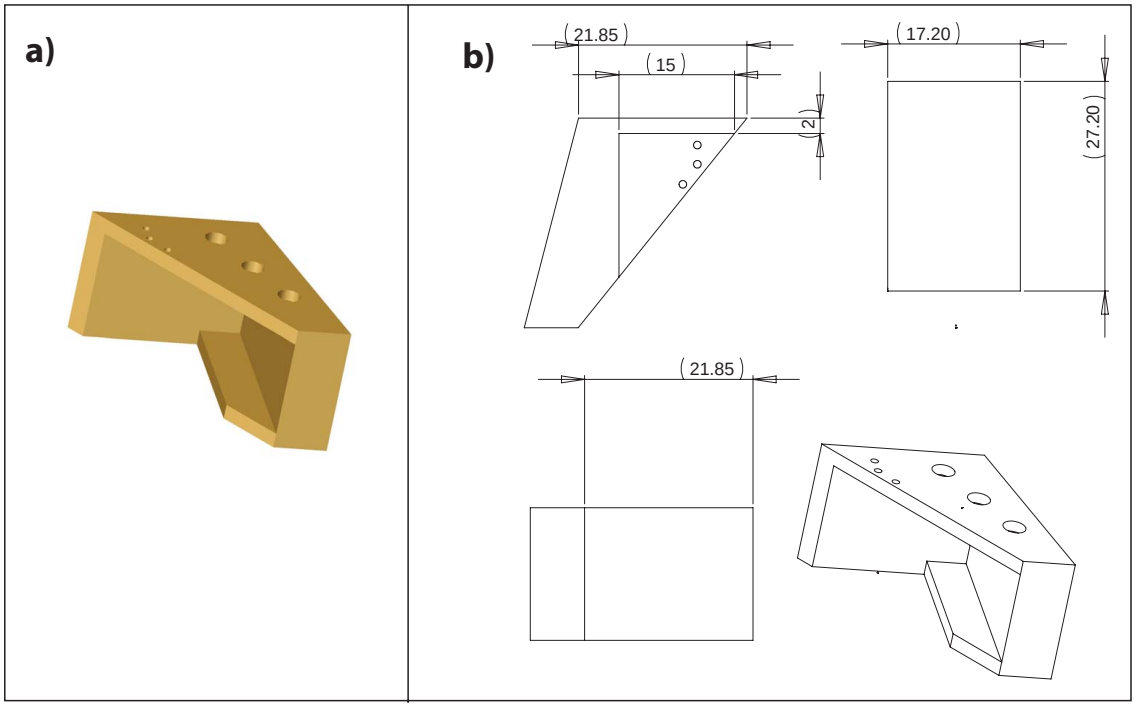

Figure A.3: The taper holder from Figure A.6 was held in the vacuum chamber by a pair of shelves as shown here. The taper holder slides easily into the shelves and is held in place with a set screw. The shelves are statically mounted to the chamber. (a) Scale model generated using Solidworks. (b) Dimensions of model from (a).

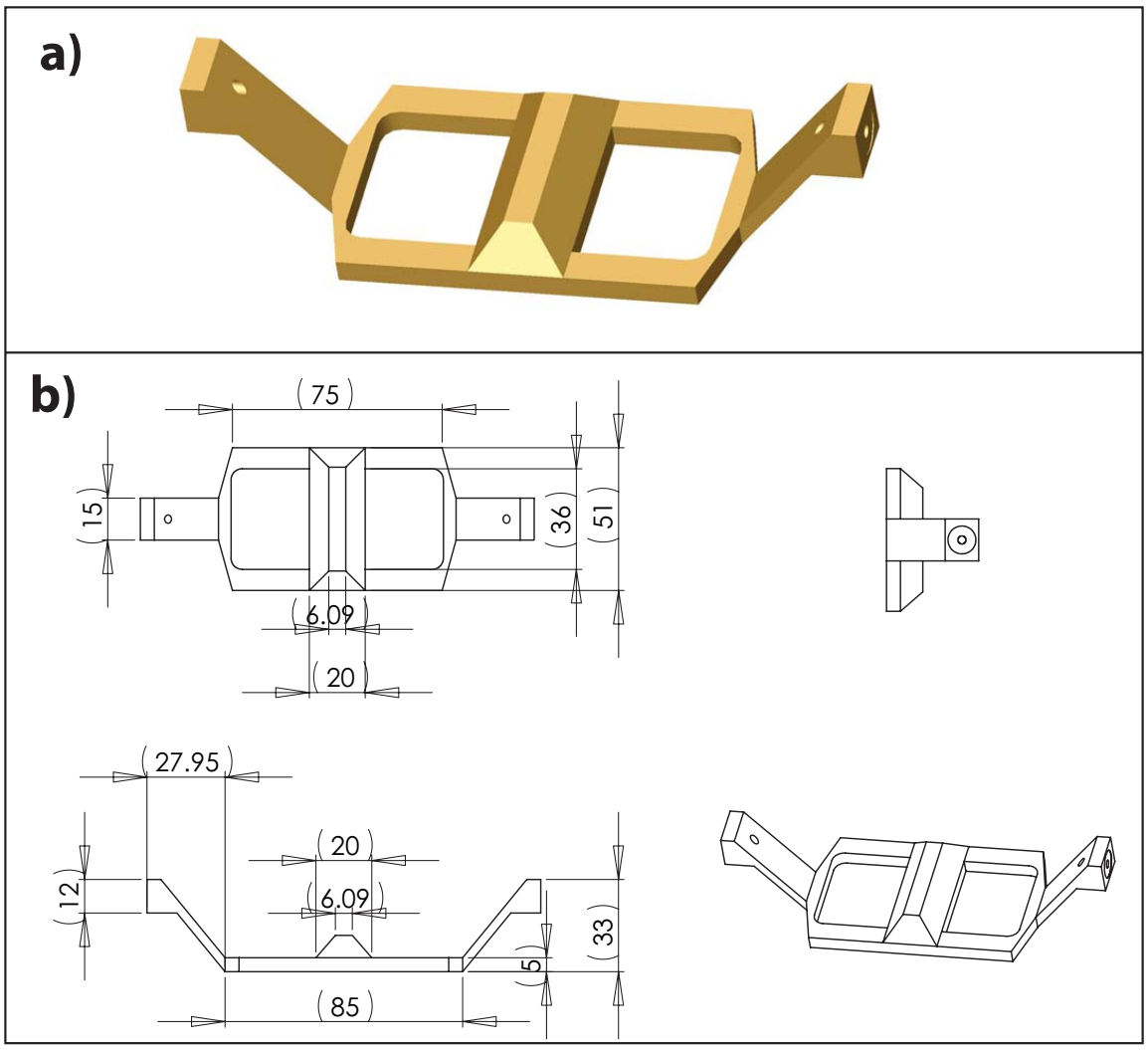

Figure A.4: The toroid was held in the vacuum chamber by this apparatus. In designing this holder the beams from the atom trap had to be taken into consideration along with the structural integrity of the piece. This holder positions the chip roughly in the center of the chamber. Rods (not shown) attached to either end of the holder are connected through a bellows to a pair of three-dimensional translation stages — used to control the coupling between the taper and toroid — that are located outside the vacuum chamber. (a) Scale model generated using Solidworks. (b) Dimensions of model from (a).

A.2 Characterization Apparatus

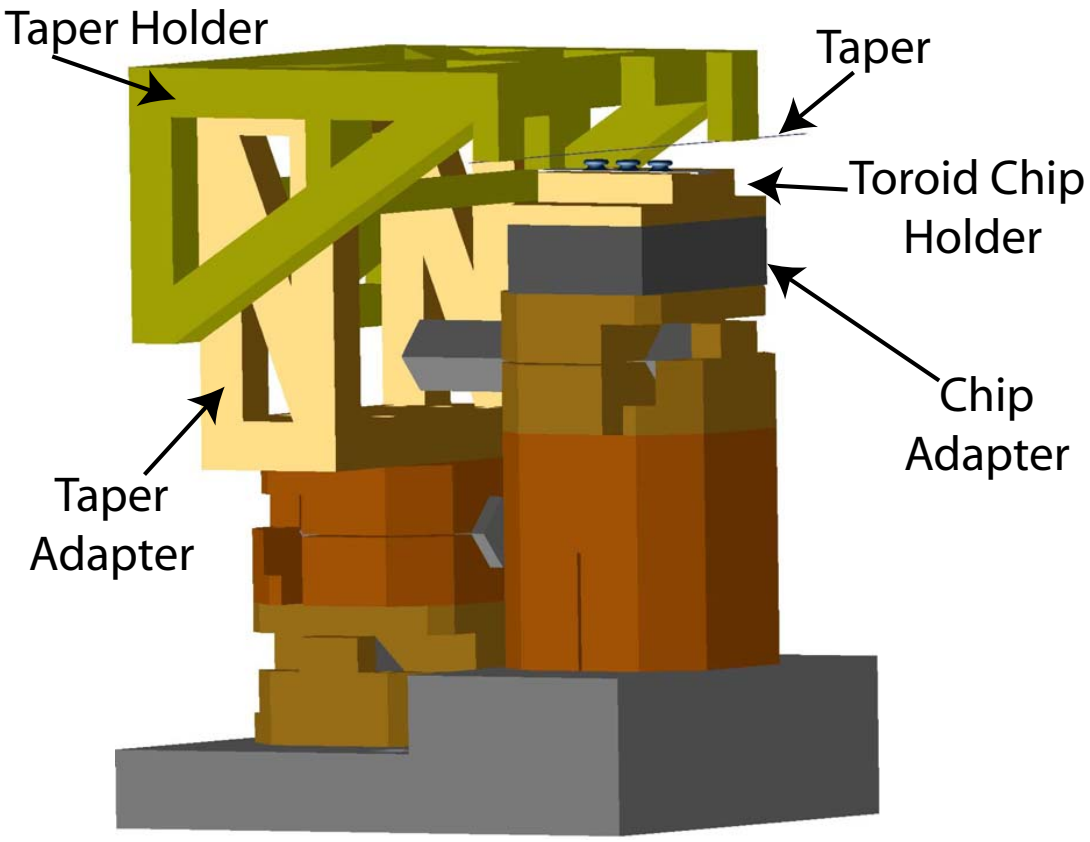

Figure A.5: Improvements in precision and locking abilities were made in this second-generation external coupling apparatus. While the use of Attocube positioners is the primary improvement (detailed in Section 4.2.4), experience led the way to design new methods of holding the chip and taper in the coupling apparatus. These new holders are more compact and easier to install. Labeled are the toroid chip and taper holders, as well as adapters used to slide the holders on and off the apparatus with minimal disturbance.

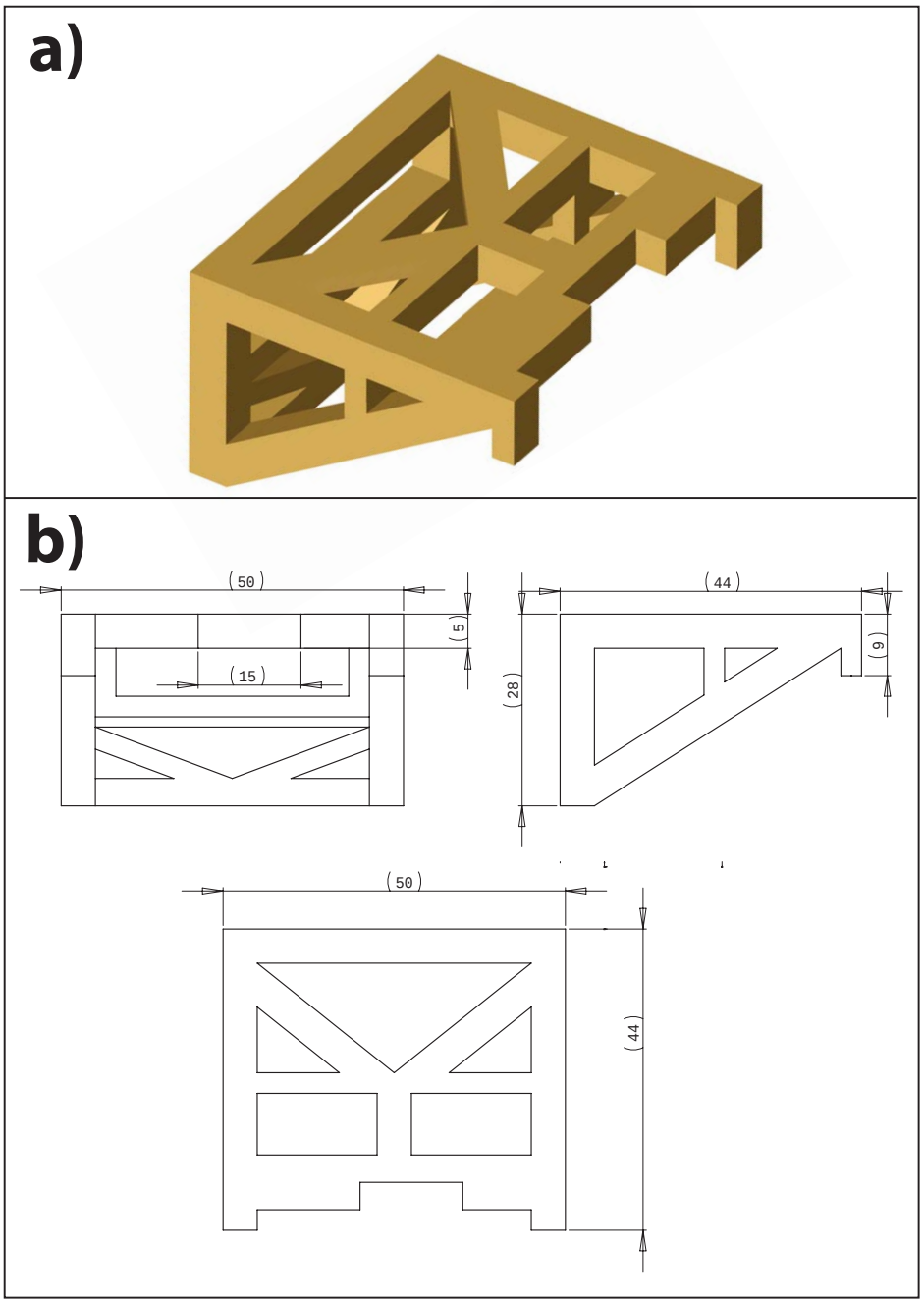

Figure A.6: The taper holder used in the second-generation coupling apparatus was designed to be light, easy to install, and have adequate optical access of the taper and toroid. The holder must cantilever in order for the taper to reach the toroid chip on the adjacent toroid stack as shown in Figure A.5. In order to minimize a "diving board effect" that would compromise the stability of the taper, a diagonal piece was used for support from the bottom. However, the Attocube positioners are only capable of supporting limited mass, therefore as much excess Aluminum as possible was milled out of the holder, hence the many holes. The holder slides onto the adapter, Figure A.7, requiring no screws due to the tight fit.

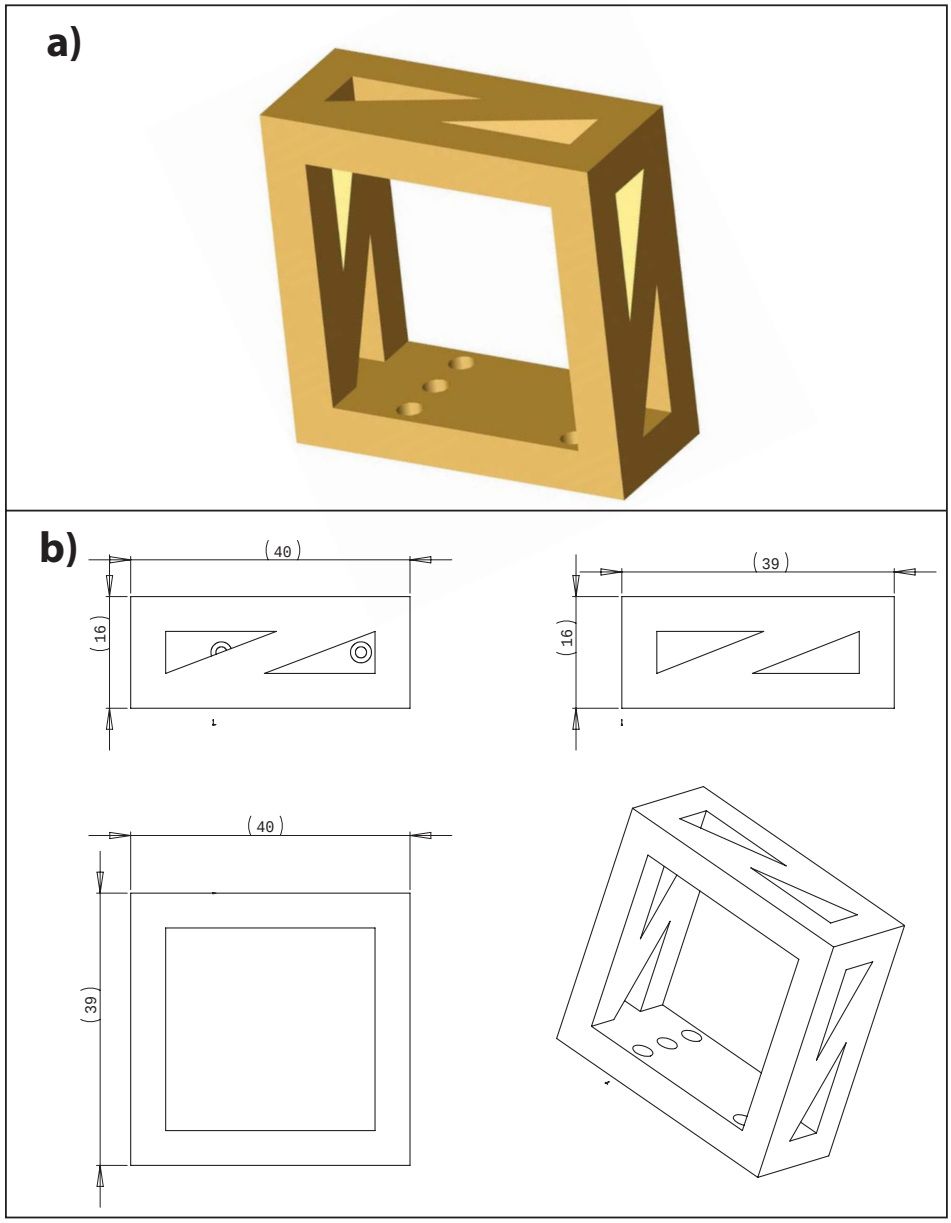

Figure A.7: In order to easily install the taper holder into the coupling apparatus this adapter was designed to be screwed to the top-most Attocube in the stack. The taper holder slides with minimal clearance over the adaptor, requiring no screws during installation. Vacuum grease is used as lubricant to ensure that the pieces slide smoothly against one another. Again, holes are drilled not only to minimize the weight which the Attocubes must support but to allow full motion of the Attocube that is supporting the toroid chip (see Figure A.5).

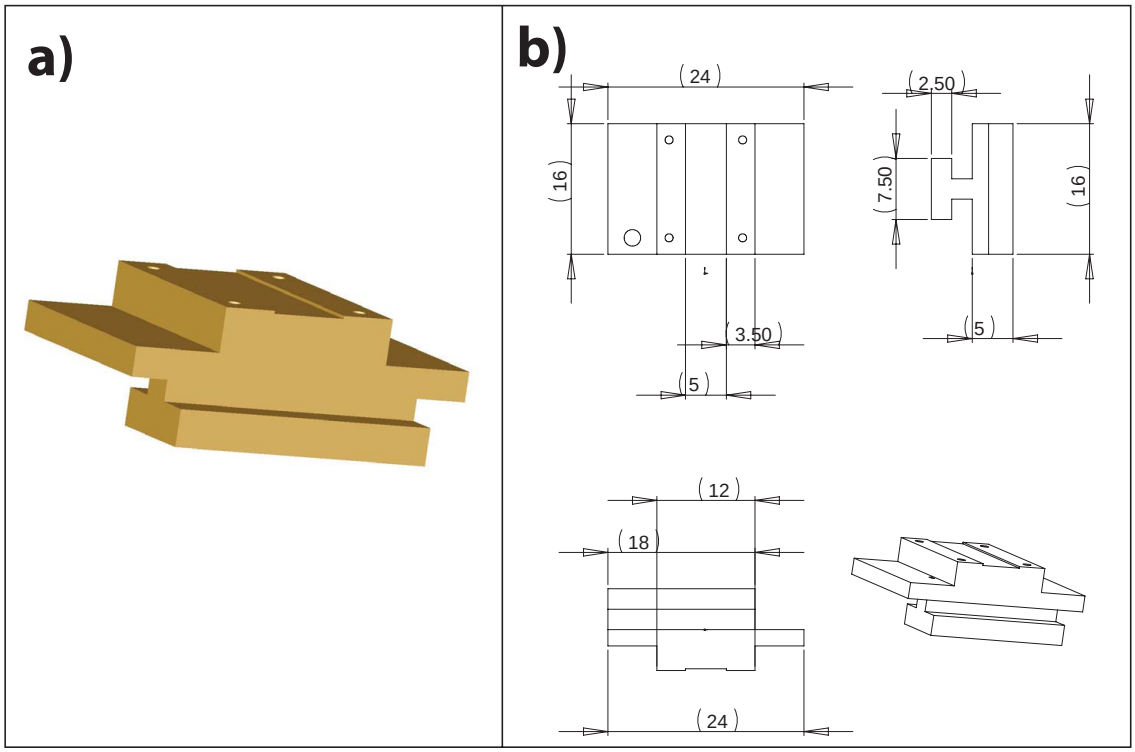

Figure A.8: As with the taper holder, the chip must be mounted to a holder which is easy to install and lightweight. This Aluminum holder is made to slide into its adapter, shown in Figure A.9, and is held in place with a set screw that is accessible from above. The chip is attached to this holder with vacuum-compatible carbon sticky pads (such as those used in SEM applications). The width of the platform that the chip is mounted on is minimal in order to lessen the chances of a non-parallel taper from hitting the platform during the initial alignment process.

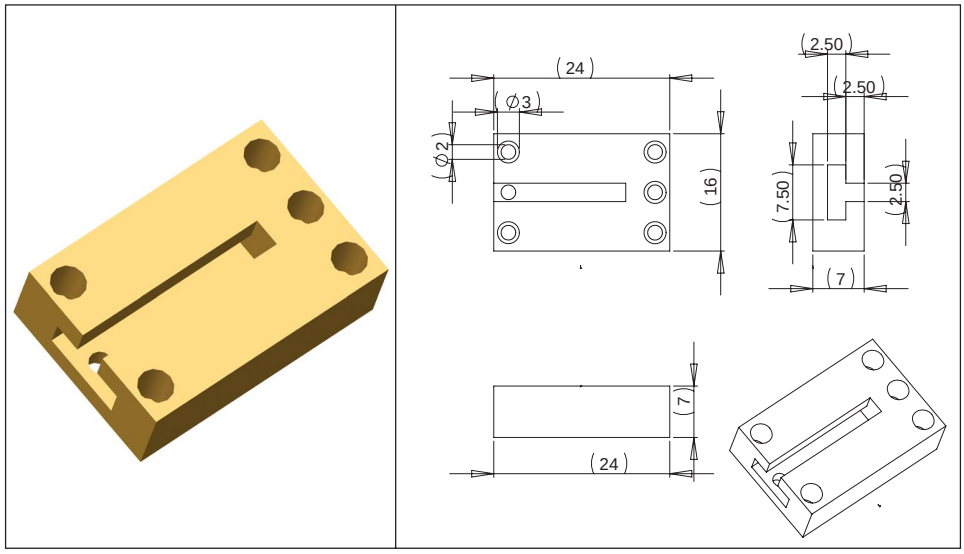

Figure A.9: This adapter is screwed to the Attocube stack which supports the toroid chip. The bottom piece of the chip holder, Figure A.8, slides tightly into the groove in this adapter. The groove does not go completely across but stops at the location that places the chip in the center of the stack. Again, vacuum grease is used as a lubricant in this sliding process.

Appendix B

Appendix B: Programs and Code

The following programs are available on the accompanying CD.

B.1 Matlab Code

B.1.1 Resonance Behavior as a Function of Coupling Strength

The following are the Matlab files used to parse the data taken from the output of a toroid resonance as a function of the separation between the taper and toroid.

The output of the toroid and each triangle wave used to generate the scans of both the laser frequency, as well as the taper-toroid separation, are recorded to one file. This measurement was repeated ten times. The following code parses each file, reduces it to one full scan of the position, and saves the data from each separate run of the experiment to one master data file which will be analyzed with another program.

Load_Mean_v2.m

```
%%%%%%%%%%%%%%%%%%%%%%%%%%%%%%%%%%%%%%%%%%%%%%%%%%%%%%%%%%%%%%%%%%%%%%%%%%%%
%%Load_Mean_v2.m
%%This file loads the data files from each run of the experiment and
%%separates each into full scans of position. These are then saved as
%%one master data file "Data.csv"

%%%%%%%%%%%%%%%%%%%%%%%%%%%%%%%%%%%%%%%%%%%%%%%%%%%%%%%%%%%%%%%%%%%%%%%%%%%%
%%Load all data files, which have the naming convention load Sweep_
%%1.csv %where the numbers increase from 1 to 10

%%each file contains three columns: the triangle wave which controls
%%the laser frequency sweep, the output of the taper, and the
triangle %%wave which controls the sweep of the taper-toroid separation
%%%%%%%%%%%%%%%%%%%%%%%%%%%%%%%%%%%%%%%%%%%%%%%%%%%%%%%%%%%%%%%%%%%%%%%%%%%%

clear all
N=10; %number of runs
N0=1; %starting run number
n=1;
for i=N0:N+N0-1
    eval(['load Sweep_' num2str(i) '.csv'])

%%%%%%%%%%%%%%%%%%%%%%%%%%%%%%%%%%%%%%%%%%%%%%%%%%%%%%%%%%%%%%%%%%%%%%%%%%%%
%%find the start of the position scan by finding the location in the
%%file of the minimum value
%%%%%%%%%%%%%%%%%%%%%%%%%%%%%%%%%%%%%%%%%%%%%%%%%%%%%%%%%%%%%%%%%%%%%%%%%%%%

    eval(['Start_T=min(find(Sweep_' num2str(i) '(:,3)==min(Sweep_'
num2str(i) '(:,3))));'])

%%%%%%%%%%%%%%%%%%%%%%%%%%%%%%%%%%%%%%%%%%%%%%%%%%%%%%%%%%%%%%%%%%%%%%%%%%%%
%%find the number of points "Length_T" of one complete scan of position
%%for the first set of data, the other files should be the same.
%%%%%%%%%%%%%%%%%%%%%%%%%%%%%%%%%%%%%%%%%%%%%%%%%%%%%%%%%%%%%%%%%%%%%%%%%%%%

    if i==1
        eval(['End_T=min(find(Sweep_' num2str(i) '(:,3)==max(Sweep_'
num2str(i) '(:,3))));'])
        Length_T=End_T-Start_T;
    end

%%%%%%%%%%%%%%%%%%%%%%%%%%%%%%%%%%%%%%%%%%%%%%%%%%%%%%%%%%%%%%%%%%%%%%%%%%%%
%%Since the position scan and the data taking are not synced the
%%scan of position starts at an arbitrary point in the data file.
%%Need to keep one full scan of position and discard the rest.
%%Save individual, full scans of position from all files to one master
%%file called "Data.csv"
%%%%%%%%%%%%%%%%%%%%%%%%%%%%%%%%%%%%%%%%%%%%%%%%%%%%%%%%%%%%%%%%%%%%%%%%%%%%
        if Start_T<End_T
            i;
         %Reduce file to one taper position sweep
```

```
        eval(['RSweep=Sweep_' num2str(i)
'(Start_T:Start_T+Length_T,:);'])
        eval(['Data(:,:,' num2str(n) ')=(RSweep);'])
        clear RSweep
        n=n+1;
        end
end
% % legend('Laser Frequency Sweep', 'Taper Output', 'Position Sweep')
% %switch columns 1 and 2
```

fun_Parkins_fit.m

```
%Definition of fun_Parkins_fit.m
%This is based on the theory of Scott Parkins

function [y]=fun(v,x)
kex=v(1);
k=(kex+1);
h=1.22;
x_0=v(2);
Tau=.022; %\kappa_i=1/Tau

a_out=i/(2*kex)^.5-((2*kex)^.5)*(i*k-(Tau*(x-1000*x_0))./(k^2-(Tau*(x-
1000*x_0)).^2+h^2+i*(2*k*(Tau*(x-1000*x_0))));

y=conj(a_out).*a_out*2*kex;
```

Parse and Fit Data

Coupling_v_Distance_v9.m

```
close all
clear all

%%%%%%%%%%%%%%%%%%%%%%%%%%%%%%%%%%%%%%%%%%%%%%%%%%%%%%%%%%%%%%%%%%%%%%%
%Load data files with the program Load_Mean_v2.m
%%%%%%%%%%%%%%%%%%%%%%%%%%%%%%%%%%%%%%%%%%%%%%%%%%%%%%%%%%%%%%%%%%%%%%%

Load_Mean_v2

%%%%%%%%%%%%%%%%%%%%%%%%%%%%%%%%%%%%%%%%%%%%%%%%%%%%%%%%%%%%%%%%%%%%%%%
%Load data from cesium reference in order to obtain an absolute
%frequency reference. This reference is swept over the same length as
%the laser in the data file which sweeps over a resonance. Therefore,
%the correlation between number of data points and frequency difference
%for the cesium reference data is the same as that for the resonance
%sweep
%%%%%%%%%%%%%%%%%%%%%%%%%%%%%%%%%%%%%%%%%%%%%%%%%%%%%%%%%%%%%%%%%%%%%%%
```

```
load CS_ref.csv

%%%%%%%%%%%%%%%%%%%%%%%%%%%%%%%%%%%%%%%%%%%%%%%%%%%%%%%%%%%%%%%%%%%%%%%
%Find the length of one sweep of the Cesium reference by taking the
%second derivative of the triangle sweep input and taking the distance
%between positive and negative slopes
%%%%%%%%%%%%%%%%%%%%%%%%%%%%%%%%%%%%%%%%%%%%%%%%%%%%%%%%%%%%%%%%%%%%%%%

DFsweep=(CS_ref(2:length(CS_ref),2)-CS_ref(1:length(CS_ref)-1,2));
    DFsweep=sign(DFsweep);
    DDFsweep=(DFsweep(2:length(DFsweep),1)-DFsweep(1:length(DFsweep)-
1,1));
    test=find(DDFsweep>0);
    test2=test(2:length(test))-test(1:length(test)-1);
    SweepLength=(max(test2)); %Number of points for one sweep cycle

    m=1
%%%%%%%%%%%%%%%%%%%%%%%%%%%%%%%%%%%%%%%%%%%%%%%%%%%%%%%%%%%%%%%%%%%%%%%
%Divide data into single sweeps of Cesium reference, combine into one
%file. In order to eliminate false, short sweeps caused by noise in the
%data, discard if the length of the sweep is less than 90% of the
%longest sweep given by "SweepLength"
%%%%%%%%%%%%%%%%%%%%%%%%%%%%%%%%%%%%%%%%%%%%%%%%%%%%%%%%%%%%%%%%%%%%%%%

for  i=1:length(test)-1
    if test(i+1)-test(i)>SweepLength*(.9)


OneSweepC(:,m)=eye(SweepLength,length(CS_ref(test(i):test(i+1),1)))*CS_
ref(test(i):test(i+1),1);

OneSweepCF(:,m)=eye(SweepLength,length(CS_ref(test(i):test(i+1),2)))*CS
_ref(test(i):test(i+1),2);
        m=m+1;
    end
end

%%%%%%%%%%%%%%%%%%%%%%%%%%%%%%%%%%%%%%%%%%%%%%%%%%%%%%%%%%%%%%%%%%%%%%%
%Plot cesium reference versus frequency and have user input the
%distance between two transistions that are approximately 100MHz apart
%%%%%%%%%%%%%%%%%%%%%%%%%%%%%%%%%%%%%%%%%%%%%%%%%%%%%%%%%%%%%%%%%%%%%%%

figure(10)
plot(OneSweepCF(:,1), OneSweepC(:,2))
axis([.05 .25 min(min(OneSweepC)) max(max(OneSweepC))])
temp=ginput
V2F=(temp(2,1)-temp(1,1))/100 % voltage to frequency in MHz


n=1
while n<=NumRuns
    clear DFsweep; clear DDFsweep; clear test; clear test2; clear
SweepLength;
```

```
%%%%%%%%%%%%%%%%%%%%%%%%%%%%%%%%%%%%%%%%%%%%%%%%%%%%%%%%%%%%%%%%%%%%%%%%
%find intervals of laser frequency sweep and put together in one file
%per column of the data file) in the same manner as for the Cesium
%reference sweep
%%%%%%%%%%%%%%%%%%%%%%%%%%%%%%%%%%%%%%%%%%%%%%%%%%%%%%%%%%%%%%%%%%%%%%%%

    DFsweep=(Data(2:length(Data),2,n)-Data(1:length(Data)-1,2,n));
    DFsweep=sign(DFsweep);
    DDFsweep=(DFsweep(2:length(DFsweep),1)-DFsweep(1:length(DFsweep)-
1,1));
    test=find(DDFsweep>0);
    test2=test(2:length(test))-test(1:length(test)-1);
    SweepLength=(max(test2)); %Number of points for one sweep cycle
    test3(n)=[n];


%%%%%%%%%%%%%%%%%%%%%%%%%%%%%%%%%%%%%%%%%%%%%%%%%%%%%%%%%%%%%%%%%%%%%%%%
%OneSweepT_i is the output of the toroid (the resonance) for one sweep
%OneSweepF_i is the frequency scan triangle wave for one sweep
%OneSweepP_i is the position scan triangle wave for one sweep
%%%%%%%%%%%%%%%%%%%%%%%%%%%%%%%%%%%%%%%%%%%%%%%%%%%%%%%%%%%%%%%%%%%%%%%%


    m=1;
    for i=1:length(test)-1
        if test(i+1)-test(i)>SweepLength*(.9)

            eval(['OneSweepT_' num2str(n)
'(:,m)=eye(SweepLength,length(Data(test(i):test(i+1),1)))*Data(test(i):
test(i+1),1,' num2str(n) ');'])
            eval(['OneSweepF_' num2str(n)
'(:,m)=eye(SweepLength,length(Data(test(i):test(i+1),2)))*Data(test(i):
test(i+1),2,' num2str(n) ');'])
            eval(['OneSweepP_' num2str(n)
'(:,m)=eye(SweepLength,length(Data(test(i):test(i+1),3)))*Data(test(i):
test(i+1),3,' num2str(n) ');'])
            m=m+1;
        end

%         n
    end
    eval(['SizeT(' num2str(n) ')=min(size(OneSweepT_' num2str(n)
'));'])
    SizeT_R=min(SizeT(find(SizeT)));

    n=n+1
end

MeanT=[zeros(250,SizeT_R)];
MeanF=[zeros(250,SizeT_R)];
MeanP=[zeros(250,SizeT_R)];

%%%%%%%%%%%%%%%%%%%%%%%%%%%%%%%%%%%%%%%%%%%%%%%%%%%%%%%%%%%%%%%%%%%%%%%%
%Add all data files of their respective types together in preparation
%for creating a mean value, to be done at end of while sequence
```

```
%%%%%%%%%%%%%%%%%%%%%%%%%%%%%%%%%%%%%%%%%%%%%%%%%%%%%%%%%%%%%%%%%%%%%%%%

n=1


while n<=NumRuns

    if i==(length(test)-1)

        eval(['MeanT=MeanT + (OneSweepT_'  num2str(n)
'(:,1:SizeT_R));'])
        eval(['MeanF=MeanF + (OneSweepF_'  num2str(n)
'(:,1:SizeT_R));'])
        eval(['MeanP=MeanP + (OneSweepP_'  num2str(n)
'(:,1:SizeT_R));'])
        %

    end

    n=n+1

end

for n=1:NumRuns
    eval(['DiffT=(OneSweepT_'  num2str(n) '(:,1:SizeT_R) - MeanT);'])
    SigmaT(:,n)=((1/(NumRuns-1)).*sum(DiffT.^2)).^.5;

    eval(['DiffF=(OneSweepF_'  num2str(n) '(:,1:SizeT_R) - MeanF);'])
    SigmaF(:,n)=((1/(NumRuns-1)).*sum(DiffF.^2)).^.5;

    eval(['DiffP=(OneSweepP_'  num2str(n) '(:,1:SizeT_R) - MeanP);'])
    SigmaP(:,n)=((1/(NumRuns-1)).*sum(DiffP.^2)).^.5;
end

%%%%%%%%%%%%%%%%%%%%%%%%%%%%%%%%%%%%%%%%%%%%%%%%%%%%%%%%%%%%%%%%%%%%%%%%
%Divide by number of runs to create the mean
%%%%%%%%%%%%%%%%%%%%%%%%%%%%%%%%%%%%%%%%%%%%%%%%%%%%%%%%%%%%%%%%%%%%%%%%

MeanT=-MeanT(:,1:SizeT_R)./NumRuns;
MeanF=MeanF(:,1:SizeT_R)./NumRuns;
MeanP=MeanP(:,1:SizeT_R)./NumRuns;
MeanT_max=max(MeanT);

%%%%%%%%%%%%%%%%%%%%%%%%%%%%%%%%%%%%%%%%%%%%%%%%%%%%%%%%%%%%%%%%%%%%%%%%
%%%%%%%%%%%%%%%%%%%%%%%%%%%%%%%%%%%%%%%%%%%%%%%%%%%%%%%%%%%%%%%%%%%%%%%%
%%%%%%%%%%%%%%%%%%%%%%%%%%%%%%%%%%%%%%%%%%%%%%%%%%%%%%%%%%%%%%%%%%%%%%%%
%Fit the ten most under coupled resonances in order to determine
%the intrinsic linewidth of each Lorentzian
%%%%%%%%%%%%%%%%%%%%%%%%%%%%%%%%%%%%%%%%%%%%%%%%%%%%%%%%%%%%%%%%%%%%%%%%
%%

for i=95:100

    x=MeanF(:,i)/V2F-min(MeanF(:,i)/V2F);
```

```
    yOrig=MeanT(:,i)/MeanT_max(i);

%%%%%%%%%%%%%%%%%%%%%%%%%%%%%%%%%%%%%%%%%%%%%%%%%%%%%%%%%%%%%%%%%%%%%%%%
%Plot each instance of a frequency scan (and hence a resonance at a
%different taper-toroid separation)
%%%%%%%%%%%%%%%%%%%%%%%%%%%%%%%%%%%%%%%%%%%%%%%%%%%%%%%%%%%%%%%%%%%%%%%%

    figure(3);
    plot(x,yOrig,'ob');
    axis([min(x) max(x) 0 1.2])
%     print('-dpng','-
r150',['C:\Lab\Data\Coupling_versus_Distance_090407\res_8k\movie_frames
_no_fit\couple' num2str(i) '.png'])
    hold on;

%%%%%%%%%%%%%%%%%%%%%%%%%%%%%%%%%%%%%%%%%%%%%%%%%%%%%%%%%%%%%%%%%%%%%%%%
%Define fit parameters
%%%%%%%%%%%%%%%%%%%%%%%%%%%%%%%%%%%%%%%%%%%%%%%%%%%%%%%%%%%%%%%%%%%%%%%%

    %% define start point
    kex=8;
    h=2.6;
    x_0=1.75;
%     Tau=.008;
    vStart=[kex,  x_0];
    yStart=fun_Parkins_fit(vStart,x);
    %         plot(x,yStart,'-r');

    %% using nlinfit
    OPTIONS = statset('MaxIter',5000);
    [vEnd, R(:,i)]=nlinfit(x,yOrig,@fun_Parkins_fit,vStart,OPTIONS);
    yEnd=fun_Parkins_fit(vEnd,x);

%%%%%%%%%%%%%%%%%%%%%%%%%%%%%%%%%%%%%%%%%%%%%%%%%%%%%%%%%%%%%%%%%%%%%%%%
%Plot the fit on top of the data from the previous plot
%%%%%%%%%%%%%%%%%%%%%%%%%%%%%%%%%%%%%%%%%%%%%%%%%%%%%%%%%%%%%%%%%%%%%%%%

    plot(x,yEnd,'-g');
    legend('Orig','Fit');
    set(gca,'Color',[0.7,0.7,0.7]);
    set(gcf,'Color',[1,1,1]);
    figure(3);
    hold off
%     FitUC(:,i)=[vEnd(1) vEnd(2) vEnd(3)*2/V2F vEnd(4)/V2F
vEnd(5)/V2F];
    FitUC(:,i)=[vEnd(1) 1.22 vEnd(2)];
    Fit_PlotUC(:,i)=yEnd;
    [vEnd(1) 1.22 vEnd(2)]
end

%%

%
% %%%%%%%%%%%%%%%%%%%%%%%%%%%%%%%%%%%%%%%%%%%%%%%%%%%%%%%%%%%%%%%%%%%%%%%%
```

```
% %Filter out the bad fits that are more than 1 sigma away from the
mean %of the first 75% of points
% %%%%%%%%%%%%%%%%%%%%%%%%%%%%%%%%%%%%%%%%%%%%%%%%%%%%%%%%%%%%%%%%%%%%%%%
%
xMR=find(abs(FitUC(3,:))<(abs(std(FitUC(3,:)))+abs(mean(FitUC(3,:)))) &
abs(FitUC(4,:))<(abs(std(FitUC(4,:)))+abs(mean(FitUC(4,:)))) &
abs(FitUC(5,:))<(abs(std(FitUC(5,:)))+abs(mean(FitUC(5,:)))) &
FitUC(3,:)>0 & FitUC(4,:)>0 & FitUC(5,:)>0);
% xMR=find(abs(Fit(1,:))<(mean(Fit(1,:))+abs(std(Fit(1,:)))) &
abs(Fit(2,:))<(mean(Fit(2,:))+abs(std(Fit(2,:)))) &
abs(Fit(3,:))<(mean(Fit(3,:))+abs(std(Fit(3,:)))) &
abs(Fit(4,:))<(mean(Fit(4,:))+abs(std(Fit(4,:)))) &
abs(Fit(5,:))<(mean(Fit(5,:))+abs(std(Fit(5,:)))));
MeanMinMaxP=(6/100)*15*[mean(MeanP(:,xMR)); min(MeanP(:,xMR));
max(MeanP(:,xMR))]; %times 15 because actual voltage to piezos is what
we record times 15

% %%%%%%%%%%%%%%%%%%%%%%%%%%%%%%%%%%%%%%%%%%%%%%%%%%%%%%%%%%%%%%%%%%%%%%%
% % %input start of coupling in position scan, call Xstart
% %%%%%%%%%%%%%%%%%%%%%%%%%%%%%%%%%%%%%%%%%%%%%%%%%%%%%%%%%%%%%%%%%%%%%%%
%
% Xstart=.1;
% Xoffset=mean(Fit(4,find(MeanMinMaxP(1,:)<(Xstart+.1*(6/100)*15) &
MeanMinMaxP(1,:)>(Xstart-.1*(6/100)*15)))) %times 15 because actual
voltage to piezos is what we record times 15
%
% Amp_Adj=abs(max(max(Fit(2,xMR)))); %adjust the amplitude of the
lorentzian to plot on same graph as FWHM
% %
% figure(4)
% plot(MeanMinMaxP(1,:),Fit(3,xMR)','.', MeanMinMaxP(1,:),-
Xoffset+Fit(4,xMR)','.', MeanMinMaxP(1,:),abs(Fit(5,xMR))','.',
MeanMinMaxP(1,:),(min(Fit_Plot(:,xMR))).*Amp_Adj)
% % axis([min(min(MeanMinMaxP)) max(max(MeanMinMaxP)) -.1 .8])
% % axis([.4 max(max(MeanMinMaxP)) -.1 .8])
% xlabel('Position of Scan (um)')
% ylabel('Frequency (MHz)')
% legend('\kappa_{ext}', 'Res. Shift', 'splitting h', 'Coupling Depth
(a.u)')
% %
```

B.2 Labview VIs

Automation streamlines the apparatuses used for taper pulling and toroid coupling. Labview code has been used to control the devices used in these processes, making them more powerful than when done manually. Included is the code used to partially automate the processes of taper pulling, toroid characterization, taper-toroid separation effect investigation, and taper-toroid separation locking. Additionally, some other code which has proven useful is included.

B.2.1 Taper Pulling

Front panel— While taper pulling, the data is automatically displayed and recorded on a computer. Although the majority of the pulling process is done manually, such as motor control and torch and fiber alignment, this automatic storage of data has allowed us to compile traces of every pull that has occurred in the year since the automation was implemented. This data is now available in order to analyze how pull behavior affects taper efficiency, as discussed in Chapter 3.

The Front Panel of the file *Taper_Pull_Data_v5.vi* is shown in Figure B.1. The output from the photodetector of the taper pulling setup is connected to the appropriate channel of the data acquisition (DAQ) card, (in the figure Dev2/ai4), and displayed on the graph shown here on the front panel. The parameters for the input port of the DAQ card are set in the upper-left zoomed view, where the physical channel and the upper and lower boundaries for the input signal can be set. The range for these boundaries should be set at the minimum value which will encompass the incoming signal in order to optimize resolution of the signal once it is digitized.

The sampling rate and number of samples to read are set in the section shown in the "Timing Parameters" zoomed view on the lower left of Figure B.1. The "number of samples" input determines how many samples the card will take before displaying those samples on the graph and written to the data file (this will be discussed more thoroughly below when the block diagram is discussed).

The path to which the data file will be saved is displayed below the graph. This

path is set automatically in the format $date \setminus pullN.csv$, where N is determined by the number of taper pulls that have been saved on a given date. When the taper pull begins, press the "Save" button to begin saving data.

Finally, the view zoomed in on the far right controls and displays the real time taper efficiency. At the beginning of a taper pull, once the fiber has been connected to the photodetector but the pull has not yet begun, the "Starting Mean" value is set when the button "Starting Mean" is pressed. The real time mean value of the signal is divided by that from the untapered fiber to determine the real-time "Taper Efficiency."

Block Diagram— Figure B.2 shows the block diagram for the file $Taper\_Pull\_Data\_v5.vi$. In section "a," the physical channel on the DAQ card is initialized, setting the range and sampling frequency values from the front panel.

Inside the while loop, which continues until the user presses the stop button on the front panel, in section "b," the data input channel is told how many samples to read for each iteration of the while loop. Since this determines how many samples will be acquired before the data is displayed or saved, the number of samples to read determines how quickly and smoothly the data appears on the graph. Clearly, the smaller the value the less delay time. However, if this is made too small then the time that it takes the computer to complete one while loop will dominate and data will once again be slow. For a given computer this value should, along with the sampling rate, be tuned for optimum performance.

Section "c" is the graph display input.

Section "d" creates the data file name and path. The VI that the filename is connected to sets the path shown on the front panel, creating folders and iteratively changing the filename as needed.

Section "e" saves the data to a file upon user request. When the "Save" button is pressed, "Write to Measurement File" runs. (This is a built-in Labview VI that is adequate, although slow, for saving data. A better program for saving large, continuous, data acquisition has been developed and is outlined in Section B.2.2)

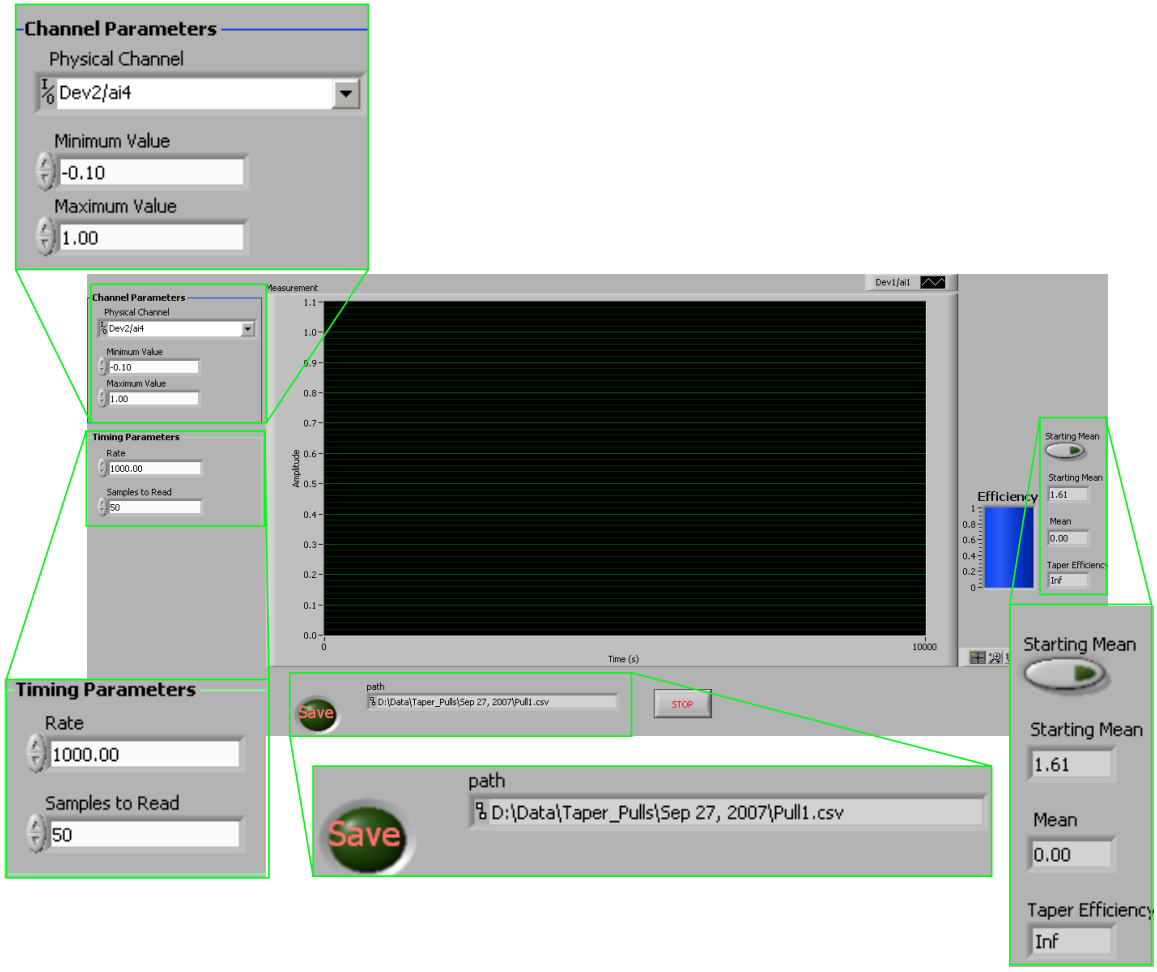

Figure B.1: *Taper_Pull_Data_v5.vi* Taper Pulling Labview VI: Front Panel

In section "f," the mean of the data is taken and, if the user presses the "Start Mean" button, is set as the "Starting Mean" value. The button is set to release after one instance of the while loop.

In section "g" the real time mean is displayed. This value is divided by the value stored as "Starting Mean" to determine and display the real time "Taper Efficiency."

Finally, in section "h," the virtual channel created from the physical channel in section "a" is cleared.

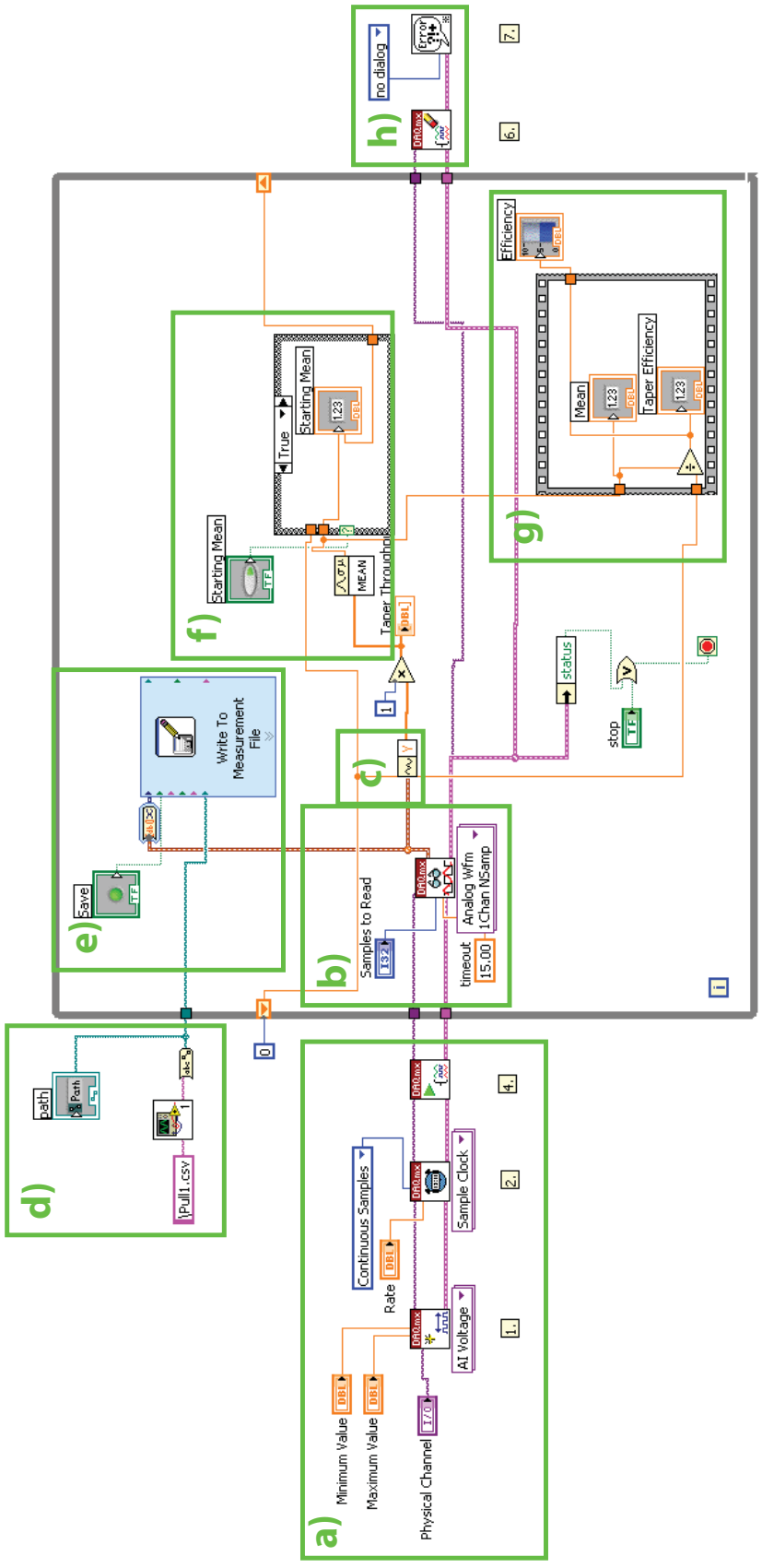

Figure B.2: Taper Pulling Labview VI: Block Diagram

B.2.2 Toroid Characterization

Front panel— In order to speed up and improve the process of characterizing toroids, I wrote a Labview program which automates the scanning of the laser frequency and taking of data. This is the program used for the procedures outlined in Chapter 4. The laser is controlled via serial connection. This program uses basic Labview VIs that came with the laser as a basis for communicating with the laser.

The front panel of the file *Coupling_Data_v*16*_no_piezo_control.vi* is shown in Figure B.3. The top graph shows the output of the taper, the error signal (Section 4.1), and the signal from the saturation absorption setup when the characterization is not occurring. This enables us to tune the coupling between the taper and toroid when the frequency of the laser is being scanned over a range $\simeq$ several hundered MHz (set by the user). The bottom graph shows these same signals as the top graph when they are being saved (this particular graph is not entirely useful since the data is saved over a such a large range— several nanometers— that individual resonances are beyond the resolution of the screen).

The same timing parameters described in Section B.2.1 are set on the front panel (top-left inset). Below this, the parameters governing the wavelength scan of the probe laser are set, including the start and stop wavelengths, the forward and backward scan rates, and the data resolution. The forward slewrate is the rate that the laser will scan when data is being taken. The slower the scan the easier it is for the computer to save the data, making higher-resolution data possible. The return slewrate is the rate at which the laser resets itself to the initial wavelength. Since this has no bearing on data taking, this can be set to a fast rate. The data resolution, "$\sharp Samples \setminus MHz$," sets how many sample points will be acquired per MHz. This is calculated based on the wavelength range of the sweep.

The lowest inset on the left hand side, "Sweep Parameters," sets the range for the input channels that acquire the signals displayed on the graphs.

The inset in the right shows the "Extinction Ratio" of a given coupled resonance. This measures, on the output of the taper, the ratio between the lowest and high-

est levels of the data. For a resonance, this measures how well coupled it is (e.g., on critical coupling, the minimum value should be zero on resonance, therefore the extinction ratio would be zero). Since zero light does not necessarily correspond to zero volts out of the photodetector, this background level is set and accounted for by pressing the "Set Zero" button while the light is blocked.

Also on the front panel is the path which displays the path to which the data will be saved. The toroid number is input by the user and used in the filename (the toroid number is a label given by the user to differentiate between different toroids on a chip. With the current mask, this numbering starts with the toroid nearest the lowest roman numeral).

Once the appropriate degree of coupling is achieved, the program will start sweeping the wavelength of the laser and saving data when the button "Sweep and Save" is pressed.

Block Diagram— The entire block diagram for this file is shown in Figure B.4. Due to the large size of this diagram, it is broken into three parts, as shown in Figure B.4. Part 1, Figure B.5, initializes the virtual channels from the physical channels that the signals are plugged into.

Part 2, Figure B.6, set the parameters necessary to display the signals for coupling the toroid, when the data is not being taken. Part "a" sets the digital output that controls a TTL switch — which turns the fine frequency sweep of the laser on and off — so that the fine frequency scan is on. Part "b" sets the number of samples for the input channel to record for each instance of the while loop. Part "c" set the wavelength of the laser to 852.2 nm, the location of the cesium resonances that we use for frequency calibration. Part "d" scales the three inputs so that they can be nicely displayed on the same graph. Part "e" is the input for the top graph of the front panel. Part "f" and part "g" are for setting the zero level and extinction ratio, respectively, of the taper output signal (discussed above).

Part 3 sets the inputs for the program $6300Sweep\_Liz\_v14\_with\_data.vi$, which is responsible for actually sweeping the laser and saving the data and is discussed

below.

Details for 6300 Sweep_Liz_v14_with_data.vi— The front panel for 6300*Sweep_Liz_v*14*_with_data.vi* has most of the inputs that are on the front panel for its parent file, *Coupling_Data_v*16*_no_piezo_control.vi*, as can be seen in Figure B.8.

The block diagram for 6300*Sweep_Liz_v*14*_with_data.vi* is shown in its entirety in Figure B.9, but is again too large to easily see and has therefore been broken up into four parts. Part 1, top of Figure B.10, initializes the connection with the laser, gets the current values for wavelength range and slewrates, and uses them to set the resolution at which data will be acquired. Part 2, bottom of Figure B.10, sets the values of the laser scan that are set by the user on the front panel. The program waits until the laser sends back a signal that the operations have been successfully completed. Part 3, top of Figure B.11, sets the filename and calculates the number of data points to be taken. The exact number required, based on the scan rate and scan range, is extended by 20% to account for any unaccounted for delays that may occur. Finally, in Part 4, bottom of Figure B.11, the data is saved using the file $ContAcq\&GraphVoltage-WriteDatatoSpreadsheetFile(CSV)\_v4.vi$ (detailed below in Section B.2.4). The program then waits for the signal from the laser that the operation is complete before terminating.

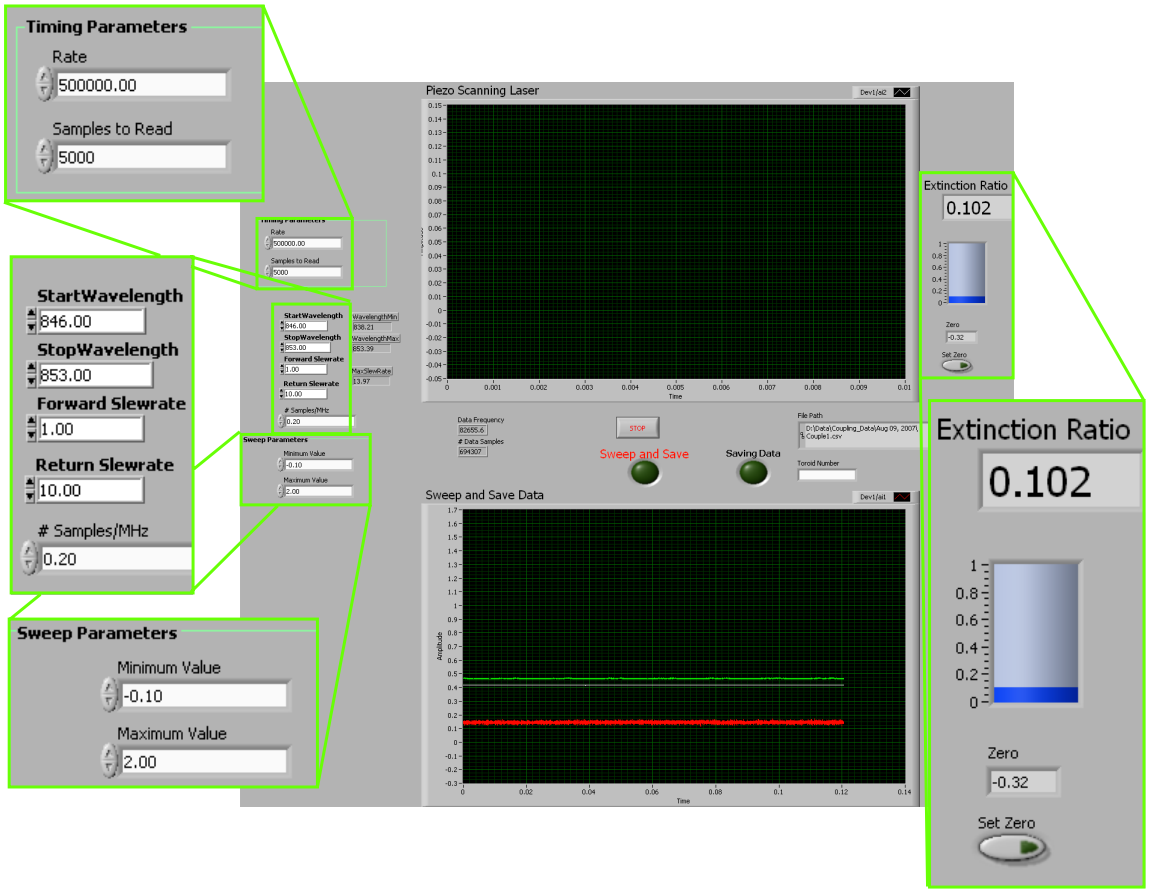

Figure B.3: Toroid Characterization Labview VI: Front Panel

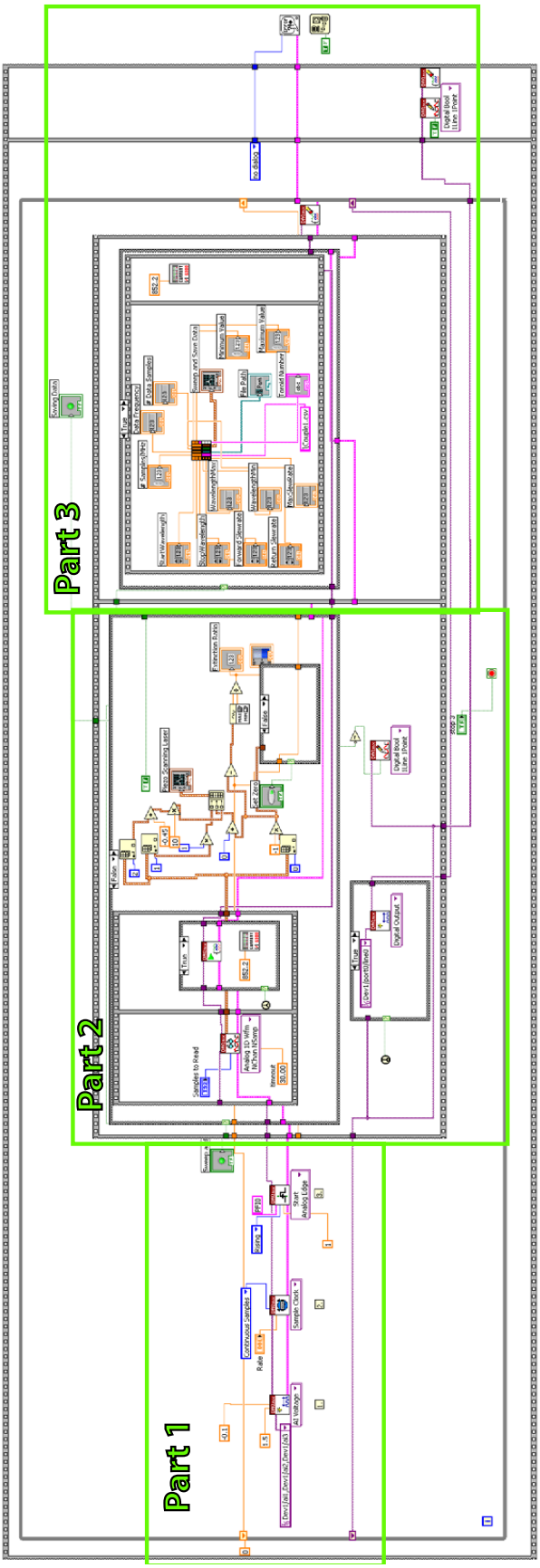

Figure B.4: Toroid Characterization Labview VI: Block Diagram

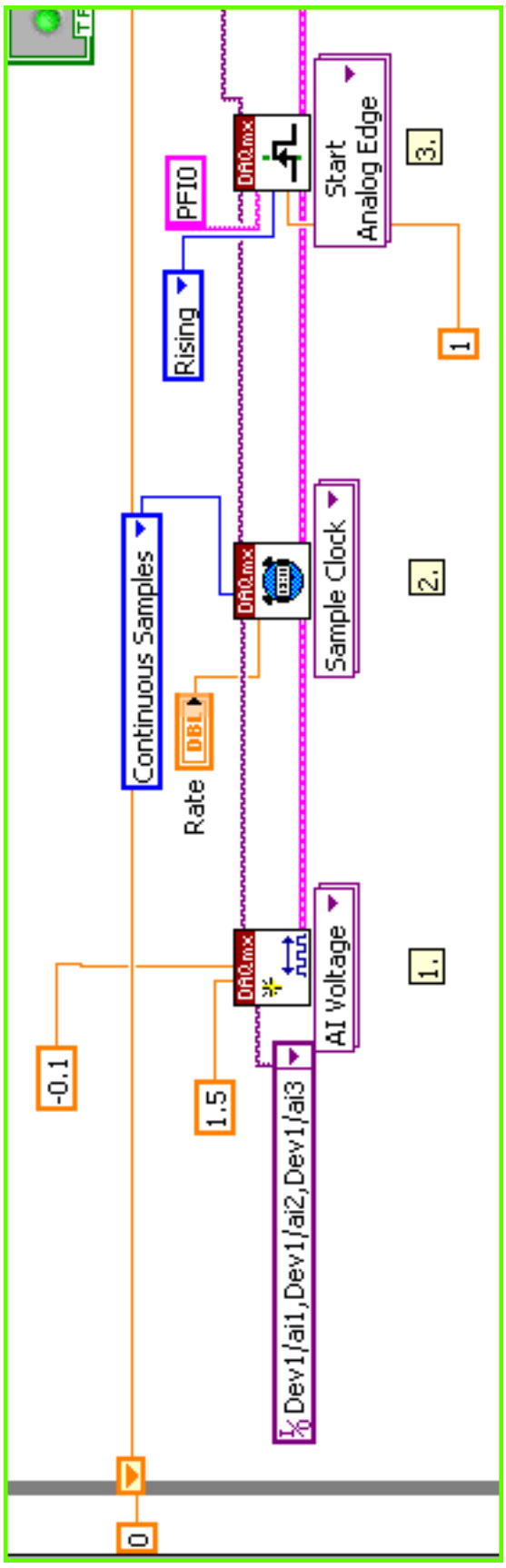

Figure B.5: Toroid Characterization Labview VI: Block Diagram Part 1

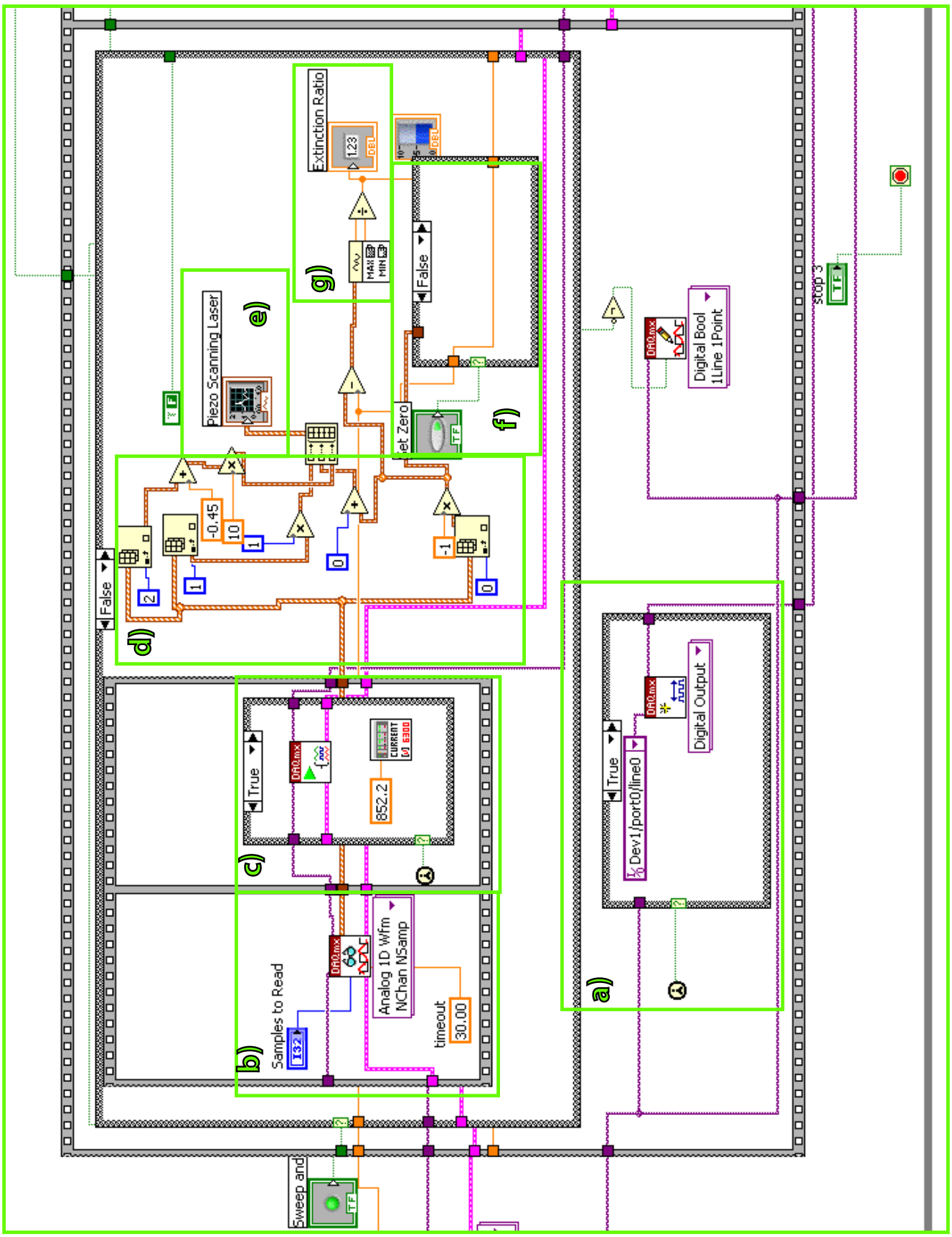

Figure B.6: Toroid Characterization Labview VI: Block Diagram Part 2

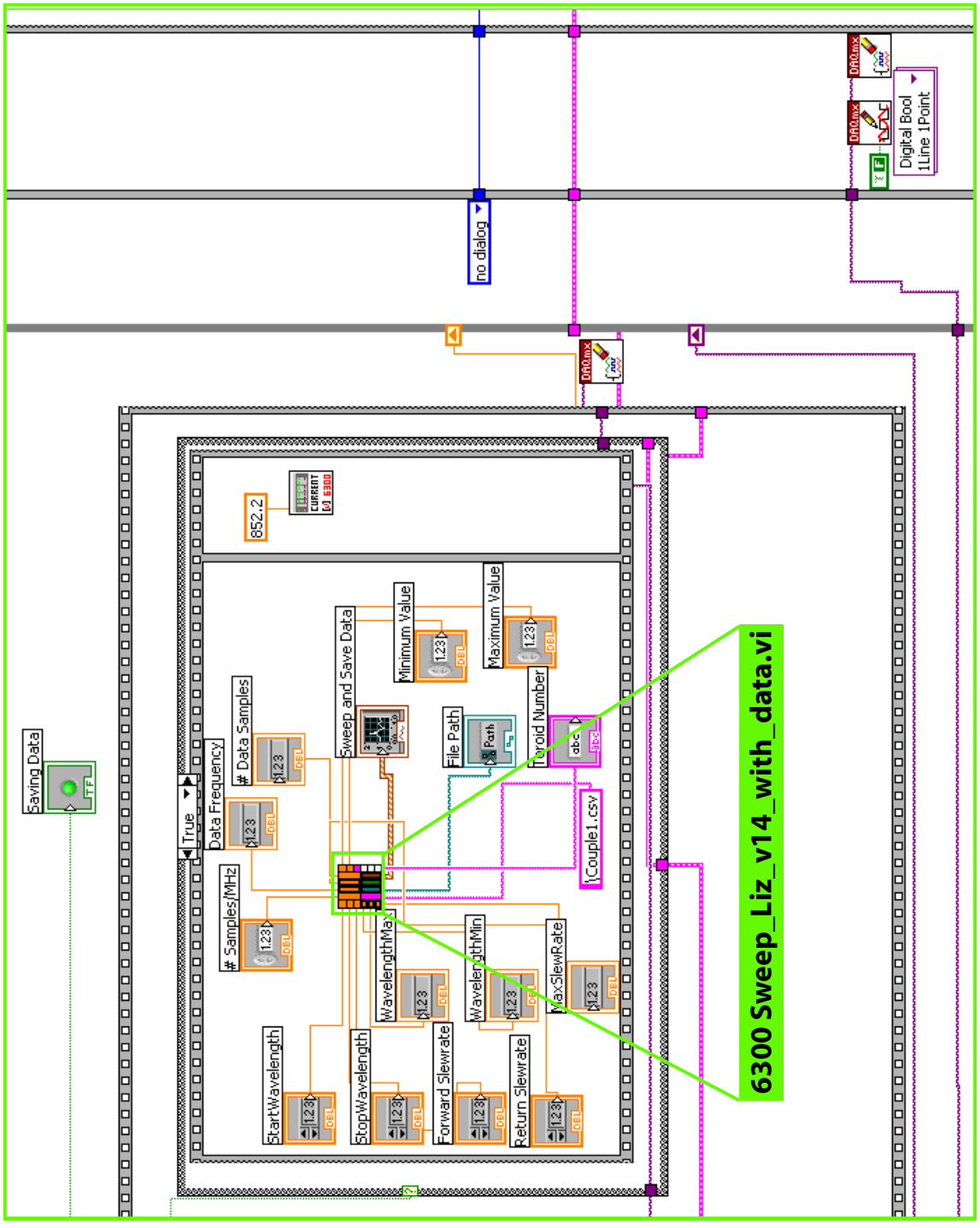

Figure B.7: Toroid Characterization Labview VI: Block Diagram Part 3

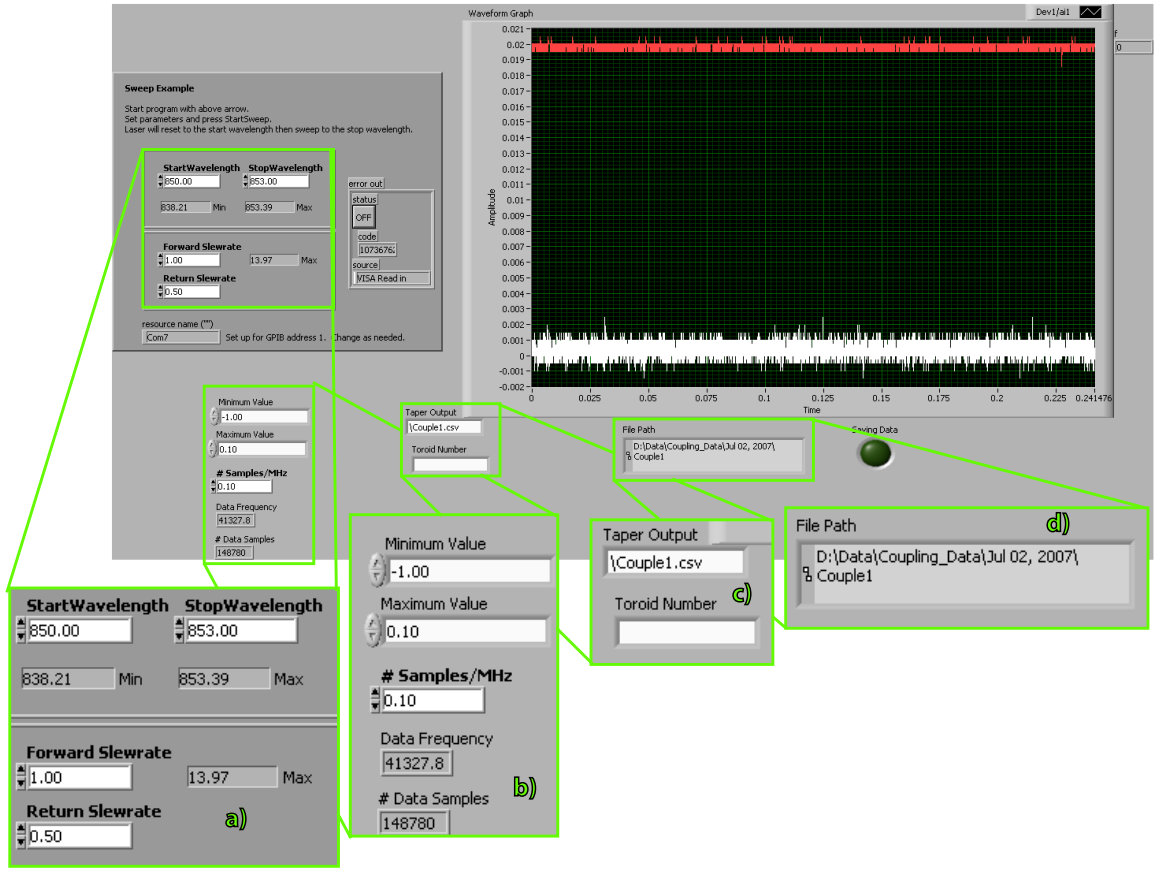

Figure B.8: Toroid Characterization, Sweep Laser Frequency Labview VI: Front Panel

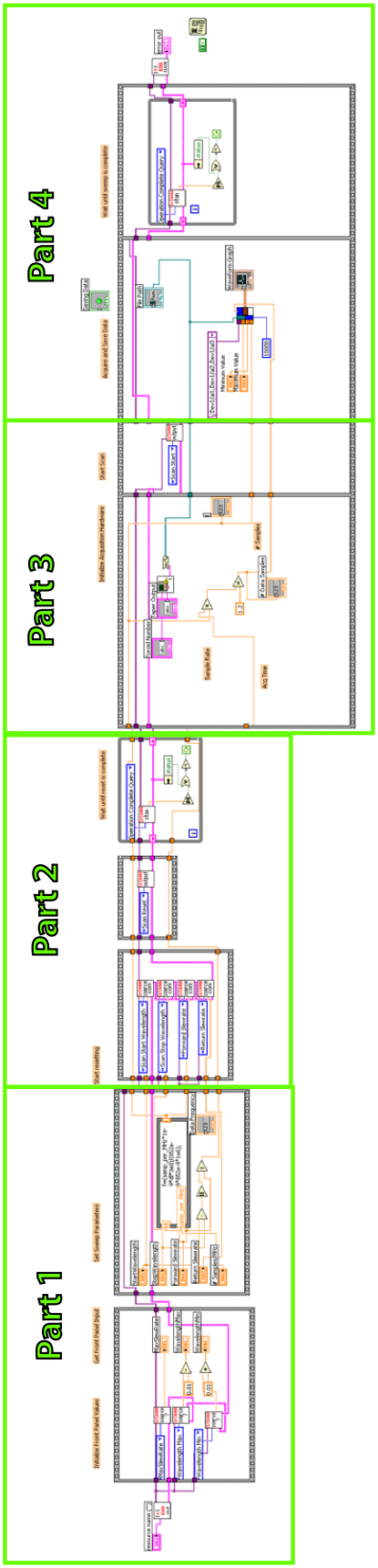

Figure B.9: Toroid Characterization, Sweep Laser Frequency Labview VI: Entire Block Diagram

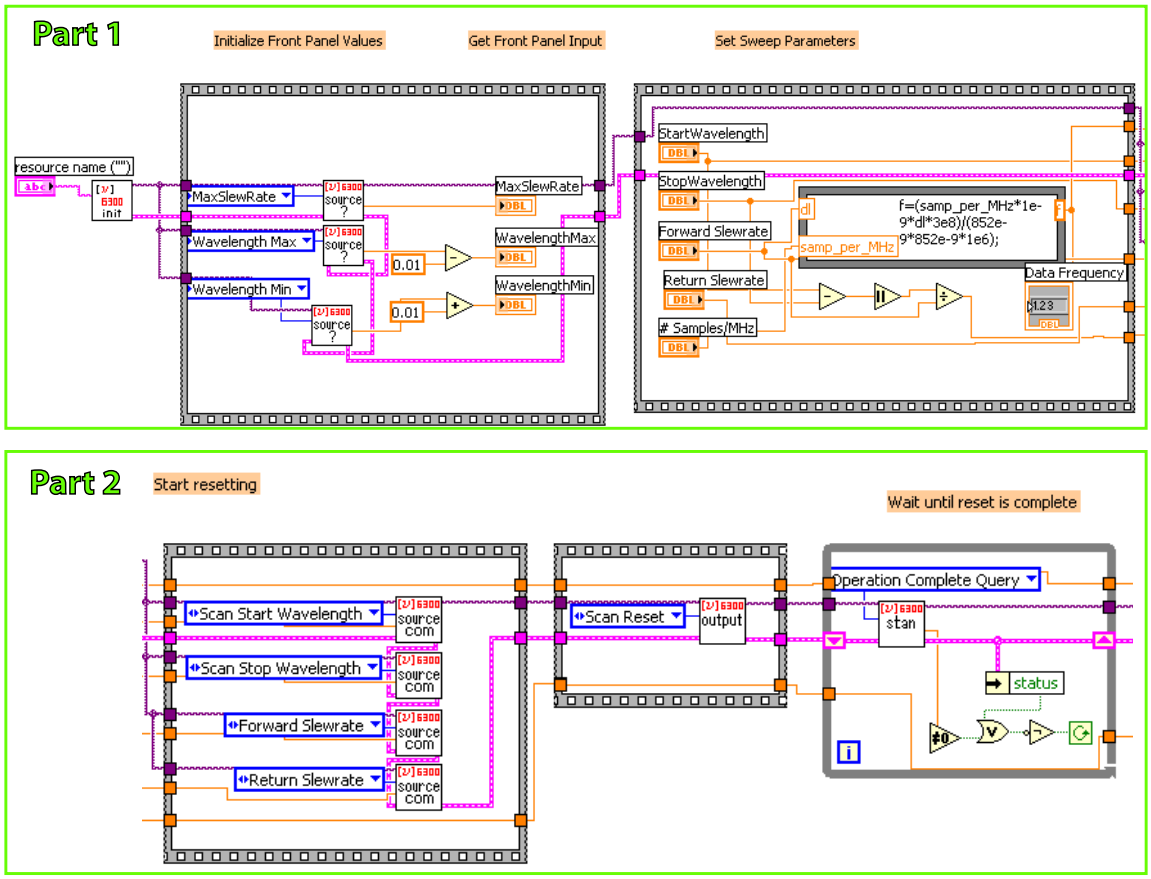

Figure B.10: Toroid Characterization, Sweep Laser Frequency Labview VI: Block Diagram Parts 1 and 2

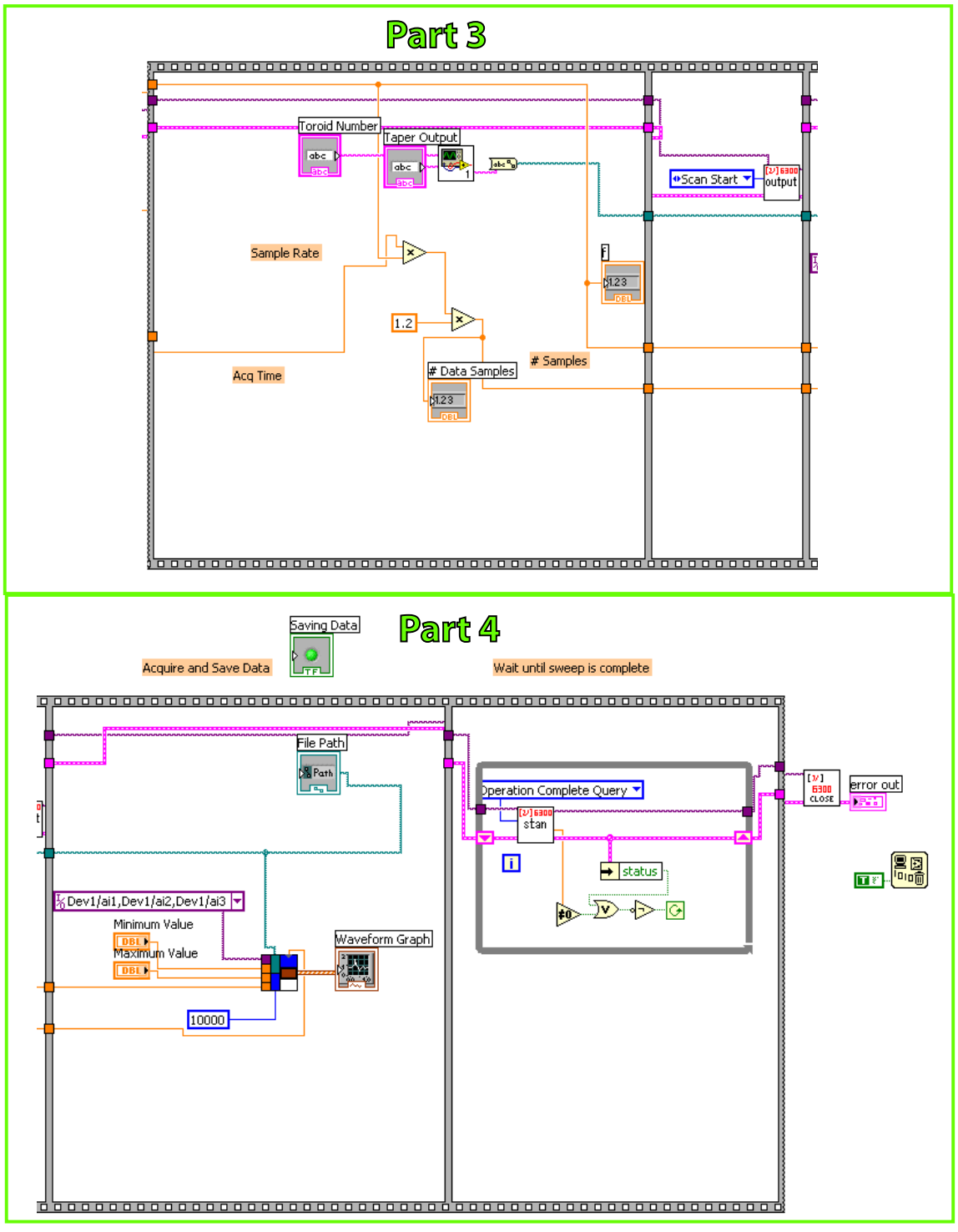

Figure B.11: Toroid Characterization, Sweep Laser Frequency Labview VI: Block Diagram Parts 3 and 4

B.2.3 Taper-Toroid-Laser Locking

In order to accomplish simple locking between both the laser frequency and a toroid, as well as the taper-toroid separation, in two axes, a simple PID locking circuit has been written for Labview. Figure B.12 shows the front panel for the program *PID Control Loop__Control3_v1.vi*, which controls the locking of the three previously mentioned entities. Section "a" sets the loop delay and offset. The loop delay sets an upper limit on the bandwidth of the circuit, while the offset determines to what point in the error signal the locking should occur (this is necessary since our error signal has an offset. This is also useful for locking to a point other than the bottom of the resonance). Section "b" locks the laser frequency to the toroid resonance. Sections "c" and "d" lock to the x and z axes of the taper-toroid separation, respectively. The block diagram is shown, in entirety, in Figure B.13. The components will be discussed in more detail below when a simple, one-axis, locking circuit is analyzed.

The circuit shown above consists, essentially, of three one-axis locking systems. To more easily understand the method of locking, the simple one-axis locking program, upon which the three-axis program was based, will be analyzed. The front panel and block diagram of this program, *PID Control Loop_v4.vi*, is shown in figures B.14 and B.15. On the front panel, in section "a" the gain values P, I, and D are set. These are the proportional, integration, and derivative gains, respectively. Section "b" sets the range of the feedback signal. Section "c" sets the polarity of the gain (in case the phase of the error signal changes) as well as the offset. Again, the offset is the level on the error signal to which the circuit will attempt to lock. Section "d" is essentially an additional offset in the case that locking to a point other than the bottom of the resonance is desired. Section "e" sets the bandwidth of the circuit through settings of the loop delay. Sections "f," "g," and "h" display the setpoint on the error signal to which the circuit will lock, the error signal itself, and the feedback signal that is generated. The averaging switch that is crossed out is not in use.

Figure B.15 shows the block diagram for *PID Control Loop__Control3_v1.vi*. In section "a" the input and output channels are initialized. In section "b" a smal

number of points of the error signal are acquired, and in section "c" the mean of these points is taken before being sent into the PID calculation frames. Section "d" inputs the gain values P, I, and D. Depending on the polarization switch, they are either multiplied by one or negative one. In section "e" these values, along with the set point, are input in to the PID calculation frames. The integration output is dependent on the history of the error signals. Section "f" resets these values for the first iteration, and inputs the values from the n-1 iteration thereafter. Section "g" contains the PID calculation frames. The PID output feedback is plotted in section "h," and section "i" closes the output channel when either locking is manually stopped or an error occurs.

The PID calculation frames are shown in Figure B.16. Frame "a" acquires the time elapsed since the last iteration. Frame "b" calculates the difference between the error signal and the set point. The proportional output is calculated in frame "c" by multiplying the proportional gain by the error difference calculated in frame "b." In frame "d," the derivative component to the output is calculated by dividing the difference between the error difference from the previous iteration and the current iteration with the time difference calculated in frame "a." Finally, in frame "e," the integration component is calculated. The error difference from frame "b" is multiplied by the time elapsed from frame "a" and added to the error difference from the previous iteration. It is combined with the proportional and derivative components from frames "c" and "d". If this exceeds either boundary on the output range of the feedback then the signal rails at its limit.

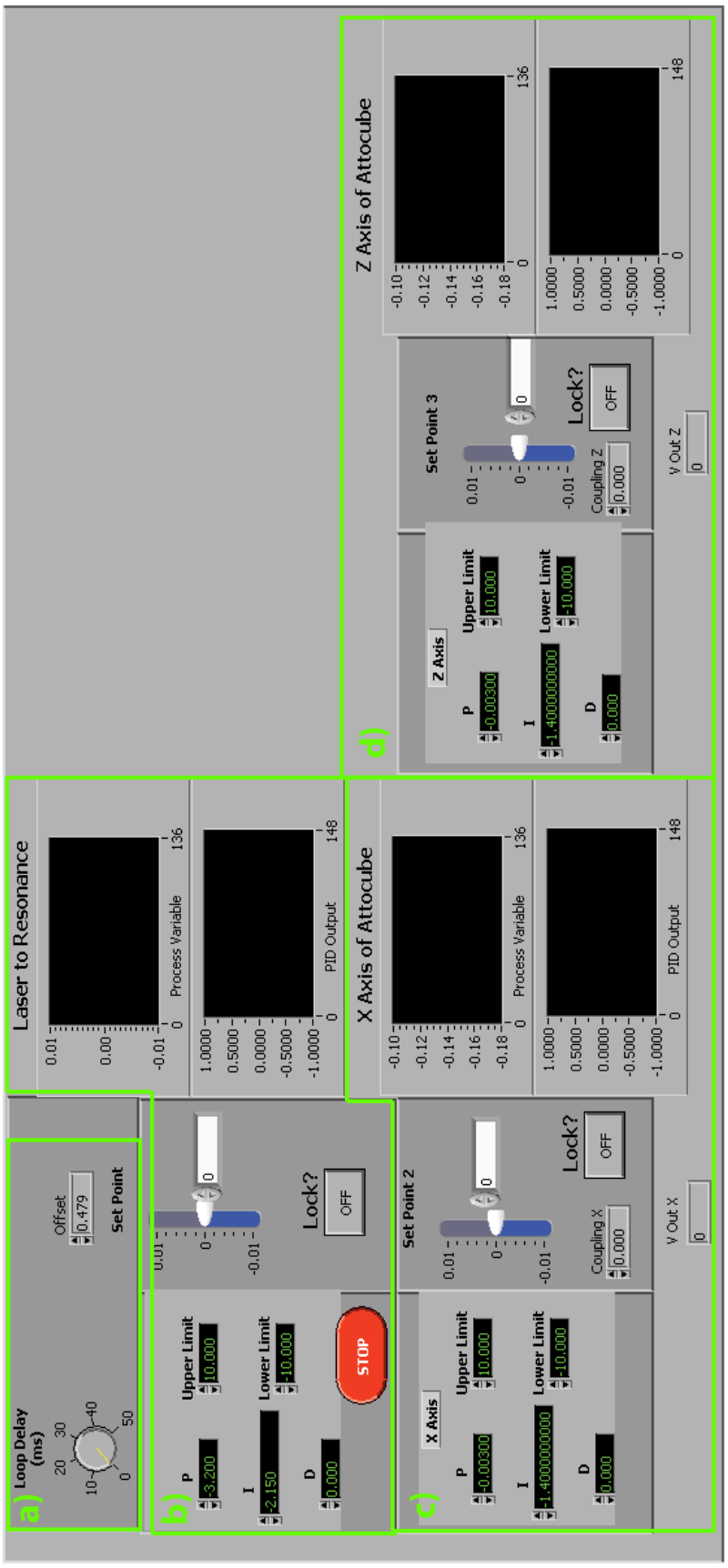

Figure B.12: *PID Control Loop_Control3_v1.vi* Locking of laser frequency to toroid resonance as well as taper-toroid separation Labview VI: Front Panel

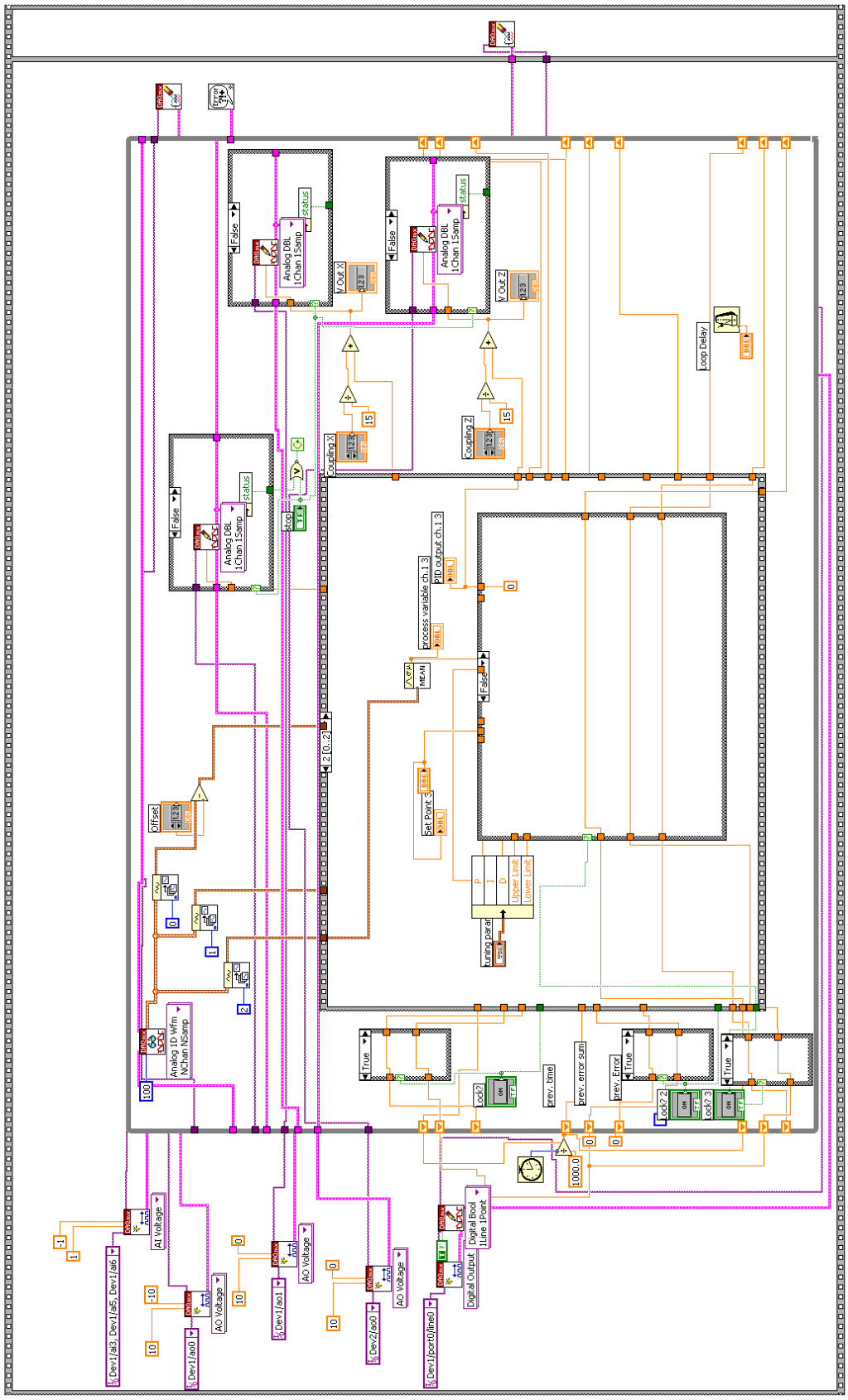

Figure B.13: *PID Control Loop_Control3_v1.vi* Locking of laser frequency to toroid resonance as well as taper-toroid separation Labview VI: Block Diagram

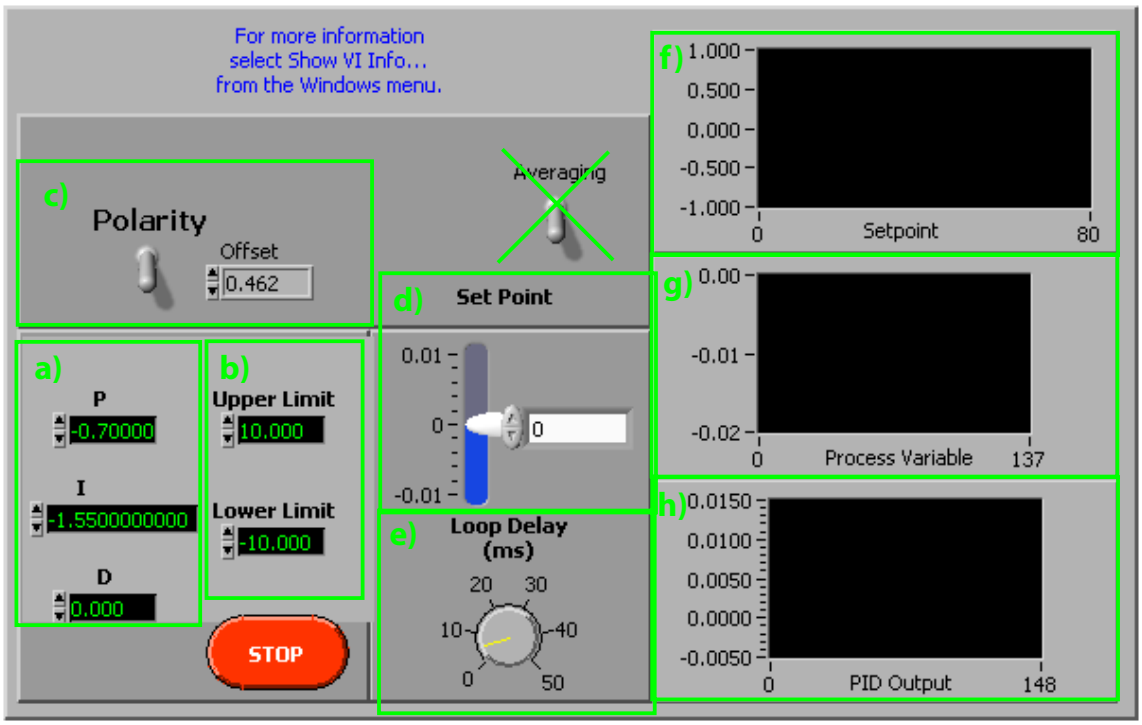

Figure B.14: *PID Control Loop_v4.vi* Locking of one entity Labview VI: Front Panel

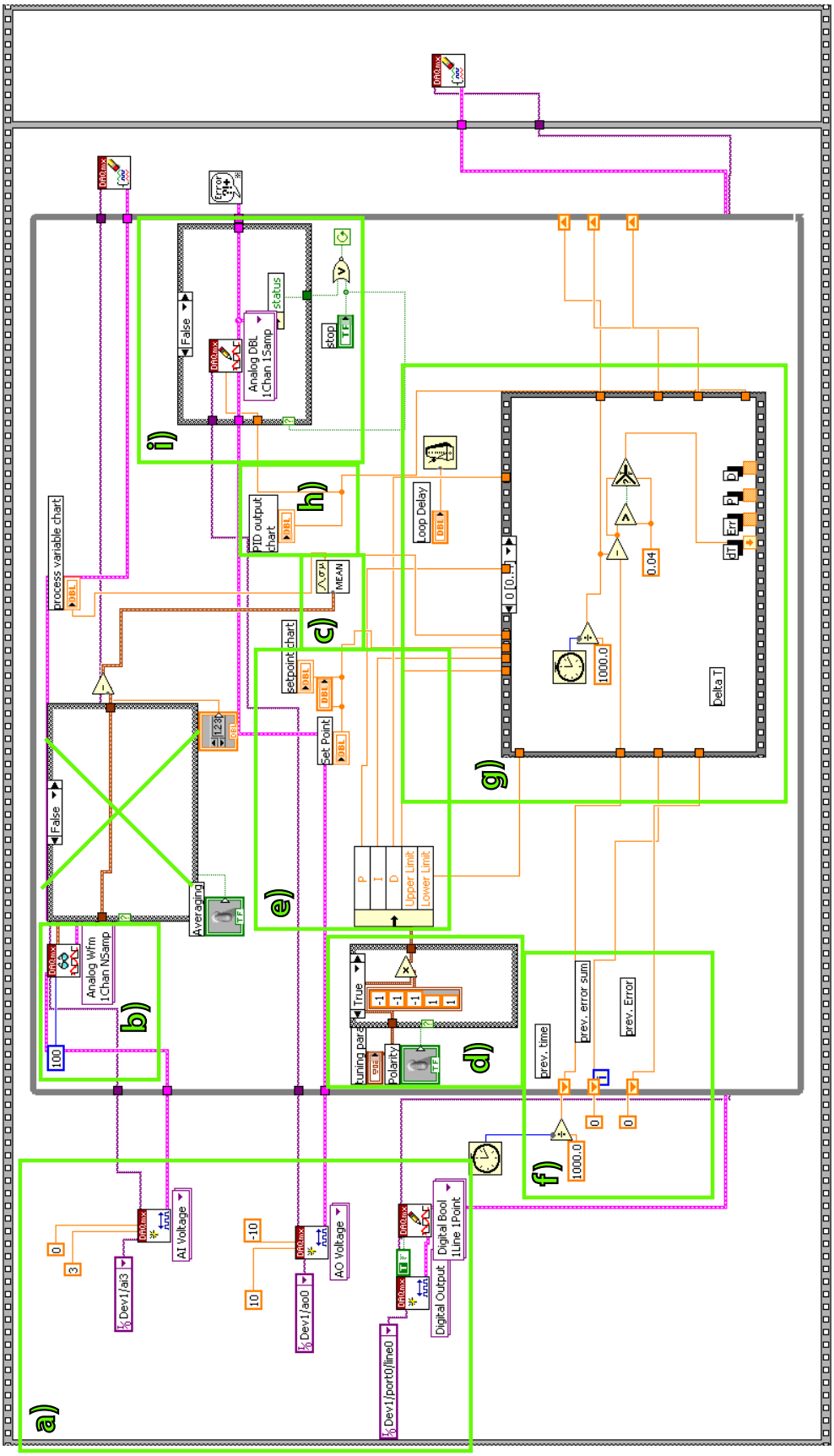

Figure B.15: *PID Control Loop_v4.vi* Locking of one entity Labview VI: Block Diagram

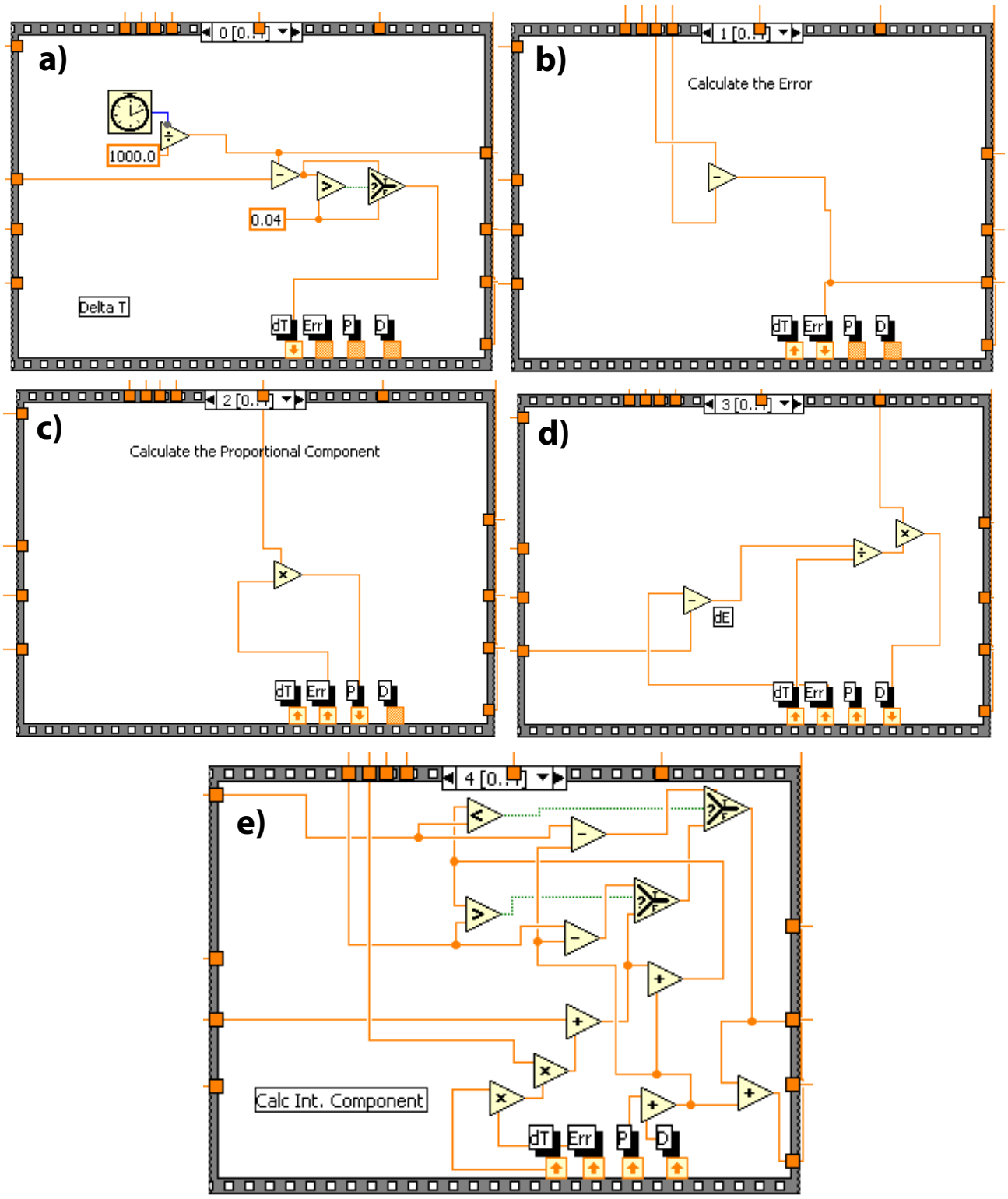

Figure B.16: *PID Control Loop_v4.vi* Locking of one entity Labview VI: Block Diagram, zoom of different case structures

B.2.4 Save Large File of Incoming Data

The file $ContAcq\&GraphVoltage-WriteDatatoSpreadsheetFile(CSV)\_v4.vi$ saves large streams of data in a manner much less resource intensive than the "Write to Measurement File" function that comes with Labview. The front panel, Figure B.17, has the standard inputs of filename, channel specifications, and sampling specifications, as discussed above in sections B.2.1 and B.2.2.

The block diagram is shown in Figure B.18. Section "a" sets the filename, section "b" initializes the input channel, and section "c" sets the total number of samples to be taken. Inside the while loop, section "d" dictates how many samples to acquire during an iteration of the while loop. The samples are then displayed in the graph on the front panel. Section "e" saves this data to a file using a low-level Labview function that writes data to a spreadsheet. The fact that this function is very basic means that it can operate very fast, causing little downtime in data taking while the computer writes the data to the disk. Finally, section "f" determines how many iterations of the while loop are necessary to acquire the requested amount of data. When the final iteration is complete, a signal is sent to terminate the while loop, the channels are cleared, and the program ends.

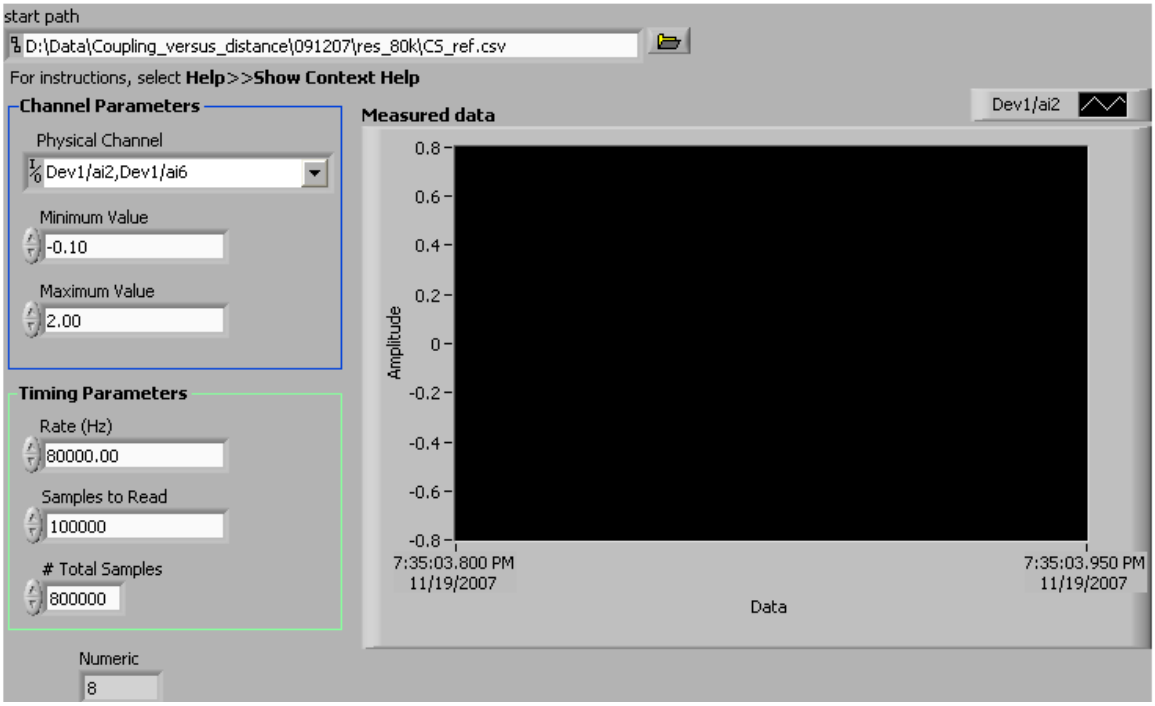

Figure B.17: $ContAcq\&GraphVoltage-WriteDatatoSpreadsheetFile(CSV)\_v4.vi$ Save Large File of Incoming Data Labview VI: Front Panel

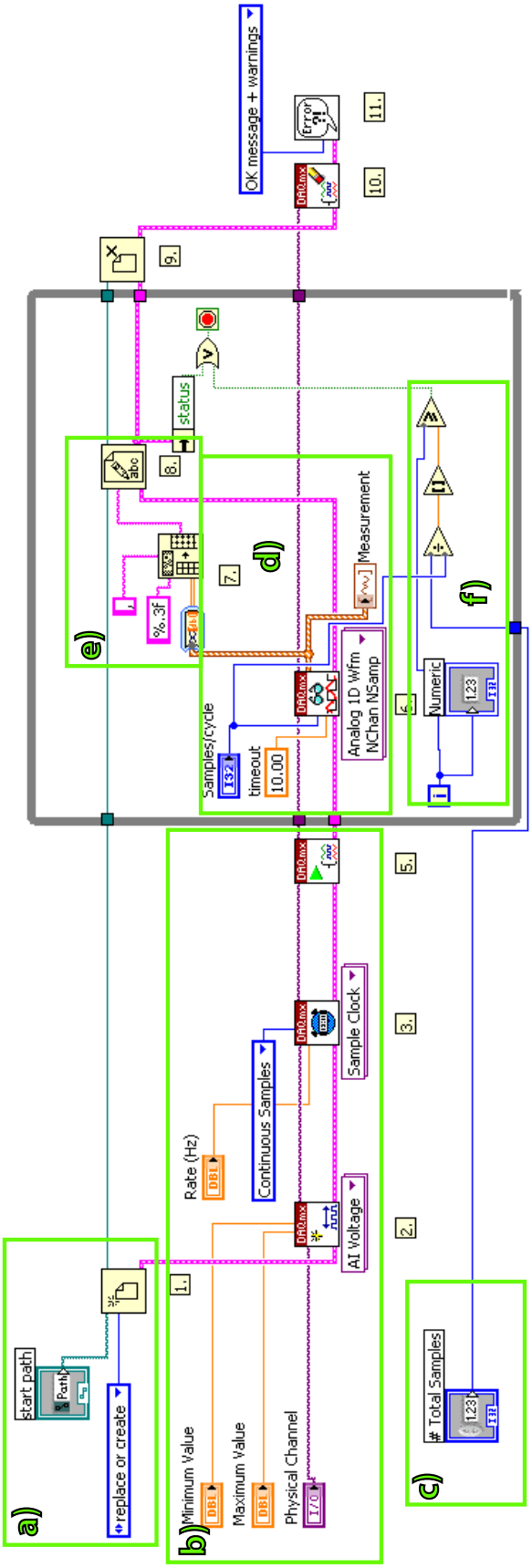

Figure B.18: $ContAcq\&GraphVoltage-WriteDatatoSpreadsheetFile(CSV)\_v4.vi$
Save Large File of Incoming Data Labview VI: Block Diagram

Bibliography

[1] J. Ye, D. W. Vernooy, and H. J. Kimble, Phys. Rev. Lett. **83**, 4987 (1999).

[2] J. McKeever, A. Boca, A. Boozer, and J. Buck, Nature **425**, 268 (2003).

[3] J. McKeever et al., Deterministic Generation of Single Photons from One Atom Trapped in a Cavity, 2004.

[4] K. Birnbaum et al., Nature **436**, 87 (2005).

[5] D. Vernooy, A. Furusawa, N. Georgiades, V. Ilchenko, and H. Kimble, Physical Review A **57**, 2293 (1998).

[6] D. Vernooy, V. Ilchenko, H. Mabuchi, E. Streed, and H. Kimble, Optics Letters **23**, 247 (1998).

[7] K. Vahala, Nature **424**, 839 (2003).

[8] J. Buck and H. Kimble, Physical Review A **67**, 33806 (2003).

[9] D. Armani, T. Kippenberg, S. Spillane, and K. Vahala, Nature **421**, 925 (2003).

[10] T. Kippenberg, S. Spillane, and K. Vahala, Applied Physics Letters **85**, 6113 (2004).

[11] V. B. Braginsky, M. L. Gorodetsky, and V. S. Ilchenko, Physics Letters A **137**, 393 (1989).

[12] S. Spillane et al., Physical Review A **71**, 13817 (2005).

[13] C. Hood, H. Kimble, and J. Ye, Physical Review A **64**, 33804 (2001).

[14] K. M. Birnbaum, *Cavity QED with Multilevel Atoms*, PhD thesis, California Institute of Technology, 2005.

[15] T. Aoki et al., Nature **443**, 671 (2006).

[16] J. Love et al., Optoelectronics [see also IEEE Proceedings-Optoelectronics], IEEE Proceedings J **138**, 343 (Oct 1991).

[17] R. Black, S. Lacroix, F. Gonthier, and J. Love, Optoelectronics [see also IEEE Proceedings-Optoelectronics], IEEE Proceedings J **138**, 355 (Oct 1991).

[18] T. J. Kippenberg, *Nonlinear Optics in Ultra-high-Q Whispering-Gallery Optical Microcavities*, PhD thesis, California Institute of Technology, 2004.

[19] T. Aoki et al., Nature **443** (2006).

[20] E. Jaynes and F. Cummings, Proceedings of the IEEE **51**, 89 (1963).

[21] G. Rempe, R. J. Thompson, and H. J. Kimble, Physica Scripta **T51**, 67 (1994).

[22] R. Miller et al., Journal of Physics B: Atomic, Molecular, and Optical Physics **38**, S551 (2005).

[23] P. Berman, *Cavity quantum electrodynamics*, Boston: Academic Press, 1994.

[24] H. Walther, **52** (2004).

[25] J. Raimond et al., J. Phys. B **38**.

[26] S. Nußmann et al., Nature Physics **1**, 122 (2005).

[27] G. Khitrova, H. Gibbs, M. Kira, S. Koch, and A. Scherer, Nature Physics **2**, 81 (2006).

[28] A. Badolato et al., Deterministic Coupling of Single Quantum Dots to Single Nanocavity Modes, 2005.

[29] A. Wallraff et al., Nature **431**, 162 (2004).

[30] I. Chiorescu et al., Nature **431**, 159 (2004).

[31] M. Keller, B. Lange, K. Hayasaka, W. Lange, and H. Walther, Nature **431**, 1075 (2004).

[32] T. Legero, T. Wilk, M. Hennrich, G. Rempe, and A. Kuhn, Physical Review Letters **93**, 70503 (2004).

[33] G. Rempe, R. Thompson, H. Kimble, and R. Lalezari, Opt. Lett **17**, 363 (1992).

[34] J. Cirac, P. Zoller, H. Kimble, and H. Mabuchi, Physical Review Letters **78**, 3221 (1997).

[35] H. J. Briegel, *The Physics of Quantum Information*, Springer, Berlin, 2000, edited by D. Bouwmeester, A. Ekert, and A. Zeilinger.

[36] L. Duan and H. Kimble, Physical Review Letters **92**, 127902 (2004).

[37] P. Treutlein et al., Fortschritte der Physik **54**, 702 (2006).

[38] S. Spillane, T. Kippenberg, O. Painter, and K. Vahala, Physical Review Letters **91**, 43902 (2003).

[39] J. Courtois, J. Courty, and J. Mertz, Physical Review A **53**, 1862 (1996).

[40] D. Vernooy and H. Kimble, Physical Review A **55**, 1239 (1997).

[41] M. Cai, O. Painter, and K. J. Vahala, Phys. Rev. Lett. **85**, 74 (2000).

[42] E. R. Abraham and E. A. Cornell, Appl. Opt. **37**, 1762 (1998).

[43] E. L. Raab, M. Prentiss, A. Cable, S. Chu, and D. E. Pritchard, Phys. Rev. Lett. **59**, 2631 (1987).

[44] P. D. Lett et al., Phys. Rev. Lett. **61**, 169 (1988).

[45] R. Gupta, S. Padua, C. Xie, H. Batelaan, and H. J. Metcalf, Journal of the Optical Society of America B Optical Physics **11**, 537 (1994).

[46] J. Reichel, W. Hänsel, and T. W. Hänsch, Phys. Rev. Lett. **83**, 3398 (1999).

[47] K. Lindquist, M. Stephens, and C. Wieman, Physical Review A **46**, 4082 (1992).

[48] M. Succi, R. Canino, and B. Ferrario, Vacuum **35**, 579 (1985).

[49] D. Lide, *CRC handbook of chemistry and physics*, CRC Press, 2004.

[50] R. Drever et al., Phys. B **31**, 97 (1983).

[51] E. Black, American Journal of Physics **69**, 79 (2001).

[52] Y. Chen, Y. Liao, L. Hsu, and I. Yu, Physical Review A **64**, 31401 (2001).

[53] Y. Çengel, *Heat Transfer: A Practical Approach*, McGraw-Hill, 2003.

[54] R. Younkin et al., Applied Physics Letters **71**, 1261 (1997).

[55] S. M. Spillane, *Fiber-coupled Ultra-high-Q Microresonators for Nonlinear and Quantum Optics*, PhD thesis, California Institute of Technology, 2004.

[56] G. Brambilla, V. Finazzi, and D. Richardson, Opt. Express **12**, 2258 (2004).

[57] J. M. Ward et al., Review of Scientific Instruments **77**, 083105 (2006).

[58] A. Cronin, C. McAtamney, R. Sherlock, G. M. O'Connor, and T. J. Glynn, Laser-based workstation for the manufacture of fused biconical tapered coupler devices, volume 5827, pages 505–514, SPIE, 2005.

[59] H. Konishi, H. Fujiwara, S. Takeuchi, and K. Sasaki, Applied Physics Letters **89**, 121107 (2006).

[60] M. Sumetsky, Y. Dulashko, and A. Hale, Opt. Express **12**, 3521 (2004).

[61] T. A. Birks and Y. W. Li, Journal of Lightwave Technology **10**, 432 (1992).

[62] O. Schmidt, K. Knaak, R. Wynands, and D. Meschede, Applied Physics B: Lasers and Optics **59**, 167 (1994).

[63] T. Kippenberg, S. Spillane, and K. Vahala, Optics Letters **27**, 1669 (2002).

[64] B. Dayan et al., Science **319**, Supporting Online Material for 1062 (2008).

[65] D. Rowland and J. Love, Optoelectronics [see also IEEE Proceedings-Optoelectronics], IEEE Proceedings J **140**, 177 (1993).

[66] B. Lipták, *Instrument Engineers' Handbook*, CRC Press, 2003.